Detection of Defects in FRP-Reinforced Concrete with the Acoustic-Laser Vibrometry Method

by

Justin Gejune Chen

B.S. Physics
California Institute of Technology, 2009

Submitted to the Department of Civil and Environmental Engineering
in partial fulfillment of the requirements for the degree of

Master of Science in Civil and Environmental Engineering

at the

MASSACHUSETTS INSTITUTE OF TECHNOLOGY

February 2013

Author .....
Department of Civil and Environmental Engineering
January 18, 2013

Certified by .....
Oral Büyüköztürk
Professor of Civil and Environmental Engineering
Thesis Supervisor

Certified by .....
Robert W. Haupt
Staff, MIT Lincoln Laboratory
Thesis Co-Supervisor

Accepted by .....
Heidi M. Nepf
Chair, Departmental Committee for Graduate Students

Detection of Defects in FRP-Reinforced Concrete with the Acoustic-Laser Vibrometry Method

by

Justin Gejune Chen

Submitted to the Department of Civil and Environmental Engineering
on January 18, 2013, in partial fulfillment of the
requirements for the degree of
Master of Science in Civil and Environmental Engineering

Abstract

Fiber-reinforced polymer (FRP) strengthening and retrofitting of concrete structural elements has become increasingly popular for civil infrastructure systems. When defects occur in FRP-reinforced concrete elements at the FRP-concrete interface, such as voids or delamination, FRP obscures the defect such that visual detection may not be possible. Most currently available non-destructive testing (NDT) methods rely on physical contact; an NDT method that is capable of remotely assessing damage would be greatly advantageous. A novel approach called the acoustic-laser vibrometry method which is capable of remote assessment of damage in FRP-reinforced concrete, is investigated in this thesis. It exploits the fact that areas where the FRP has debonded from concrete will vibrate excessively compared to intact material. In order to investigate this method, a laboratory system consisting of a commercial laser vibrometer system and conventional loudspeaker was used to perform tests with fabricated FRP-reinforced concrete specimens. The measurement results in the form of resonant frequencies were compared to those determined from theoretical and finite element defect models. With a series of measurements the vibrational mode shapes of defects and extent of the damage were imaged. The feasibility of the method was determined through a series of parametric studies, including sound pressure level (SPL), defect size, laser signal level, and angle of incidence. A preliminary Receiver Operating Characteristic (ROC) curve was determined for the method, and future work involving the acoustic-laser vibrometry method is proposed.

Thesis Supervisor: Oral Büyüköztürk
Title: Professor of Civil and Environmental Engineering

Thesis Co-Supervisor: Robert W. Haupt
Title: Staff, MIT Lincoln Laboratory

Acknowledgments

I would like to thank Rob Haupt and the rest of my old MIT Lincoln Laboratory team, Leaf, Marius, and Rich, for getting me started in working with laser vibrometry and its applications and really teaching me how to do this work. I'm thankful for my advisor, Professor Buyukozturk for introducing me to civil engineering and guiding me through my research.

Special thanks goes out to Tim Emge for helping me make measurements for supplying the FRP-steel specimen. John Doherty was also helpful in getting acquainted with the acoustic-laser vibrometry method. Also, I thank my previous group mates, Chakrapan and Denvid for their help and camaraderie.

This research was supported by the National Science Foundation (NSF), CMMI Grant No. 0926671, and I am grateful to the program managers, Dr. Mahendra Singh and Dr. Kishor Mehta for their interest in and support of this work. I also thank the American Society for Nondestructive Testing (ASNT) for their support through the 2011 Fellowship Award, and the opportunity to present this work at the 2012 Fall Conference.

Finally, I'm eternally grateful to my parents Yihwa and Minder for their encouragement and support in whatever endeavors I choose to pursue.

Contents

1 Introduction and Background **21**

1.1 Infrastructure Assessment 23

1.2 NDT of FRP-reinforced concrete 24

2 Phenomenology and Theory **27**

2.1 Concept 27

2.2 Failure Modes of FRP-reinforced Concrete and Basic Phenomenology 28

2.3 Simplified Defect Model 30

2.4 Rectangular Acoustic Cavity 32

3 Finite Element Analysis **35**

3.1 Sensitivity Analysis 35

3.2 Plate Model Frequency Analysis 40

3.3 Analysis With Air Void 42

3.3.1 Air Void 42

3.3.2 Concrete Void 44

3.4 Analysis of Curved Plate 46

3.5 Analysis of Curved Plate With Air Void 49

3.6 Air Void Depth 50

3.7 Summary: Finite Element Analysis 52

4 Materials and Methodology **53**

4.1 Fabrication of Concrete Test Specimens 53

4.2 Summary of FRP-reinforced Concrete Specimens 57
4.3 Experimental Setup 63
4.4 Components of Laboratory Acoustic-Laser Vibrometry System and Key Specifications 66

5 Defect Measurements **69**
5.1 Preliminary Measurements 69
5.2 Frequency Sweep Defect Measurements 71
5.2.1 FRPP1 71
5.2.2 FRPP2 74
5.2.3 FRPC1 77
5.2.4 FRPC2 80
5.2.5 FRPCAD3 83
5.2.6 FRPC4 85
5.2.7 FRPP3 87
5.2.8 FRPP4 89
5.2.9 FRPP5 91
5.2.10 Summary: Frequency Sweep Defect Measurements 97
5.3 Image Construction 97
5.3.1 FRPP1 98
5.3.2 FRPP2 100
5.3.3 FRPC1 105
5.3.4 FRPC2 107
5.3.5 FRPC4 108
5.3.6 FRPP5 0.5” Defect 113
5.3.7 Summary: Image Construction 116

6 Parametric Studies **119**
6.1 Sound Pressure Level 119
6.2 Angle of Incidence 121
6.3 Laser Signal Level 123

6.4 Dwell Time 124
6.5 Frequency Sweep Duration Study 127
6.6 Summary: Parametric Studies 128

7 Receiver Operating Characteristic Curve Analysis 129
7.1 ROC Curves 129
7.2 Scaling of ROC Curve with Parametric Study Results 134
7.3 Summary: ROC Curve Analysis 137

8 Summary, Conclusions, and Future Work 139
8.1 Summary 139
8.2 Conclusions 140
8.2.1 Measurement Methodology 140
8.2.2 Area Rate of Coverage 141
8.2.3 Distance Limitations 145
8.2.4 Defect Discrimination 146
8.3 Future Work 147

A Appendix 151
A.1 Chapter 5: Defect Measurements 151
A.1.1 Frequency Sweep Defect Measurements 151
A.2 Chapter 6: Parametric Studies 155
A.2.1 Sound Pressure Level 155
A.2.2 Dwell Time 156
A.2.3 Frequency Sweep Duration Study 160
A.3 Chapter 7: Receiver Operating Characteristic Curve Analysis 162

References 165

List of Figures

1-1 I-35W Bridge After Collapse 22

1-2 Corroded rebar and concrete spall, MIT Campus, West Garage 23

1-3 Damage in FRP reinforced bridge box-girder wall, Jamestown Bridge, RI 25

2-1 Notional acoustic-laser vibrometry system for NDT 28

2-2 Failure Modes of an FRP Strengthened RC beam 29

2-3 Acoustic-Laser Vibrometry 29

2-4 Mathematical Model of FRP Plate 30

3-1 X-Eigenvector of mode 1,1 of a simply supported plate, f = 49.0608 Hz 36

3-2 X-Eigenvector of mode 2,2 of a simply supported plate, f = 196.2432 Hz 37

3-3 X-Eigenvector of mode 3,3 of a simply supported plate, f = 441.5471 Hz 37

3-4 Percent error vs. number of elements for mode 1,1 38

3-5 Percent error vs. number of elements for mode 2,2 38

3-6 Percent error vs. number of elements for mode 3,3 39

3-7 The plate finite element model, showing the eigenvector values for the first resonant mode 41

3-8 Fourier analysis plot of the plate for out of plane vibration velocity at the center of the plate 42

3-9 Diagram of the full defect as modeled 43

3-10 Fourier analysis plot of the plate and air void for out of plane vibration velocity at the center of the defect 44

3-11 Fourier analysis plot of the plate and concrete model for out of plane vibration velocity at the center of the defect 46
3-12 The curved plate finite element model, showing the eigenvector values for the first resonant mode 47
3-13 Fourier analysis plot of the curved plate model for out of plane vibration velocity at the center of the defect 48
3-14 The full curved defect as modeled 49
3-15 Fourier analysis plot of the curved 1.5" × 1.5" plate and 1" air void for out of plane vibration velocity at the center of the plate 50
3-16 The full defect as modeled for the air void thickness analysis 51

4-1 Specimen mold and foam inserts 54
4-2 Cast concrete specimen with foam inserts 54
4-3 Cast concrete specimen with foam inserts removed 55
4-4 Specimen after wet FRP-epoxy layup 55
4-5 Completed FRP-reinforced concrete specimen 56
4-6 FRPP0, FRP-bonded reinforced concrete panel 58
4-7 FRPP1, FRP-bonded reinforced concrete panel 58
4-8 FRPP2, FRP-bonded reinforced concrete panel 59
4-9 FRPP3, FRP-bonded concrete panel 59
4-10 FRPP4, FRP-bonded concrete panel 60
4-11 FRPP5, FRP-bonded concrete panel 60
4-12 FRPC1, FRP-confined concrete cylinder 61
4-13 FRPC2, FRP-confined concrete cylinder 61
4-14 FRPCAD3, FRP-confined concrete cylinder 62
4-15 FRPC4, FRP-confined concrete cylinder 62
4-16 Diagram of experimental setup 63
4-17 Retroreflective tape adhered to specimen 64
4-18 Light reflected from retroreflective tape on specimen, imaged onto paper surrounding the laser vibrometer lens 64

4-19 Examples of measurement locations on specimen FRPP2 65
4-20 Sample measurement of sound pressure level of frequency sweep . . . 65
4-21 Polytec Laser Vibrometer OFV-505 and Controller OFV-5000 66
4-22 M-Audio DSM1 Studio Monitor 67
4-23 WaveBook/516E Data Acquisition System 67
4-24 Earthworks M30 Microphone 68
4-25 Earthworks 1021 Microphone Pre-amp 68

5-1 Background measurement of FRPP0 70
5-2 Frequency sweep measurement of FRPP0 70
5-3 Frequency response of FRPP1 at center of defect 72
5-4 Frequency response of FRPP1 at center side of defect 72
5-5 Frequency response of FRPP1 at corner of defect 73
5-6 Frequency response of FRPP1 over intact FRP-concrete system . . . 73
5-7 Frequency response of FRPP2 at center of defect 75
5-8 Frequency response of FRPP2 at center side of defect 75
5-9 Frequency response of FRPP2 at corner of defect 76
5-10 Frequency response of FRPP2 over intact FRP-concrete system . . . 76
5-11 Frequency response of FRPC1 at center of defect 78
5-12 Frequency response of FRPC1 at center side of defect 78
5-13 Frequency response of FRPC1 at corner of defect 79
5-14 Frequency response of FRPC1 over intact FRP-concrete system . . . 79
5-15 Frequency response of FRPC2 at center of defect 81
5-16 Frequency response of FRPC2 at center side of defect 81
5-17 Frequency response of FRPC2 at corner of defect 82
5-18 Frequency response of FRPC2 over intact FRP-concrete system . . . 82
5-19 Frequency response of FRPCAD3 at center top of defect 84
5-20 Frequency response of FRPCAD3 at center of defect 84
5-21 Frequency response of FRPC4 at top of defect 85
5-22 Frequency response of FRPC4 at center of defect 86

5-23 Frequency response of FRPC4 at bottom of defect 86
5-24 Frequency response of FRPC4 over intact FRP-concrete system . . . 87
5-25 Frequency response of FRPP3 over defect 88
5-26 Frequency response of FRPP3 over intact FRP-concrete system . . . 88
5-27 Frequency response of FRPP4 at center of defect 89
5-28 Frequency response of FRPP4 over internally cracked region 90
5-29 Frequency response of FRPP4 over intact FRP-concrete system . . . 90
5-30 Frequency response of FRPP5 over intact FRP-concrete system . . . 92
5-31 Frequency response of FRPP5 at center of 1" wide crack defect . . . 93
5-32 Frequency response of FRPP5 at center of 0.75" wide crack defect . . 94
5-33 Frequency response of FRPP5 at center of 0.5" wide crack defect . . . 95
5-34 Frequency response of FRPP5 at center of 0.25" wide crack defect . . 96
5-35 Frequency response of FRPP5 at center of 0.125" wide crack defect . 96
5-36 Surface plot of vibration amplitude for specimen FRPP1 at 3200 Hz, 1,1 mode 98
5-37 Surface plot of vibration amplitude for specimen FRPP1 at 4050 Hz, 2,1 mode 99
5-38 Surface plot of vibration amplitude for specimen FRPP1 at 6050 Hz, 3,1 mode 100
5-39 Surface plot of vibration amplitude for specimen FRPP2 at 1380 Hz, 1,1 mode 101
5-40 Surface plot of vibration amplitude for specimen FRPP2 at 1490 Hz, 2,1 mode 101
5-41 Surface plot of vibration amplitude for specimen FRPP2 at 1580 Hz, 2,1 mode 102
5-42 Surface plot of vibration amplitude for specimen FRPP2 at 2050 Hz, 3,1 mode 102
5-43 Surface plot of vibration amplitude for specimen FRPP2 at 2750 Hz, 4,1 mode 103

5-44 Surface plot of vibration amplitude for specimen FRPP2 at 3260 Hz, 1,3 mode 103
5-45 Surface plot of vibration amplitude for specimen FRPP2 at 3580 Hz, 2,3 mode 104
5-46 Surface plot of vibration amplitude for specimen FRPP2 at 3940 Hz, 3,3 mode 104
5-47 Surface plot of vibration amplitude for specimen FRPC1 at 4400 Hz, 1,1 mode 105
5-48 Surface plot of vibration amplitude for specimen FRPC1 at 6040 Hz, 1,2 mode 106
5-49 Surface plot of vibration amplitude for specimen FRPC1 at 8860 Hz, 2,1 mode 106
5-50 Surface plot of vibration amplitude for specimen FRPC2 at 2740 Hz, 2,1 mode 107
5-51 Surface plot of vibration amplitude for specimen FRPC2 at 3150 Hz, 1,1 mode 108
5-52 Surface plot of vibration amplitude for specimen FRPC4 at 6300 Hz . 109
5-53 Surface plot of vibration amplitude for specimen FRPC4 at 8100 Hz . 109
5-54 Surface plot of vibration amplitude for specimen FRPC4 at 9090 Hz . 110
5-55 Surface plot of vibration amplitude for specimen FRPC4 at 10000 Hz 110
5-56 Surface plot of vibration amplitude for specimen FRPC4 at 11000 Hz 111
5-57 Surface plot of vibration amplitude for specimen FRPC4 at 12000 Hz 111
5-58 Surface plot of vibration amplitude for specimen FRPC4 at 13000 Hz 112
5-59 Surface plot of vibration amplitude for specimen FRPC4 at 14700 Hz 112
5-60 Surface plot of vibration amplitude for specimen FRPC4 at 16700 Hz 113
5-61 Plot of vibration amplitude for specimen FRPP5, 0.5” width defect at 9390 Hz 114
5-62 Plot of vibration amplitude for specimen FRPP5, 0.5” width defect at 10010 Hz 114

5-63 Plot of vibration amplitude for specimen FRPP5, 0.5" width defect at 11340 Hz 115
5-64 Plot of vibration amplitude for specimen FRPP5, 0.5" width defect at 16300 Hz 115
5-65 Plot of vibration amplitude for specimen FRPP5, 0.5" width defect at 20000 Hz 116

6-1 Vibration amplitude of specimen FRPP1 vs. sound pressure level and fitted curve 120
6-2 Vibration amplitude vs. angle of incidence for FRPP1 specimen . . . 121
6-3 Diagram of rippled FRPP1 surface measurement 122
6-4 Vibration amplitude vs. angle of incidence for FRPS3 specimen . . . 123
6-5 Noise floor vs. fraction of light allowed through back into the laser vibrometer 124
6-6 SNR and vibration amplitude as a function of dwell time for a sine wave excitation for FRPP1 125
6-7 SNR and vibration amplitude as a function of dwell time for a white noise excitation for FRPP1 126

7-1 Scatter plot data from FRPP1 grid measurement at 3200 Hz 130
7-2 ROC curve for FRPP1 at 3200 Hz 131
7-3 Plot of true and false positive rate vs. detection velocity level for FRPP1 at 3200 Hz 131
7-4 ROC curve for FRPP2 at 1380 Hz 133
7-5 ROC curve for FRPC1 at 4400 Hz 133
7-6 ROC curve for FRPC2 at 3150 Hz 134
7-7 Estimated effect of sound pressure level on FRPP1 ROC curve 135
7-8 Estimated effect of laser power or distance on FRPP1 ROC curve . . 135
7-9 Estimated effect of angle of incidence on FRPP1 ROC curve 136

8-1 Time required to measure 1 square meter vs. measurement spacing, 0.2s measurement time 143
8-2 Time required to measure 1 square meter vs. measurement spacing, with false positive time penalty 144
8-3 Sound pressure level vs. Distance for commercial loudpseaker 146

A-1 Frequency response of FRPP5 at center side long of 1" wide crack defect 151
A-2 Frequency response of FRPP5 at center side short of 1" wide crack defect 152
A-3 Frequency response of FRPP5 at corner of 1" wide crack defect . . . 152
A-4 Frequency response of FRPP5 at center side long of 0.75" wide crack defect 153
A-5 Frequency response of FRPP5 at center side short of 0.75" wide crack defect 153
A-6 Frequency response of FRPP5 at corner of 0.75" wide crack defect . . 154
A-7 Vibration amplitude of specimen FRPP2 vs. sound pressure level and fitted curve 155
A-8 Vibration amplitude of specimen FRPC1 vs. sound pressure level and fitted curve 155
A-9 Vibration amplitude of specimen FRPC2 vs. sound pressure level and fitted curve 156
A-10 SNR and vibration amplitude as a function of dwell time for a sine wave excitation for FRPP2 156
A-11 SNR and vibration amplitude as a function of dwell time for a white noise excitation for FRPP2 157
A-12 SNR and vibration amplitude as a function of dwell time for a sine wave excitation for FRPC1 157
A-13 SNR and vibration amplitude as a function of dwell time for a white noise excitation for FRPC1 158
A-14 SNR and vibration amplitude as a function of dwell time for a sine wave excitation for FRPC2 158

A-15 SNR and vibration amplitude as a function of dwell time for a white noise excitation for FRPC2 159
A-16 Frequency Responses from FRPP1, 0.1 second long 0-20 kHz frequency sweep 160
A-17 Frequency Responses from FRPP1, 1 second long 0-20 kHz frequency sweep 160
A-18 Frequency Responses from FRPP1, 10 second long 0-20 kHz frequency sweep 161
A-19 Frequency Responses from FRPP1, 60 second long 0-20 kHz frequency sweep 161
A-20 Scatter plot data from FRPP2 grid measurement at 1380 Hz 162
A-21 Plot of true and false positive rate vs. detection velocity level for FRPP2 at 1380 Hz 162
A-22 Scatter plot data from FRPC1 grid measurement at 4400 Hz 163
A-23 Plot of true and false positive rate vs. detection velocity level for FRPC1 at 4400 Hz 163
A-24 Scatter plot data from FRPC2 grid measurement at 3150 Hz 164
A-25 Plot of true and false positive rate vs. detection velocity level for FRPC2 at 3150 Hz 164

List of Tables

2.1 Table of values of frequency parameter λ for a clamped square plate . 31

2.2 Material Properties and Estimated Resonant Frequencies for a 1.5" × 1.5" defect 32

2.3 Material Properties and Estimated Resonant Frequencies for a 3.0" × 3.0" defect 32

2.4 Resonant frequencies for a 0.0381m × 0.0381m × 0.0254m closed box 33

3.1 Material properties for sensitivity analysis 36

3.2 Finite element analysis derived resonant frequencies for a 1.5" × 1.5" plate 41

3.3 Material properties for air 42

3.4 Finite element analysis calculated resonant frequencies for a 1.5" × 1.5" plate over a 1.5" × 1.5" × 1" air void 43

3.5 Materials properties values for concrete 45

3.6 Resonant frequencies for the 1.5" × 1.5" curved plate and the percent difference from the flat plate 47

3.7 Resonant frequencies for the 3" × 3" curved plate and the percent difference from the flat plate 48

3.8 Calculated resonant frequencies for the curved 1.5" × 1.5" plate and 1" air void model 49

3.9 Resonant frequencies of plate and air void model of varying air void depth 51

4.1 FRP system material properties 53

4.2 Summary of Test Specimens 57
4.3 Polytec Laser Vibrometer system specifications 66
4.4 M-Audio DSM1 Studio Monitor specifications 67
4.5 WaveBook/516E Data Acquisition System specifications 68
4.6 Earthworks M30 Microphone specifications 68
4.7 Earthworks 1021 Microphone Pre-amp specifications 68

5.1 Visually determined resonant frequencies for specimen FRPP1 74
5.2 Visually determined resonant frequencies for specimen FRPP2 77
5.3 Visually determined resonant frequencies for specimen FRPC1 80
5.4 Visually determined resonant frequencies for specimen FRPC2 83
5.5 Visually determined resonant frequencies for specimen FRPCAD3 . . 85
5.6 Visually determined resonant frequencies for specimen FRPC4 87
5.7 Visually determined resonant frequencies for specimen FRPP4 91

6.1 Results from frequency sweep duration study 127

Chapter 1

Introduction and Background

A large part of the United States infrastructure consists of buildings, bridges, roadways, tunnels, dams, and pipelines among many other structures. These structures need to be inspected and maintained to ensure their optimal function and to prevent failures that would impair the operation of the US economy [1]. It is already the case that much of the nation's infrastructure is in need of desperate repair. More than 26% of the nation's bridges are either structurally deficient of functionally obsolete, the condition of many of the nation's estimated 100,000 miles of levees is unknown, and poor roadway conditions cost motorists $67 billion a year in repairs and operating costs [2]. These deficiencies in either inspection or maintenance have resulted in several high profile failures of critical structures.

The most recent well known example of a massive structural failure is the collapse of the I-35W highway bridge over the Mississippi River in Minneapolis, Minnesota as shown in Figure 1-1. Undersized gusset plates in the connections of the bridge from incorrect design, combined with a poor distribution of a much greater than average load led, to the sudden collapse [3, 4]. In addition to deficient design there is also the problem of damage which can only be detected through detailed inspection or may not be detectable.

Corrosion in reinforced-concrete structures is one such example. There have been documented cases of parking garages and bridges failing due to corrosion, causing significant property damage [5, 6]. Corrosion can also cause less

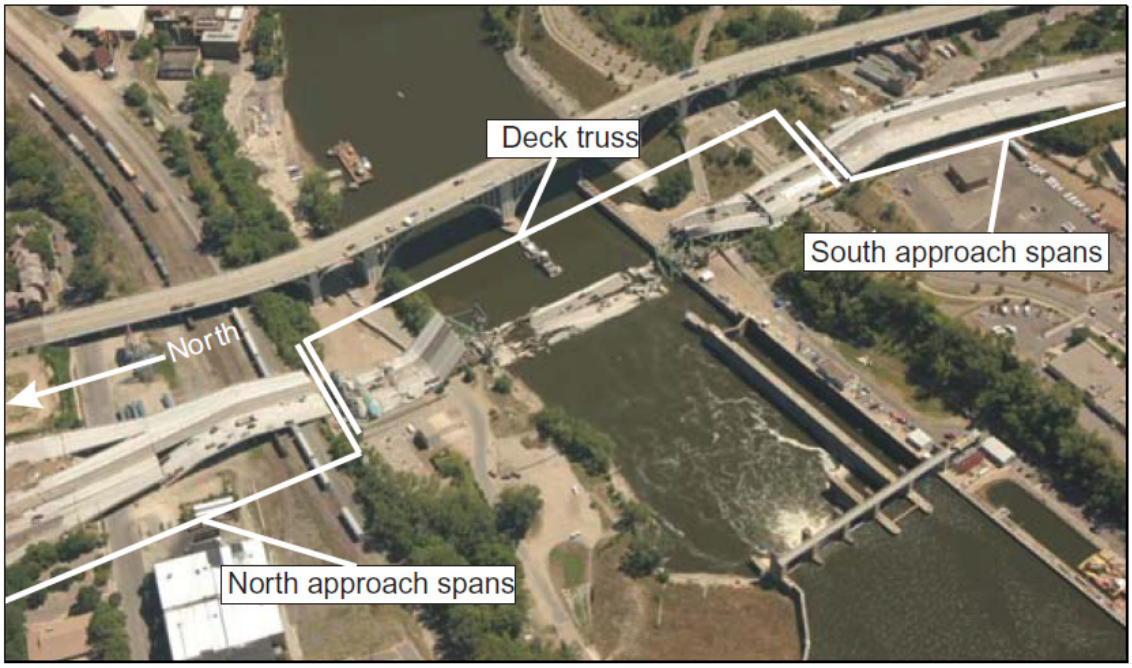

Figure 1-1: I-35W Bridge After Collapse [3]

catastrophic structural damage such as spall of the concrete cover, as seen in Figure 1-2, which also shortens the lifespan of the structure considerably, and in the case of structures such as overpasses and buildings which may have people and cars underneath, can be a dangerous failure mode. There are many documented cases of structural failures in the literature [7, 8, 9].

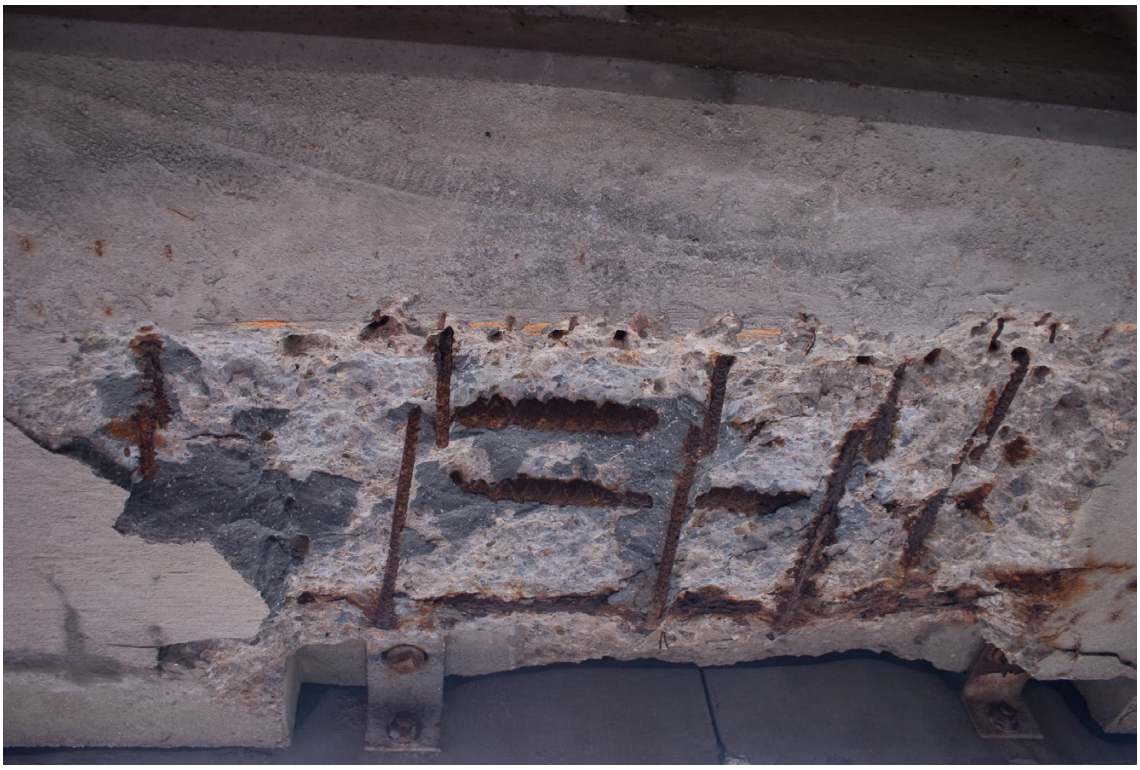

Figure 1-2: Corroded rebar and concrete spall, MIT Campus, West Garage

1.1 Infrastructure Assessment

There is a desperate need to detect damage in the structures that comprise the nation's infrastructure to prevent costly failures from happening. Accurate detection of damage can determine whether or not a structure is in proper operational condition and locate defects to direct maintenance and rehabilitation efforts. There are two general categories of methods for assessing the condition of structures: structural health monitoring (SHM) and non-destructive testing (NDT). SHM is the detection of damage from observation of general characteristics, such as resonant frequencies, damping coefficients, and mode shapes, of the structure over time [10, 11]. By observing these general characteristics over time, the global health condition of the system, in theory, can be determined and continuously monitored. NDT, in general terms, is the examination of an "object, material, or system without impairing its future usefulness" [12, 13]. The goal is to characterize an object in some way and detect damage or defects in an area local to the testing. A

rudimentary example of an NDT technique would be knocking on an object to see whether or not it is hollow [14]. They usually rely on fundamental physical characteristics of the object to detect damage. Technological innovations have expanded the scope of NDT and common techniques include acoustic, ultrasonic, magnetic, radiographic, thermographic, among others. Further technological development of NDT methods allows for better and faster detection of defects in materials and structures critical to the nation's infrastructure.

1.2 NDT of FRP-reinforced concrete

The nondestructive evaluation of concrete is important to the maintenance and monitoring of highways, bridges, and many other civil infrastructure systems. However, it is difficult to evaluate certain types of concrete structures, in particular, fiber-reinforced polymer (FRP) reinforced or retrofitted concrete structures. FRP has been used since the 1990s to strengthen and retrofit concrete structures in civil infrastructure applications [15, 16, 17]. The issue with damage detection in an FRP-reinforced concrete system, is that the FRP cover conceals any voids, cracks, or delamination that may have formed in the concrete under the reinforcement. Examples of such damage are shown in Figure 1-3. Detection of defects is especially important in the case where FRP has been retrofitted to previously damaged structures and further damage is a distinct possibility.

There currently does not exist a robust standoff method for measuring such damage. Currently commercially available and recently researched NDT technologies for FRP-reinforced concrete include elastic wave, ultrasound, x-ray, and radar methods [19, 18, 20, 21]. These methods all share the disadvantage of requiring either contact or close proximity of equipment with the specimen under test.

Standoff methods of damage detection have numerous advantages over contact measurement methods since they allow for measurement of damage in locations that are physically difficult to access, such as high above the ground or over water. Also

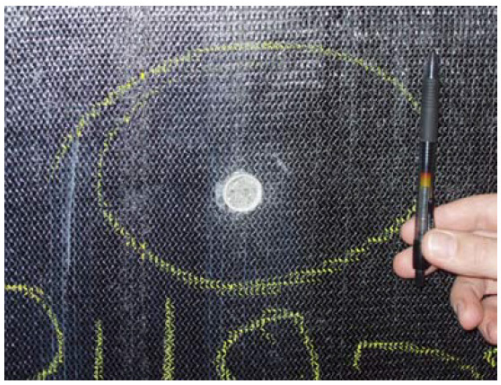

(a) Found air void defect with the removal of GFRP sheet

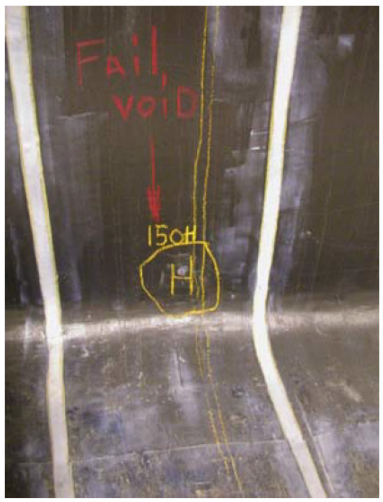

(b) Air void found near the corner

(c) Two found air voids

(d) Repaired air void defect

Figure 1-3: Damage in FRP reinforced bridge box-girder wall, Jamestown Bridge, RI [18]

measurements covering a large area are simpler since the equipment can be swept along a surface or reaimed to measure a different location. Laser vibrometry is one method of standoff measurement that measures the velocity of a surface.

Laser vibrometry has the ability to measure the surface velocity of objects from relatively large distances. To first order, measurements of velocity are only limited by laser power and line of sight [22]. With the advent of commercial laser vibrometers, researchers without a background in optical systems have the opportunity to make use of them. Some applications of laser vibrometry in NDT include brake rotors and

engine manifolds among other things in the automotive industry [23], ripeness of fruit [24], land mine detection [25, 26, 27], bubbles in paint coatings [28], and damage in composite materials [29, 30].

There is a relevant body of previous work using the acoustic-laser vibrometry method that has been applied to the detection of landmines [25, 31], and the detection of damage in FRP-steel bonded systems [32, 33]. Immediately related work on the detection of damage in FRP-reinforced concrete with the method has been published by collaborators [34].

Chapter 2

Phenomenology and Theory

2.1 Concept

There is a general need for NDT methods that can be conducted from a distance because standoff capability confers numerous advantages as mentioned previously. At the most basic level, NDT uses some sort of excitation to elicit a response from the object being measured and uses differences in the response to discriminate between intact and damaged areas. Keeping this in mind, to form a standoff NDT technique methods for standoff excitation and measurement of the target are required. A laser vibrometer and an acoustic excitation can be combined to form a standoff system that is capable of locating and measuring defects in materials. When excited by the acoustic source, defective areas will vibrate with an amplitude greater than intact areas. The vibration amplitude of the surfance of the specimen is measured and depending on the response frequency and areas where the response is exaggerated, defects are located. It is a powerful technique that allows for non-contact measurement and can be made into a relatively compact and portable system. Conceptually, the system is meant to measure tall or difficult to reach structures such as bridge piers and highway overpass structures. Figure 2-1 is a conceptual diagram of how the system might work for measuring the condition of a bridge pier from shore. In this work the specific application of detecting defects in FRP-reinforced concrete is investigated.

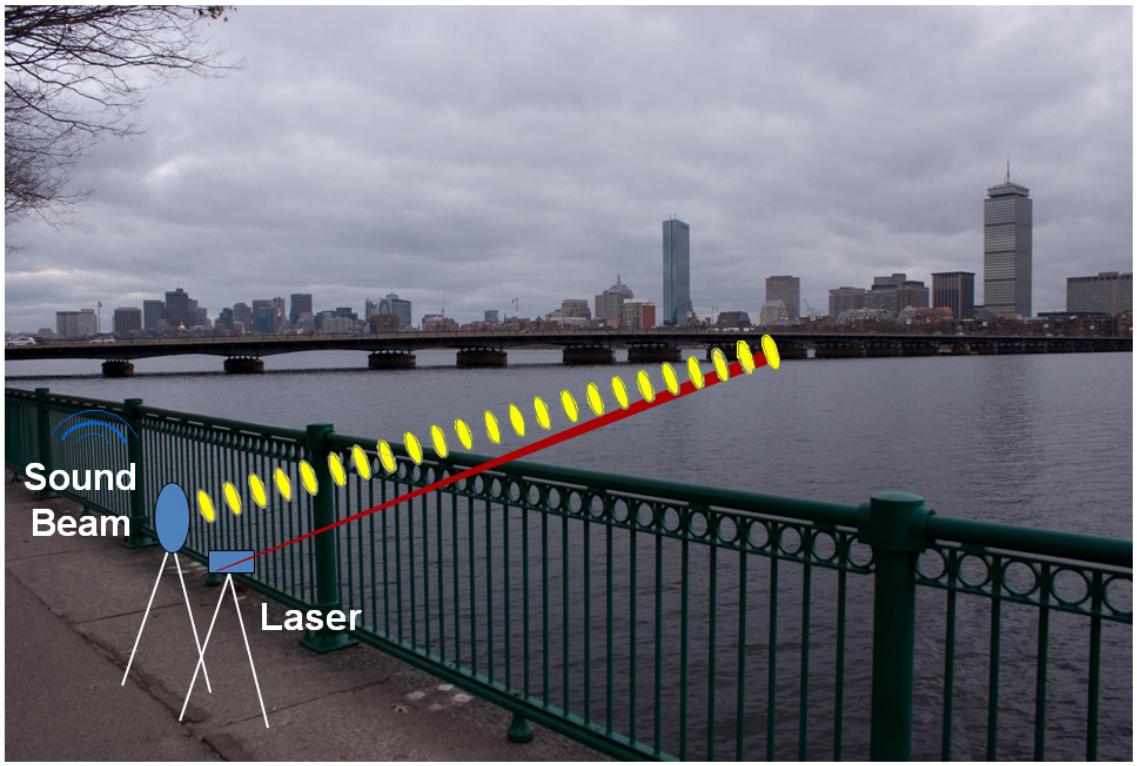

Figure 2-1: Notional acoustic-laser vibrometry system for NDT

2.2 Failure Modes of FRP-reinforced Concrete and Basic Phenomenology

In FRP-reinforced concrete there are a number of failure modes and defects that can occur as shown in Figure 2-2. The two types of damage the system is designed to detect are FRP debonding and void defects at the FRP-concrete interface. These are the two types of defects that result in the greatest difference in the surface vibration amplitude when the specimen is excited by an airborne acoustic wave at the surface. The measurement methodology exploits a variation in surface compliance due to these anomalies.

The debonding or delamination of FRP allows it to freely vibrate on the surface while in the case of intact material, epoxy firmly bonds the FRP to the concrete. When an FRP-reinforced concrete structure is stimulated by acoustic pressure waves from a loudspeaker or similar source, the area over a defect, will vibrate like a drum

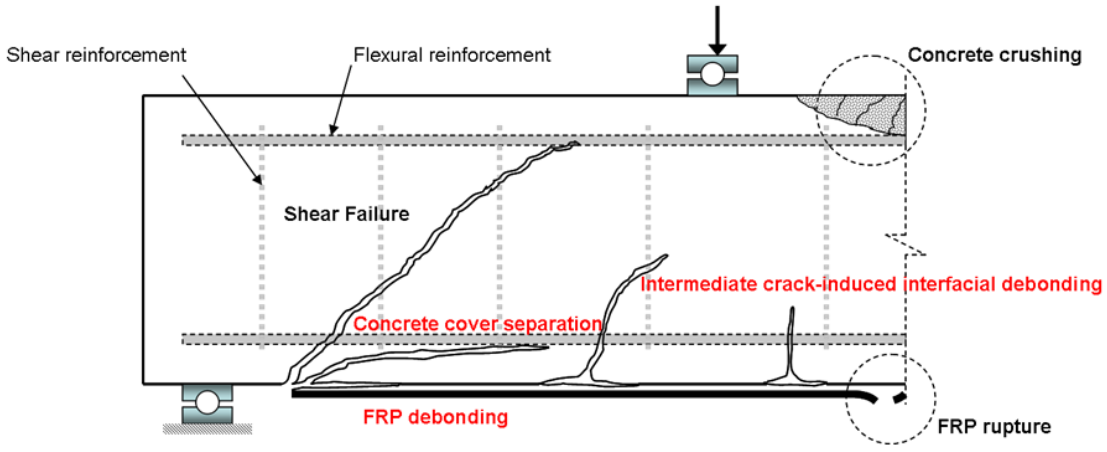

Figure 2-2: Failure Modes of an FRP Strengthened RC beam [35, 36]

head as shown in Figure 2-3. Since the FRP is much thinner than the underlying concrete, elastic waves induced in the structure by the acoustic excitation will have a much greater vibration amplitude in the areas where the FRP is detached due to a defect, when compared to areas where the FRP-concrete system is intact. By using frequency sweeps for the acoustic excitation the specimen is excited over a wide band of frequencies. The laser vibrometer measures the surface vibration of the target, obtaining the vibration frequency response to locate and characterize any anomalies. Different defects will have different frequency responses and we can use this to approximately determine the size and shape of a detected defect.

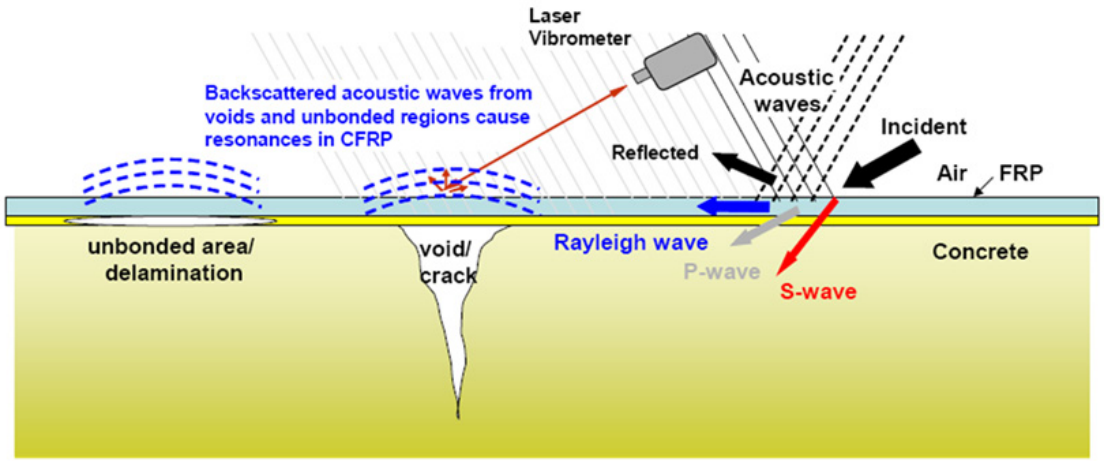

Figure 2-3: Acoustic-Laser Vibrometry [34]

2.3 Simplified Defect Model

To model a defect where the FRP has delaminated from the concrete in a certain area, a simplified mathematical model is considered: a square clamped plate, shown in Figure 2-4. Even though FRP is a directional material, for simplicity it is assumed to be isotropic. The air beneath the plate, which is much less dense and less "stiff" than the FRP is also assumed to have a negligible effect on the resonant frequencies of the plate. The boundary where the FRP is bonded to the concrete is assumed to be a clamped boundary condition. The classical plate equation that describes this defect is in Equation 2.1 [37].

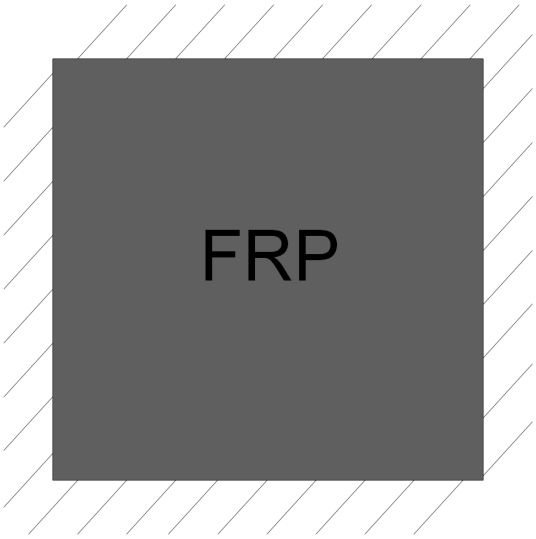

Figure 2-4: Mathematical Model of FRP Plate

$$D\nabla^4 w + \rho h \frac{\partial^2 w}{\partial t^2} = 0 \tag{2.1}$$

$D = \frac{Eh^3}{12(1-\nu^2)}$ = flexural rigidity of the plate

E = Young's modulus

h = thickness of the plate

ν = Poisson's ratio

ρ = density of the material

$w = w(x, y, t)$ transverse displacement of the plate as a function of spatial variables

x,y, and time t

The resonant frequencies of the plate are determined by Equation 2.2.

$$f = \frac{\lambda}{2\pi a^2}\sqrt{\frac{D}{\rho h}} \tag{2.2}$$

λ = a frequency parameter

a = side length of the square plate

f = resonant frequency

The value of frequency parameter λ is given in Table 2.1 for different vibrational modes, for the boundary condition and geometric shape, a square plate that is clamped on all sides [38].

Mode	1	2	3	4	5	6
1	35.999989	73.405	131.902	210.526	309.038	428
2		108.237	165.023	242.66	340.59	458.27
3			220.06	296.35	393.36	509.9
4				371.38	467.29	583.83
5					562.18	676
6						792.5

Table 2.1: Table of values of frequency parameter λ for a clamped square plate [38]

Using these equations, the expected resonant frequency of the different vibrational modes of the plate, assuming an isotropic material, can be calculated. Since fiberglass is not an isotropic material, so this method is only reasonable for giving an estimate of the fundamental resonant frequency. Using the following material property values, a table of resonant frequencies was calculated, shown in Tables 2.2 and 2.3. If the properties of the FRP being measured are known, from a measured resonant frequency, an estimation of the detect size can be back calculated.

Material Properties of FRP			Calculated Resonant Frequencies	
Defect side length	0.0381 m		Mode	Frequency (Hz)
Young's modulus	20.9 GPa		1,1	5151
Poisson's ratio	0.2		2,1	10504
Density	1800 $\frac{kg}{m^3}$		2,2	15488
Thickness	1.3 mm		3,1	18875

Table 2.2: Material Properties and Estimated Resonant Frequencies for a 1.5" × 1.5" defect

Material Properties of FRP			Calculated Resonant Frequencies	
Defect side length	0.0762 m		Mode	Frequency (Hz)
Young's modulus	20.9 GPa		1,1	1288
Poisson's ratio	0.2		2,1	2626
Density	1800 $\frac{kg}{m^3}$		2,2	3872
Thickness	1.3 mm		3,1	4719

Table 2.3: Material Properties and Estimated Resonant Frequencies for a 3.0" × 3.0" defect

2.4 Rectangular Acoustic Cavity

Now consider a cubic defect where there is a void in the concrete that is obscured by the FRP. The mathematical model for this defect is a rectangular box that is filled with air and this void will have specific resonant frequencies determined by the lengths of the sides of the box and the mode number, separate from those associated with the FRP plate covering the box. The resonance comes from the air vibrating inside the box. Resonant frequencies for the box are determined by Equation 2.3 [39]

$$f = \frac{\nu}{2}\sqrt{(\frac{l}{L_x})^2 + (\frac{m}{L_y})^2 + (\frac{n}{L_z})^2} \tag{2.3}$$

ν = speed of sound in air

L_x, L_y, L_z = length, width, and depth of the box

l, m, and n = some non-negative integer corresponding to mode number

Assuming the speed of sound is 344.9392 m/s, the first couple of resonant frequencies for a box of size 0.0381m × 0.0381m × 0.0254m are calculated in Table 2.4.

l	m	n	Frequency (Hz)
1	0	0	4526.76
1	1	0	6401.81
0	0	1	6790.14
1	0	1	8160.73
2	0	0	9053.52
1	1	1	9332.16

Table 2.4: Resonant frequencies for a 0.0381m $\times$ 0.0381m $\times$ 0.0254m closed box

Air is much less dense by approximately a factor of 10^3, and less stiff by a factor of approximately 10^6 than FRP. Since the FRP plate is much more massive than the volume of air in the void, the air is not able to "move" the plate and so there should not be a large effect of the vibration of the air on the vibration of the plate. There may be some effect if the resonant frequencies of the plate and the void are very close, leading to some interaction between the two resonances, but in this example with these specific material and physical defect properties this is not the case.

In the case of more complex defects such as a model incorporating both the FRP plate, air void, and associated interaction, a curved plate, or any irregular defect shape, finite element analysis (FEA) is necessary to determine the resonant frequencies of the defect. These are examples of relevant situations in which simple closed form numerical or analytical solutions for the resonant frequencies are not possible or easily available.

Chapter 3

Finite Element Analysis

The best way to accurately obtain resonant frequencies for a given defect is to model the defect and loads in a finite element analysis (FEA) program. It is also the simplest way to calculate the resonant frequencies with many different defect configurations and loads because only the input geometry and settings need to be changed in the finite element analysis program. As long as an accurate mathematical model to approximate the real life defect is used in the finite element analysis, a reasonable estimation of the resonant frequencies can be obtained.

3.1 Sensitivity Analysis

Initially, a sensitivity analysis was performed to determine the effect of the mesh size on the resonant frequencies that result from the finite element analysis. The model used was a flat 3" × 3", 1mm thick plate that is simply supported on all edges, which has an easily accessible closed form solution from classical plate theory. Three modes to compare the FEA generated results with the actual values were used. The material properties used here, given in Table 3.1 are different from the actual FRP properties used in the later FEA, however the sensitivity analysis still applies. Mode 1,1 has an analytically derived frequency of 49.0608 Hz, mode 2,2 with a frequency of 196.2432 Hz, and mode 3,3 a frequency of 441.5471 Hz. The three modes are shown in Figures 3-1, 3-2, and 3-3 respectively.

Side length	0.0762 m
Young's modulus	148 GPa
Poisson's ratio	0.0
Density of FRP	1.5e6 $\frac{kg}{m^3}$
Thickness of FRP plate	1mm

Table 3.1: Material properties for sensitivity analysis

In order to analyze the finite element method wed like to compare the number of elements used, and types of elements used. We will use shell elements for our finite element model since we already know that given this sort of thickness to length ratio of approximately 1/100, shell elements are far superior to 3D-solid elements [40]. Our finite element model is a square plate in the Y-Z plane. To have a simply supported boundary we have no translation but allow Y or Z rotation at the boundary. Since only the vibrational modes normal to the surface are relevant, degrees of freedom were restricted to X-translation, Y-rotation and Z-rotation.

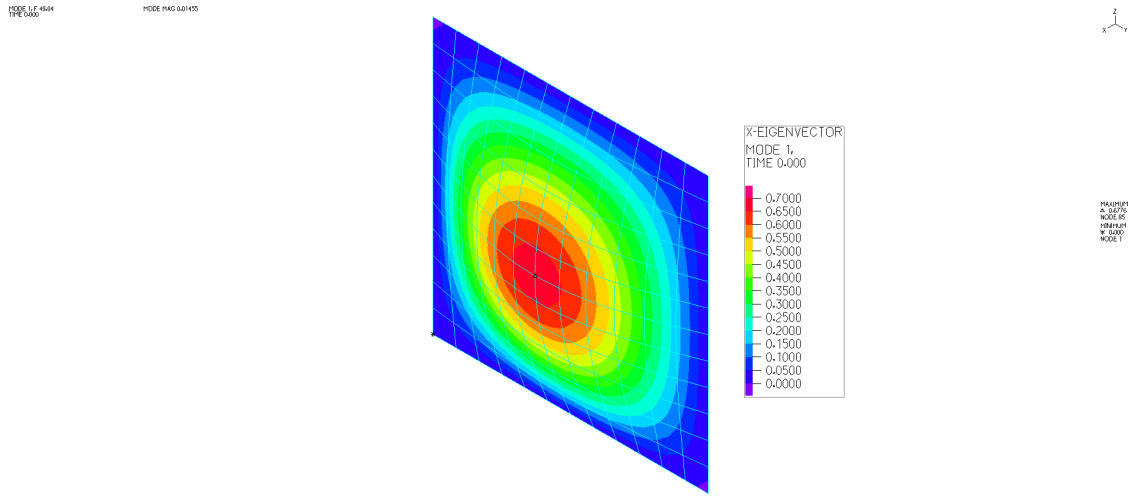

Figure 3-1: X-Eigenvector of mode 1,1 of a simply supported plate, f = 49.0608 Hz

These modes were obtained from models with varying numbers of 4 and 9 node elements. Plots of the percent error vs. number of elements used for the model were obtained for the 1,1, 2,2, and 3,3, vibrational modes.

Figure 3-4 shows the error comparison for mode 1,1. 9 node elements allowed the value for f11 as calculated from the finite element model (FEM) to converge very

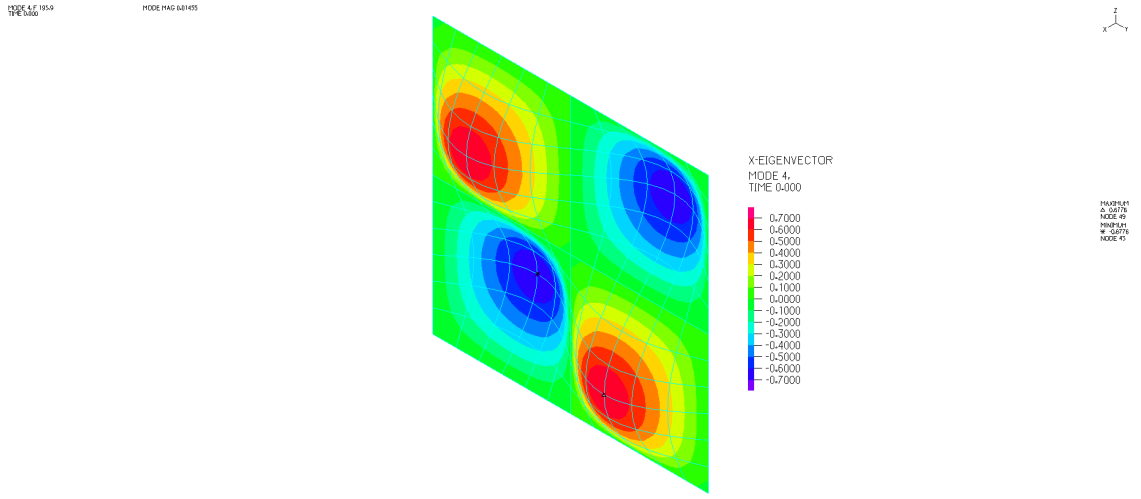

Figure 3-2: X-Eigenvector of mode 2,2 of a simply supported plate, f = 196.2432 Hz

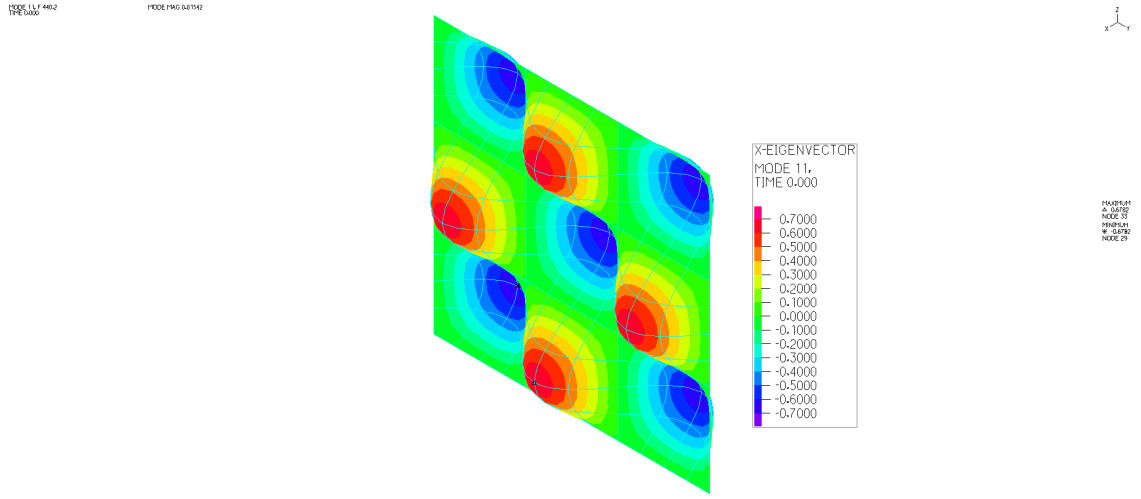

Figure 3-3: X-Eigenvector of mode 3,3 of a simply supported plate, f = 441.5471 Hz

quickly. With only 2 elements across, or 4 elements total the first mode frequency was determined to within 1% of the actual value. With 4 elements across there was better than 0.1% error. When the error increases after the minimum at 5 elements it showed that the computation converged to some, slightly lower frequency than the analytical solution. Usage of 4 node elements allowed for a somewhat accurate solution with a relatively small number of elements, reaching 1% error with 10 elements on one side.

Figure 3-5 shows the error comparison for mode 2,2. Again the use of 9 node

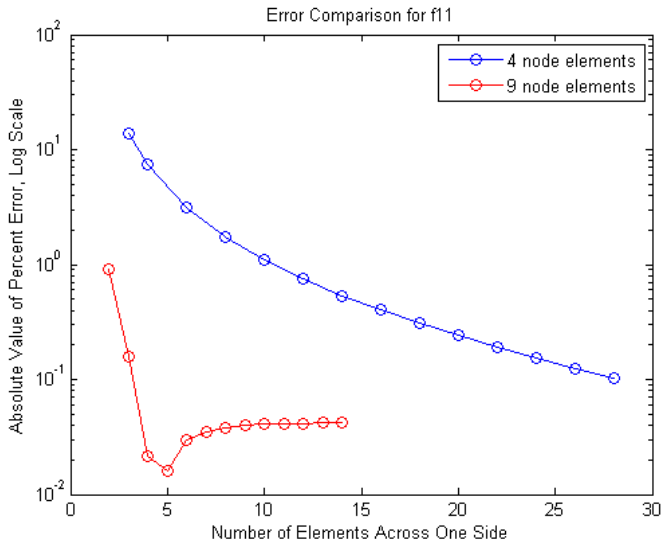

Figure 3-4: Percent error vs. number of elements for mode 1,1

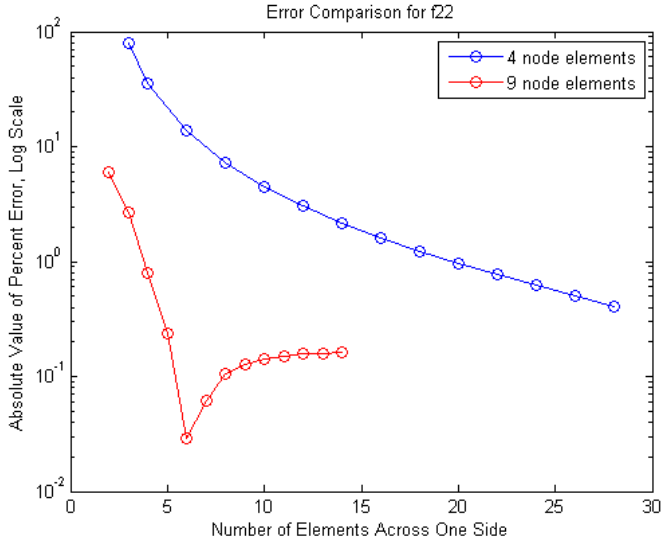

Figure 3-5: Percent error vs. number of elements for mode 2,2

elements allowed for very quick convergence of the solution and a minimum error of 0.03% was obtained at 6 elements across one side. 1% error was obtained with 4 elements across and less than 0.1% error with 6 elements across. For 4 node elements the frequency reached 1% error at 20 elements. The solution did not converge nearly as quickly as when 9 node elements were used.

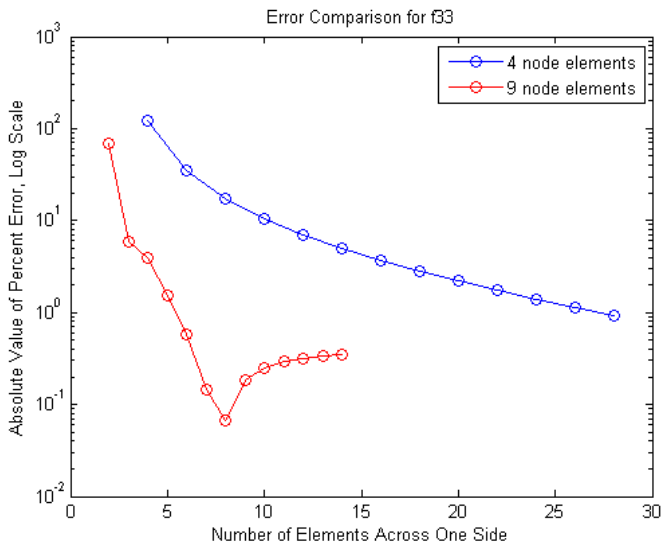

Figure 3-6: Percent error vs. number of elements for mode 3,3

Figure 3-6 shows the error comparison for mode 3,3. For 9 node elements, there was less than 1% error at 6 elements across one side and a minimum of 0.05% error at 8 elements across. Yet again, 9 node elements were very efficient at producing an accurate solution. For 4 node elements, 1% error was obtained at about 28 nodes. Again the convergence of the solution happened at about the same rate as previously and was outmatched by 9 node elements.

Summarizing the conclusions from the preceding plots, to obtain 1% error for the resonant modes of our simply supported plate, with 4 node elements the model needed about 20 elements in length per wavelength, while the 9 node elements only required about 4. This gives a rule of thumb to check if the mesh is fine enough for a certain vibrational mode. For 9 node elements a 0.1% error was obtained with about 6 elements across per wavelength. For a simulated analysis, as many 9 node elements as allowed by computational power will be used. These two guidelines determine an estimated maximum frequency that can be calculated accurately.

3.2 Plate Model Frequency Analysis

A finite element analysis on an FRP plate was conducted to confirm the model geometry and check agreement with plate theory. A commercial FEA software was used to conduct this analysis [40]. If there is good agreement, then it supports the argument that our method is reasonable. The model used for the FRP plate, was a square plate that is clamped on all sides. This approximated the delaminated FRP portion of the defect. The model consisted of a 7×7 grid of 9 node shell elements, which is a mesh size that is a compromise between computation speed and accuracy. Since the model has side length 0.0381 m, each shell element is 4.23 mm $\times$ 4.23 mm. For materials properties the values in Table 2.2 were used. The resulting frequencies of the plate from FEA were compared to those calculated in Chapter, also shown in Table 2.2.

To calculate the response, the model was run through 10^4 time steps of 10^{-5} seconds each, for a total time of 0.1 second. This resulted in a Nyquist frequency of 50 kHz. To approximate the frequency sweep, a pressure load of 0.2 Pa was applied on the surface of the plate model, with a frequency sweep from 0-20 kHz over the 0.1 second of the analysis. The 0.2 Pa of pressure corresponds to a sound pressure level (SPL) of 80 dB re 20 Pa which was a sound level that is close to that used in the experimental measurements. This excitation was used to determine the frequency response of the model under a uniform pressure load, similar to the specimen being excited by an acoustic wave with a frequency sweep waveform. Figure 3-7 shows a band plot of the displacement eigenvectors for the first resonant mode, which occurs at 5099 Hz.

The resonant frequencies as determined by finite element analysis and the difference from theory are shown in Table 3.2. The resonant frequencies from the plate model are in close agreement with theory. The model could be made more accurate at the expense of computational power, however it was already limited by the number of time steps necessary for the dynamically loaded analysis to approximate the experimental conditions.

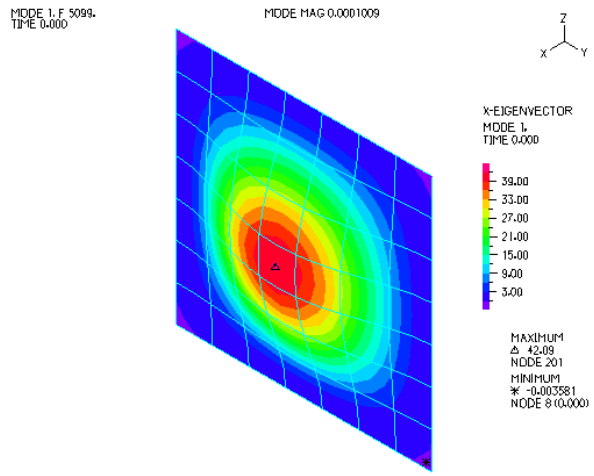

Figure 3-7: The plate finite element model, showing the eigenvector values for the first resonant mode

Mode	**Frequency (Hz)**	**Difference from theory**
1 - 1,1	5098.71	-1.015%
2 - 2,1	10337.0	-1.59%
3 - 1,2	10337.0	-1.59%
4 - 2,2	15128.3	-2.322%
5 - 3,1	18461.9	-2.189%
6 - 1,3	18560.8	-1.665%

Table 3.2: Finite element analysis derived resonant frequencies for a 1.5" $\times$ 1.5" plate

Figure 3-8 is a plot of the Fourier analysis of the response at the center of the plate model due to the frequency sweep loading. This shows the base resonant frequency at 5099 Hz of the plate. Note that the plate also responds at approximately 17 kHz which does not correspond to any of the resonant frequencies.

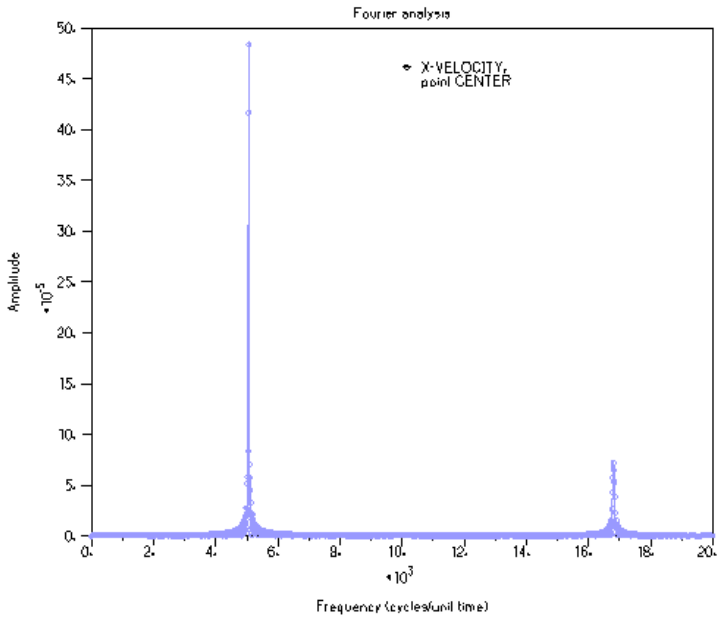

Figure 3-8: Fourier analysis plot of the plate for out of plane vibration velocity at the center of the plate

3.3 Analysis With Air Void

3.3.1 Air Void

Next, the defect was modeled as a system consisting of an air void and an FRP plate as shown in Figure 3-9. This more closely resembles the defect as it is in the experimantal FRP-reinforced concrete specimens. The basis for the model comes from an example problem presented previously in the literature [41]. The FRP plate is clamped on all sides, while the air void is clamped on 5 sides representing the boundaries of intact concrete, and on the remaining side it is constrained to move with the FRP plate. The same material properties as in the plate analysis for the FRP were used, and values used to define the properties of the air are given in Table 3.3.

Bulk modulus of air	1.404e5 Pa
Density of air	1.18 $\frac{kg}{m^3}$
Air void dimensions	0.0381m $\times$ 0.0381m $\times$ 0.0254m

Table 3.3: Material properties for air

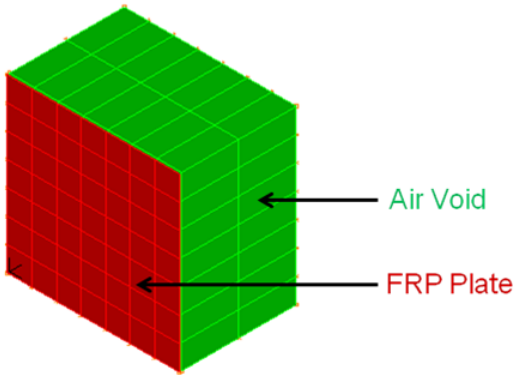

Figure 3-9: Diagram of the full defect as modeled: FRP plate in red, air void in green

Mode	Frequency (Hz)	Vibrational mode
1	365.342	Free body motion of air
2	4520.31	1,0,0 mode of air void
3	4533.67	0,1,0 mode of air void
4	5024.34	1,1 mode of plate
5	6394.15	1,1,0 mode of air void
6	6885.26	0,0,1 mode of air void
7	8088.79	1,0,1 mode of air void
8	8115.71	0,1,1 mode of air void
9	9038.8	2,0,0 more of air void
10	9073.69	0,2,0 mode of air void
11	9303.84	1,1,1 mode of air void

Table 3.4: Finite element analysis calculated resonant frequencies for a 1.5" × 1.5" plate over a 1.5" × 1.5" × 1" air void

The plate part of the model consists of a 7 × 7 grid of 9 node shell elements as before. The air void part is a 7 × 7 × 2 grid of 27 node 3D solid elements. Again, they were constrained on one side to move together, to enforce the boundary condition at the FRP plate. The same loading on the model as the previous analysis to excite the model over a broad range of frequencies was used. Table 3.4 shows the resonant modes of the model and identifies them with respect to which part of the model they come from.

Figure 3-10 shows the response of the model at the center of the FRP plate to the frequency sweep. The air void resonances in the perpendicular directions did not

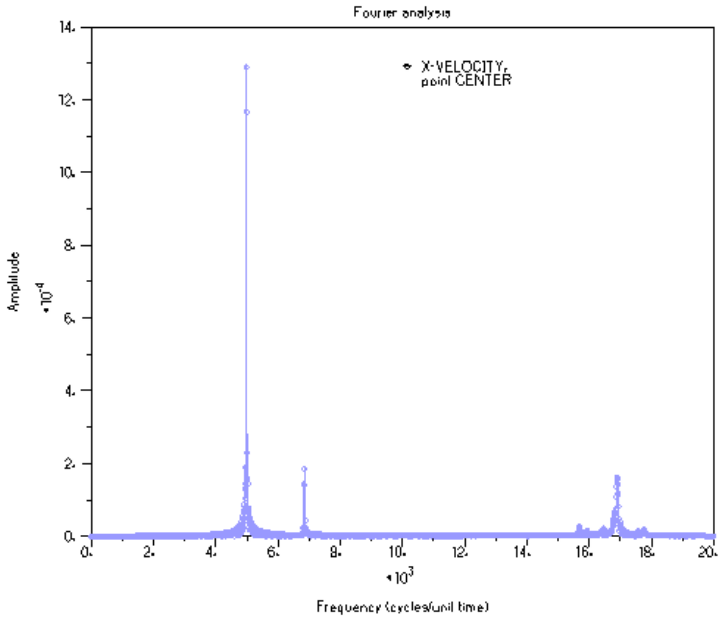

Figure 3-10: Fourier analysis plot of the plate and air void for out of plane vibration velocity at the center of the defect

contribute to the response of the model as measured on the surface of the FRP plate, however the 0,0,1 mode of the air void did contribute to the response in this model. This makes sense as that vibrational mode is in the direction of the measurement. In this case, the first resonant frequency of the plate that manifests itself in the response at 5024.32 Hz, was lower than that obtained from the model of only a plate at 5098.71 Hz. The air void effectively increased the mass of the plate, lowering the resonant frequency.

3.3.2 Concrete Void

To confirm the expected result when the FRP is properly bonded to the concrete, there is no response, concrete was substituted for the cavity of air. The material properties used for concrete are in Table 3.5 and the same material properties for the FRP were used.

The velocity response for the plate at the center over a similar "void" composed of concrete is shown in Figure 3-11. The time step was reduced to 5×10^{-6} seconds for

Young's modulus of concrete	30 GPa
Poisson's ratio of concrete	0.2
Density of concrete	2400 $\frac{kg}{m^3}$

Table 3.5: Materials properties values for concrete

a Nyquist frequency of 100 kHz because the concrete is stiffer and therefore vibrates at a higher frequency. Note that the frequency axis now goes from 0 to 100 kHz.

The Fourier analysis plot in Figure 3-11 compared with Figure 3-10 for the plate over the air void, only above approximately 40 kHz was there a resonant frequency for the FRP plate over concrete. This resonant frequency was erroneous and was due to the mathematical model having a fixed boundary at the sides of the 1.5" $\times$ 1.5" $\times$ 1" box. The real world sample would not have that boundary because it would be a much larger concrete panel or cylinder and therefore would not resonate at that frequency. In this situation the plate vibration did not show up in the response because the concrete block is so much more massive than the FRP plate. This confirms the theory and measurements that a region of FRP-reinforced concrete without any defects will not exhibit any resonant frequencies and will look "dead" to the laser vibrometer.

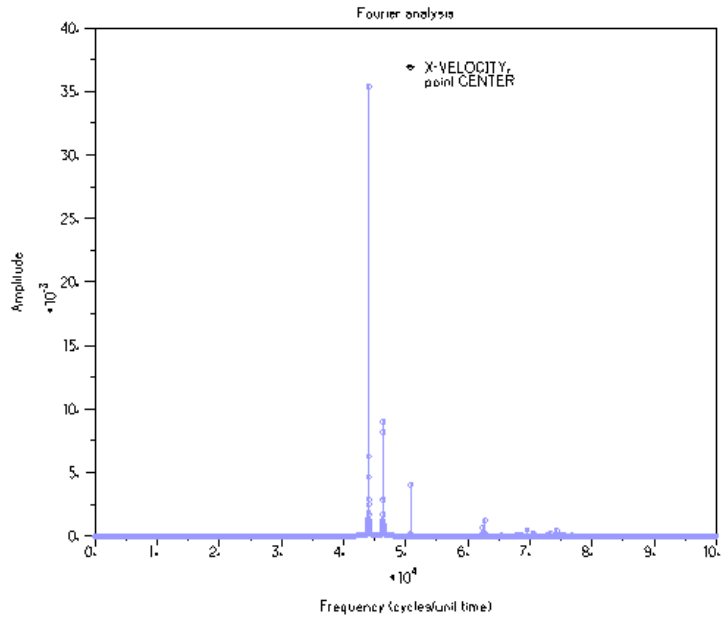

Figure 3-11: Fourier analysis plot of the plate and concrete model for out of plane vibration velocity at the center of the defect

3.4 Analysis of Curved Plate

The previous analysis covered defects on flat concrete panels, but a concrete column or cylinder provides a curved surface. The curved surface is expected to increase the stiffness of the FRP plate and therefore have a higher resonant frequency. Therefore, FEA was used to model a curved plate and a void covered by a curved plate to determine the effect on the frequency response.

The 1.5" × 1.5" FRP plate was modeled with a radius of curvature of 3" corresponding to the 6" diameter of our concrete samples. The plate is of the same size and has the same material properties as the flat plate modeled before. A band plot of the displacement eigenvectors for the first mode and picture of the model is shown in Figure 3-12.

The first resonant frequency was at 7940.6 Hz. This corresponded to a 56% increase in frequency over the flat plate caused by the increased stiffness of the curved plate. This was expected, because the curvature reduces the plate's ability to deform, and effectively increases the stiffness. A list of the first couple of resonant modes and

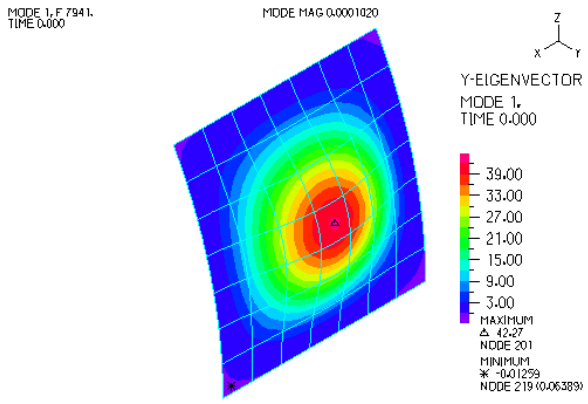

Figure 3-12: The curved plate finite element model, showing the eigenvector values for the first resonant mode

frequencies of the plate is shown in Table 3.6.

Mode	**Frequency (Hz)**	**Difference from flat plate**
1 - 1,1	7940.6	56%
2 - 2,1	10690.6	3.4%
3 - 1,2	12139.8	17.5%
4 - 2,2	15775.7	4.3%
5 - 3,1	18695.0	1.3%
6 - 1,3	19652.8	5.9%

Table 3.6: Resonant frequencies for the 1.5" $\times$ 1.5" curved plate and the percent difference from the flat plate

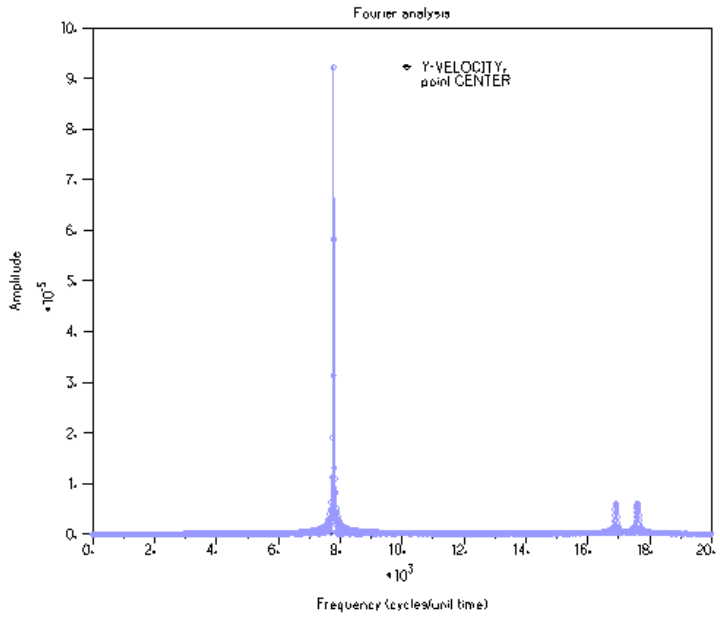

Figure 3-13: Fourier analysis plot of the curved plate model for out of plane vibration velocity at the center of the defect

The same Fourier analysis was done on the plate loaded with a frequency sweep pressure load normal to the curved surface to determine the frequency response and the plot is shown in Figure 3-13. The 2,1; 1,2; and 2,2 modes did not contribute to the response since the center of the plate is on a nodal line for those vibrational modes.

Resonant modes for a 3" × 3" specimen were also determined are are shown in Table 3.7.

Mode	**Frequency (Hz)**	**Difference from flat plate**
1 - 1,1	3751.7	191.3%
2 - 2,1	4305.6	64.0%
3 - 1,2	5730.6	118.2%
4 - 2,2	5906.2	52.5%
5 - 3,1	6783.3	43.7%
6 - 1,3	7343.8	55.6%

Table 3.7: Resonant frequencies for the 3" × 3" curved plate and the percent difference from the flat plate

3.5 Analysis of Curved Plate With Air Void

A defect with a curved FRP plate covering the air void as shown in Figure 3-14 was also considered.

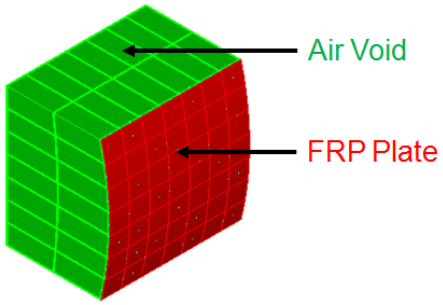

Figure 3-14: The full curved defect as modeled: FRP plate in red, air void in green

The model is the same as before with the 1.5" × 1.5" plate, except the top surface of the void is curved and the FRP is similarly curved. The resonant frequencies calculated by the finite element analysis program are given in Table 3.8. They were similar to that of the normal cubic defect, except for the increased frequency of the plate vibration.

Mode	**Frequency (Hz)**	**Vibrational mode**
1	533.9	Free body motion of air
2	4546.7	1,0,0 mode of air void
3	4674.9	0,1,0 mode of air void
4	6433.6	1,1,0 mode of air void
5	6509.6	0,0,1 mode of air void
6	7866.4	1,0,1 mode of air void
7	7936.8	1,1 mode of plate vibration

Table 3.8: Calculated resonant frequencies for the curved 1.5" × 1.5" plate and 1" air void model

To check that the first mode of plate vibration was indeed the main mode in the frequency response of the defect, a Fourier analysis of the response at the center of the plate was done as shown in Figure 3-15. The 7936.8 Hz first mode of plate vibration is the main response of the defect. This is only very slightly lower than in the case of the curved plate defect without the air void, showing that the air void has even less

effect on the vibration of the plate.

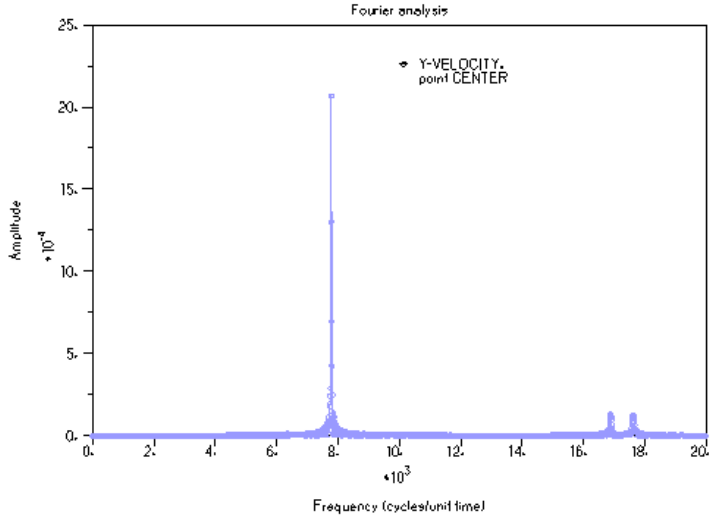

Figure 3-15: Fourier analysis plot of the curved 1.5" × 1.5" plate and 1" air void for out of plane vibration velocity at the center of the plate

3.6 Air Void Depth

An analysis of the void depth vs. resonant frequency was also conducted. As before, the defect was modeled as a system consisting of an air void and an FRP plate as shown in Figure 3-16. The FRP plate is clamped on all sides, while the air void is clamped on 5 sides representing the boundaries of intact concrete, and on the free side it is constrained to move with the FRP plate.

The plate part of the model consists of a 7 × 7 grid of 9 node shell elements as before. The air void part is a 7 × 7 × 3 grid of 27 node 3D fluid elements. They are tied together on one side to enforce the boundary condition at the FRP plate. For materials properties the same values as previously were used, as specified in Tables **??** and 3.3.

A simple frequency eigenvalue analysis was done for the models to obtain the resonant frequencies to be compared with that of just the clamped plate. The plate alone had a base resonant frequency of 5098.71 Hz. For the plate and air void model

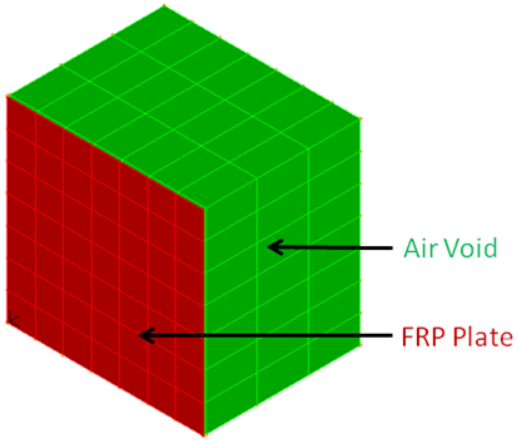

Figure 3-16: The full defect as modeled for the air void thickness analysis: FRP plate in red, air void in green

Air void thickness (m)	**4th Mode plate frequency (hz)**
0.005	5183.56
0.01	5147.92
0.015	5101.89
0.02	5069.96
0.025	5033.05
0.03	4958.02

Table 3.9: Resonant frequencies of plate and air void model of varying air void depth

the fourth resonant mode corresponded to the same mode shape and vibrational mode as the base resonant mode of the clamped plate. Table 3.9 shows the resonant frequencies at the fourth mode for the finite element models with voids of varying depths.

When the air void was thin, the resonant frequency was actually higher than that of the clamped plate. With an air void depth of approximately half the side length, the frequency was close to that of the clamped plate, and when the air void was thicker, the resonant frequency was lower than that of the clamped plate. A possible explanation is that when the air void is thin, it acts as a spring increasing the effective stiffness of the plate, while when the air void is thick, the air adds mass to the plate, does not have much of a spring effect, and the resonant frequency is lowered. This means that once a defect is imaged, the measured resonant frequency

can be compared to the theoretical resonant frequency for a clamped plate of the same size and shape to possibly determine the approximate depth of the air void defect. The caveat is that diferences in frequency will most likely be differences in the defect geometry between the modeled and actual defect.

3.7 Summary: Finite Element Analysis

Finite element models were studied to see if they could be used to provide insight into the defect phenomenology. From the sensitivity study, for approximately 1% error in the resonant frequency when compared to analytical calculations, the finite element model needs to have a mesh density that provides 4 elements per wavelength with 9 node elements. Adding curvature to the plate increased the base resonant frequency because of a stiffening effect, and can be predicted by finite element analysis. The effect of an air void on the resonant frequency of the defect was quantified and studied. With a thinner air void the resonant frequencies are increased slightly, and with a thicker air void, the resonant frequencies are decreased slightly. With full knowledge and good modeling of the defect geometry, the thickness of the air void underneath the defect may be able to be quantified. In practice this will be difficult because of the lack of information about the true defect geometry necessary to determine if the frequency has shifted up or down from the plate only configuration.

Chapter 4

Materials and Methodology

4.1 Fabrication of Concrete Test Specimens

In order to test the system a series of FRP-reinforced concrete panels or cylinders with created defects were produced to simulate defects that might be measured in the real world. The FRP used was Tyfo SEH-51 composite, bonded to the concrete panel by wet lay-up with Tyfo S epoxy, from Fyfe co. Some specifications are given in Table 4.1. The following pictures illustrate the process of creating the specimens.

Material Properties	**Dry Fiber**	**Epoxy**	**Composite Laminate**
Density ($\frac{kg}{m^3}$)	2550	1110	
Tensile Modulus (GPa)	72.4	3.18	26.1 (test), 20.9 (design)
Laminate Thickness (mm)			1.3

Table 4.1: FRP system material properties [42]

Shown here was the process for the creating the FRPP5 specimen. First, foam was glued into a mold for casting the concrete specimen as in Figure 4-1. In this specific case, defects of multiple sizes are put into this mold, so that a study can be done to determine the minimum detectable crack size. Then, the concrete was cast in the mold and left to cure for at least one week, ideally a month, resulting in a concrete block with pieces of foam embedded in it as in Figure 4-2. Then, the pieces of foam were removed so that hollow voids were left in the concrete block as in Figure 4-3. Then the fiberglass was bonded to the concrete with epoxy using the wet

lay-up process as in Figure 4-4. The epoxy required a day to cure, and the resulting specimen is shown in Figure 4-5.

Figure 4-1: Specimen mold and foam inserts

Figure 4-2: Cast concrete specimen with foam inserts

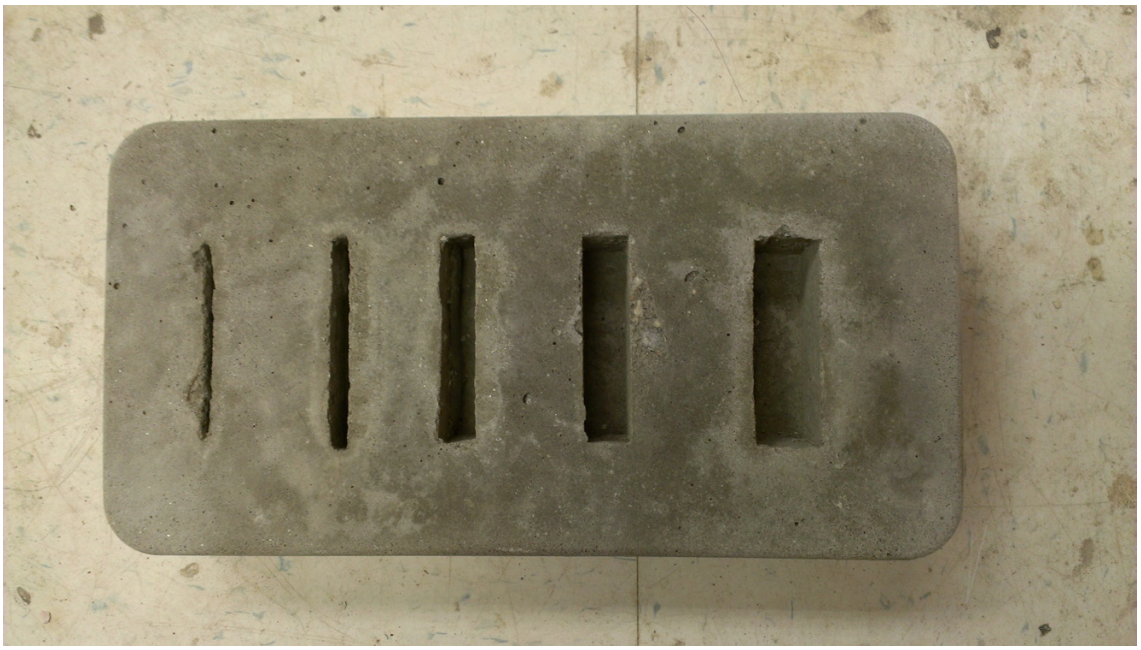

Figure 4-3: Cast concrete specimen with foam inserts removed

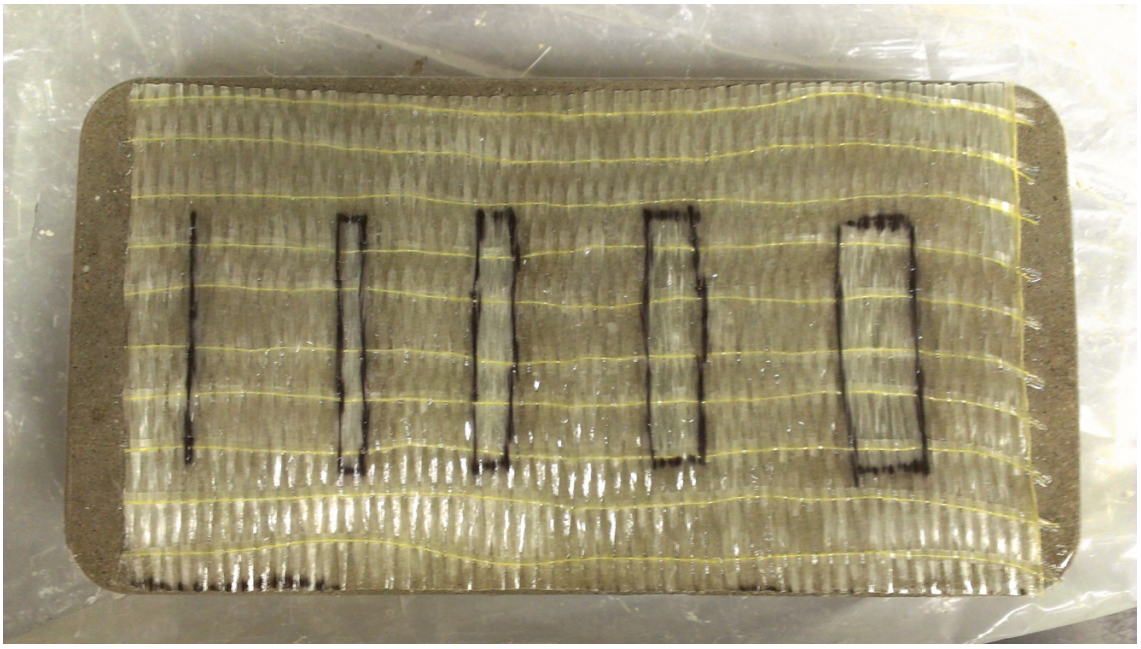

Figure 4-4: Specimen after wet FRP-epoxy layup

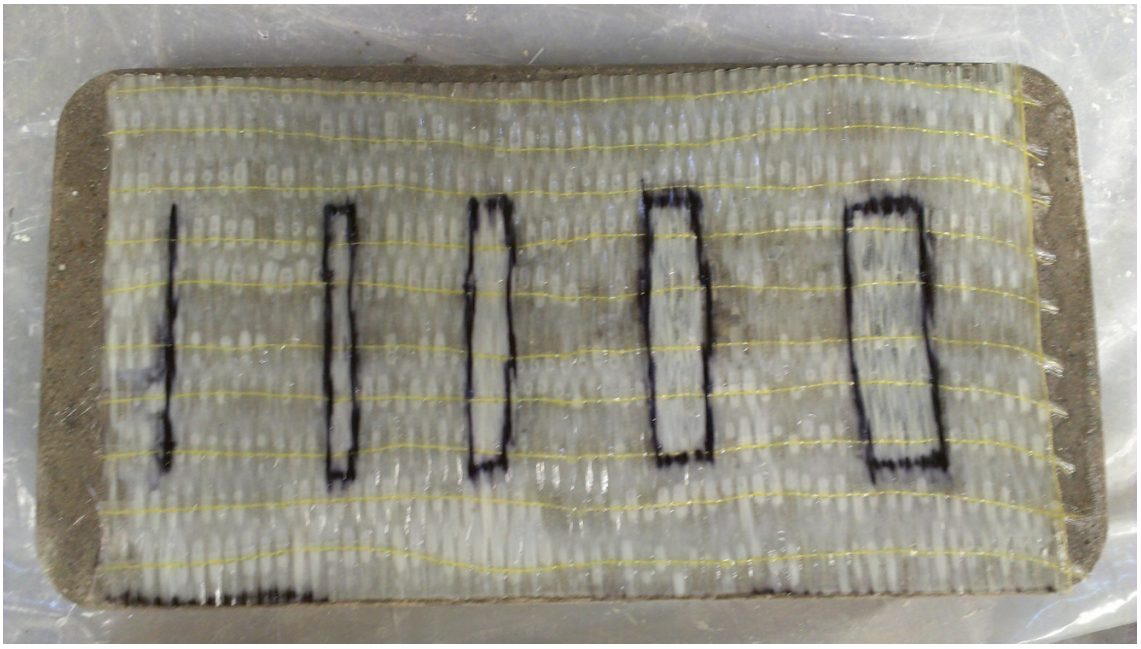

Figure 4-5: Completed FRP-reinforced concrete specimen

4.2 Summary of FRP-reinforced Concrete Specimens

There were two basic specimen types, either FRP-confined concrete cylinders, or FRP-bonded concrete panels. There were also two types of defects, a 1.5" × 1.5" × 1.0" cubic defect, and a 3" × 3" × 0.2" delamination-like defect, on both the cylinder and a panel specimen. This was used to study the effect of the curvature of the defect on the resonant frequencies observed by the system. Then, for the concrete cylinder specimens, there were specimens that have a 1" x 15" x 1" full length defect, and an irregular 1.5" × 5" delamination defect. For the concrete panels, there were specimens that have a 3" × 0.25" × 1.5" crack defect, a 3" × 0.25" × 1.5" 30° angled defect, and a panel that includes multiple sizes of crack defects, 3" × 0.125", 0.25", 0.5", 0.75", 1" × 1.5". The specimens are summarized in Table 4.2, and described along with figures of the specimens below.

FRP-Confined Concrete Cylinder	**FRP-Bonded Concrete Panel**	**Damage Type**
	FRPP0	No damage
FRPC1	FRPP1	Cubic defect
FRPC2	FRPP2	Delamination-like defect
FRPCAD3		Full length defect
FRPC4		Irregular delamination defect
	FRPP3	Crack defect
	FRPP4	Angled crack defect
	FRPP5	Multiple sizes of crack defects

Table 4.2: Summary of Test Specimens

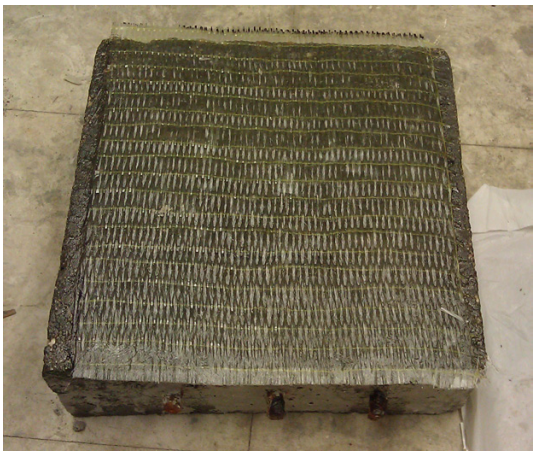

Figure 4-6: FRPP0, FRP-bonded reinforced concrete panel
Size: Height 12” × Width 12” × Depth 4”
No defects

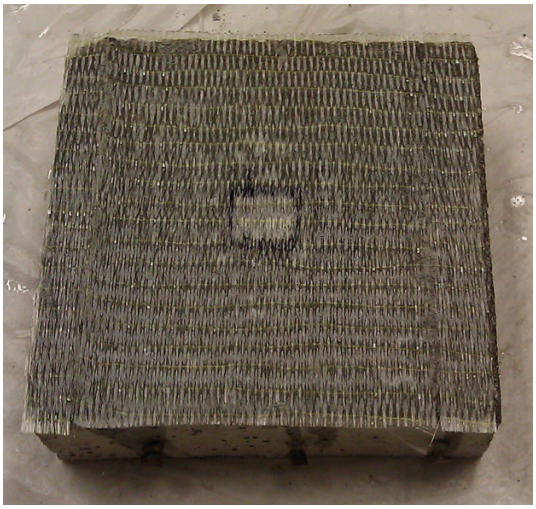

Figure 4-7: FRPP1, FRP-bonded reinforced concrete panel
Size: Height 12” × Width 12” × Depth 4”
Cubic defect size: Height 1.5” × Width 1.5” × Depth 1”

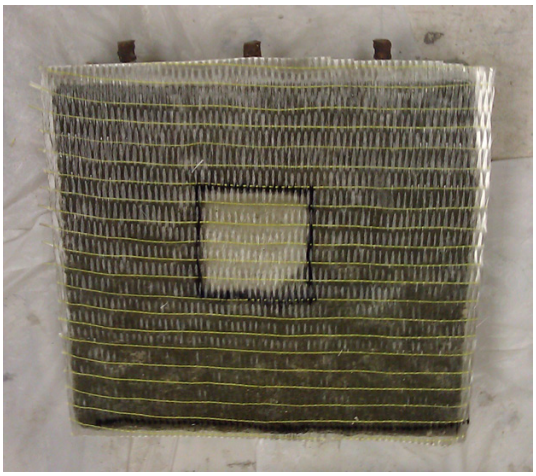

Figure 4-8: FRPP2, FRP-bonded reinforced concrete panel
Size: Height 12" × Width 12" × Depth 4"
Delamination-like defect size: Height 3" × Width 3" × Depth 0.2"

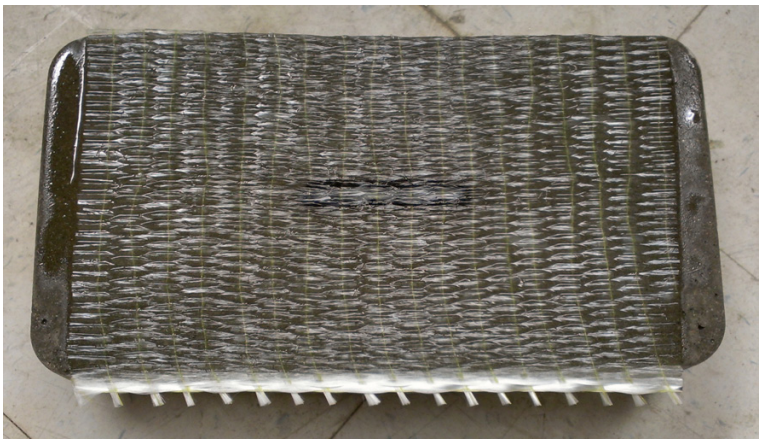

Figure 4-9: FRPP3, FRP-bonded concrete panel
Size: Height 7" × Width 13" × Depth 4"
Crack-like defect size: Height 0.25" × Width 3" × Depth 1.5"

Figure 4-10: FRPP3, FRP-bonded concrete panel
Size: Height 7” × Width 13” × Depth 4”
Angled crack-like defect size: Height 0.25” × Width 3” × Depth 1.5”,
approximately 30° angle

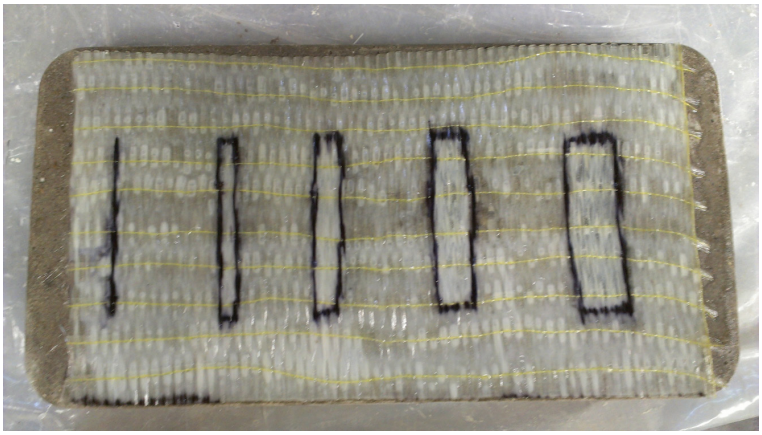

Figure 4-11: FRPP5, FRP-bonded concrete panel
Size: Height 7” × Width 13” × Depth 4”
Multiple crack-like defect sizes: Height 3” × Widths 0.125”, 0.25”, 0.5”, 0.75”, 1” ×
Depth 1.5”

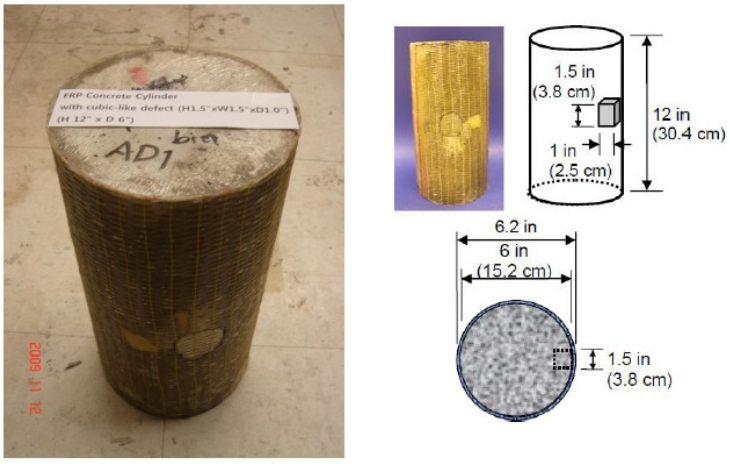

Figure 4-12: FRPC1, FRP-confined concrete cylinder
Size: Height 12" × Diameter 6"
Cubic defect size: Height 1.5" × Width 1.5" × Depth 1.0"

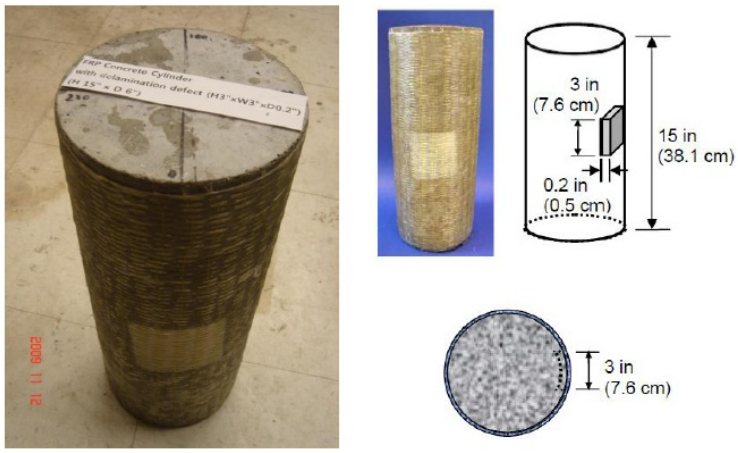

Figure 4-13: FRPC2, FRP-confined concrete cylinder
Size: Height 15" × Diameter 6"
Delamination-like defect size: Height 3" × Width 3" × Depth 0.2"

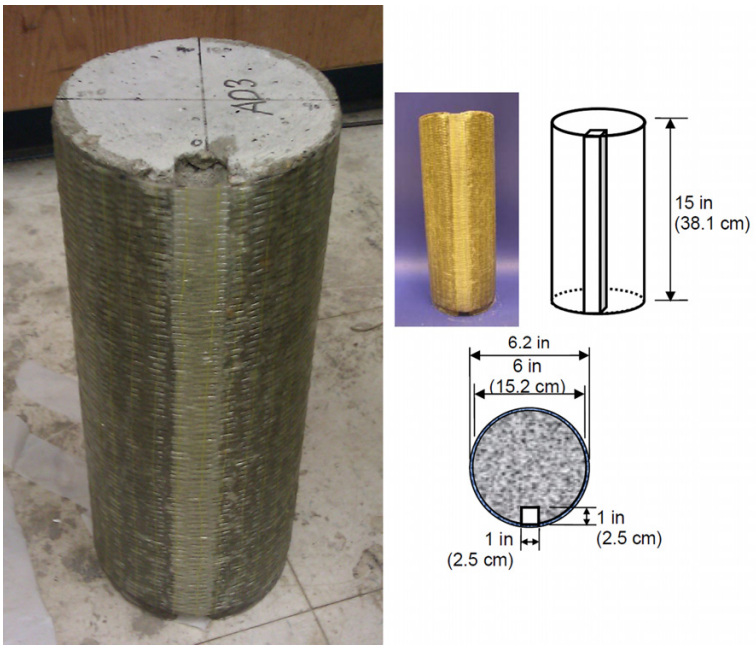

Figure 4-14: FRPCAD3, FRP-confined concrete cylinder
Size: Height 15" × Diameter 6"
Full length defect size: Height 15" × Width 1" × Depth 1"

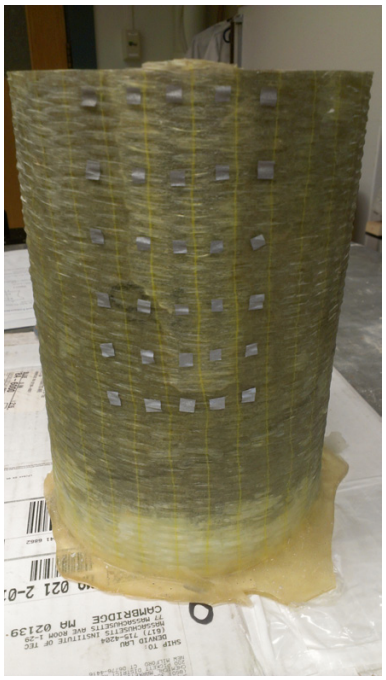

Figure 4-15: FRPC4, FRP-confined concrete cylinder
Size: Height 8" × Diameter 6"
Irregular delamination defect size: Height 5" × Width 1.5"

4.3 Experimental Setup

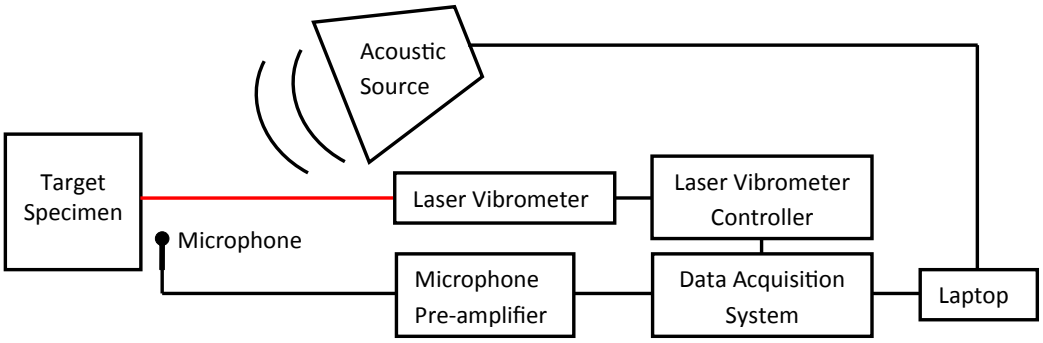

Figure 4-16: Diagram of experimental setup

The experimental setup involved a laser vibrometer, the loudspeaker, data collection equipment, and the sample under test. Figure 4-16 shows a diagram of the experimental setup. The laser vibrometer was a Polyec OFV-505 sensor head with an OFV-5000 controller, and the speaker was an M-Audio DSM1 with a ± 3 dB frequency response of 49 Hz - 27 kHz. An Earthworks M30 omnidirectional microphone with 10 Hz - 30 kHz frequency response, was used to measure the sound pressure level at the target. The data acquisition system was an IOtech 516E WaveBook connected to a laptop, operating at a sampling frequency of 50 kHz for a Nyquist frequency of 25 kHz, more than sufficient for the maximum excitation frequency of 22 kHz. The arrangement of the equipment was such that the laser vibrometer measures the sample normal to its surface to avoid any errors in the vibration magnitude. The theory predicts a flexural vibration in the defect, so the maximum amplitude will be measured normal to the surface. The speaker was placed approximate one meter away from the sample and slightly off the line of sight of the laser vibrometer to avoid obstruction of the laser. The laser vibrometer was placed about three meters away from the sample, close enough to maintain good signal strength, while avoiding acoustic coupling from the speaker into the vibrometer. Retroreflective tape, as shown in Figure 4-17 was used on the specimens

to ensure a good return signal from the specimens for the laser vibrometer. It reflects incident light back in the direction of the laser vibrometer lens instead of scattering as it would off of a diffuse surface. A picture showing the reflected light is shown in Figure 4-18.

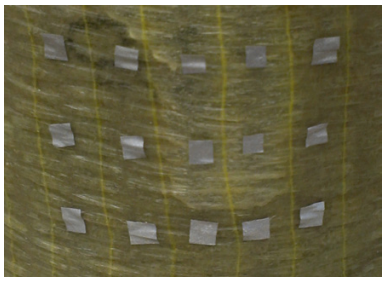

Figure 4-17: Retroreflective tape adhered to specimen

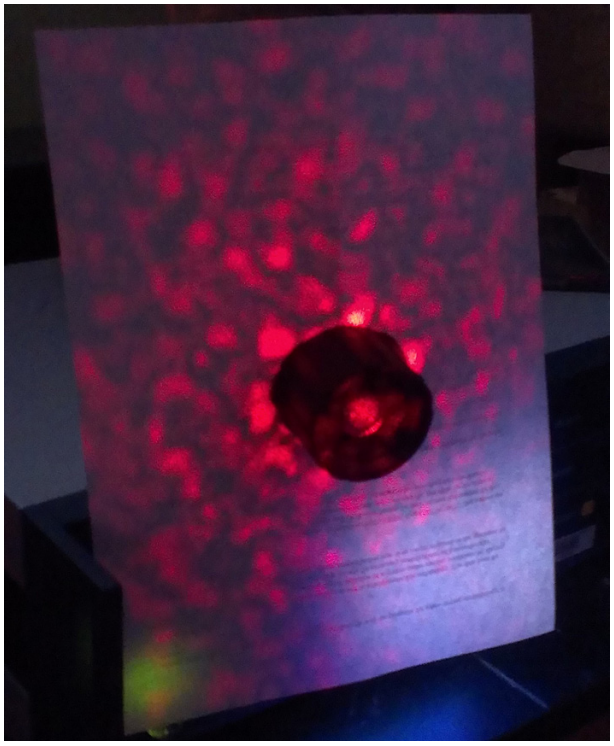

Figure 4-18: Light reflected from retroreflective tape on specimen, imaged onto paper surrounding the laser vibrometer lens

In order to determine the frequency response of the defect, measurements with the laser vibrometer were made in different locations, examples of which are shown

in Figure 4-19, while a frequency sweep was played on the loudspeaker. During the measurements the volume controls on the speaker were kept constant to maintain the same decibel level output. Amplitudes of the microphone and laser vibrometer measurement were scaled so that the resultant amplitude would be similar to that of a pure single frequency sine wave excitation. This amplitude scaling factor is the square root of the frequency sweep bandwidth times frequency sweep duration, which for a 20 kHz bandwidth and 60 second sweep duration, is 1095.445. A plot of the SPL measured at the sample as a function of frequency is shown in Figure 4-20.

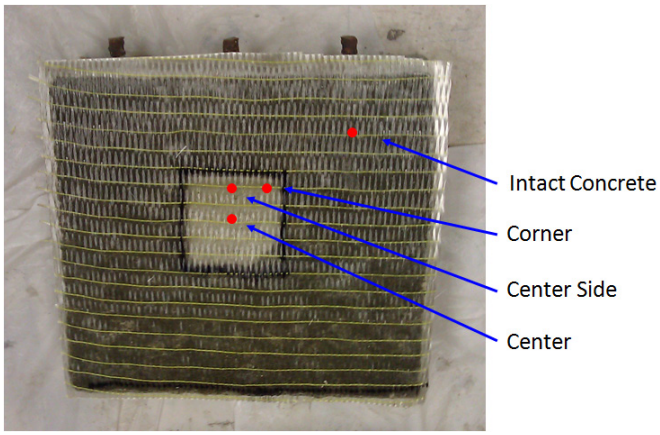

Figure 4-19: Examples of measurement locations on specimen FRPP2

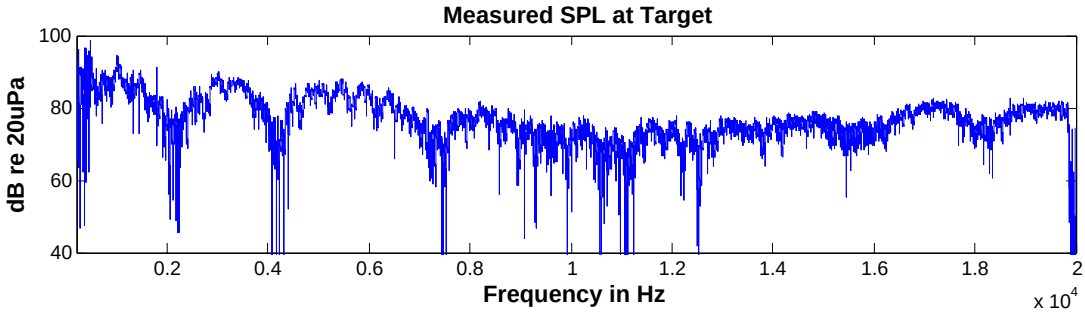

Figure 4-20: Sample measurement of sound pressure level of frequency sweep

From the calibration certificate, the M30 microphone is uniform to +1/-3 dB, and from the specifications the speaker is uniform to ±3 dB, which means that the ±10

dB uniformity of the sound power delivered to the target was likely a function of the acoustics of the room causing some frequencies to be louder than others. These variations in SPL were not great enough to cause the defect to respond with varying amplitudes that would look like a spurious resonant peak. The vibration velocity data was analyzed with a fast Fourier transform (FFT) to find resonance peaks that correspond to the resonant frequencies of the defect.

4.4 Components of Laboratory Acoustic-Laser Vibrometry System and Key Specifications

The main components of the laboratory acoustic-laser vibrometry system and key specifications are given in the following figures and tables.

Figure 4-21: Polytec Laser Vibrometer OFV-505 and Controller OFV-5000 [43]

Maximum frequency	350 kHz (100 kHz used)
Measurement ranges	1 $\frac{\frac{mm}{s}}{V}$, 2 $\frac{\frac{mm}{s}}{V}$ (used), 10 $\frac{\frac{mm}{s}}{V}$, 50 $\frac{\frac{mm}{s}}{V}$
Laser wavelength	632.8 nm
Maximum stand-off distance	300m with OFV-SLR, surface dependent
Typical spot size with OFV-LR lens	62 μm (1m), 135 μm (2m), 356 μm (3m)
Resolution, Frequency dependent	0.01 - 0.04 $\frac{\frac{\mu m}{s}}{\sqrt{Hz}}$ or 0.02 typical
Calibration error	$\pm$1%
Frequency dependent amplitude error	$\pm$0.05 dB

Table 4.3: Polytec Laser Vibrometer system specifications [44, 45]

Figure 4-22: M-Audio DSM1 Studio Monitor [46]

LF Driver	6.5-inch aluminum cone woofer
HF Driver	1-inch soft teteron dome tweeter
Frequency Response	49 Hz - 27 kHz ±3 dB
Max SPL @ 1 meter	110 dB maximum peak SPL @ 1m
Dimensions H×W×D	12.8" × 9" × 10.3"

Table 4.4: M-Audio DSM1 Studio Monitor specifications [47]

Figure 4-23: WaveBook/516E Data Acquisition System [48]

Analog Inputs	8 differential
Resolution	16 bit
Maximum Frequency (per unit)	1 MHz
Ranges	±10V, ±5V, ±2V, ±1V
Accuracy	±5V: ±0.012% of reading; 0.006% of range
Total Harmonic Distortion	-84 dB typ
Signal to Noise and Distortion	+74 dB typ
Dimensions W×D×H	11” × 8.5” × 2.7”

Table 4.5: WaveBook/516E Data Acquisition System specifications [48]

Figure 4-24: Earthworks M30 Microphone [49]

Frequency response	5Hz to 30kHz +1/-3dB
Polar pattern	Omnidirectional
Sensivitity	$30\frac{mV}{Pa}$ (Typical), $34\frac{mV}{Pa}$ (Actual)
Peak Acoustic Input	142dB SPL
Dimensions L×D	9” × 0.86”

Table 4.6: Earthworks M30 Microphone specifications [50]

Figure 4-25: Earthworks 1021 Microphone Pre-amp [49]

Frequency Response	2Hz to 100kHz ±0.1dB, 1Hz to 200kHz ±0.5dB
Equivalent Input Noise	-132dBV @ 20dB gain; -143dBV @ 60dB gain
Max. Output Level	+33dBu (37V peak-to-peak)
Dimensions H×W×D	1.75” × 9.5” × 10.3.75”

Table 4.7: Earthworks 1021 Microphone Pre-amp specifications [51]

Chapter 5

Defect Measurements

5.1 Preliminary Measurements

Preliminary measurements were made on the specimen, FRPP0 that has no defects to confirm that there was no resonant frequency vibration response when the FRP-concrete system is intact. In these measurements no amplitude normalization constant was used so the amplitudes were the raw values from the laser vibrometer scaled by the 2000 micrometers per second, per Volt ($\frac{\frac{\mu m}{s}}{V}$) scale factor. This scaling factor was selected to ensure that the vibration would not clip during measurement.

In the background measurement in Figure 5-1, the microphone records minimal background sound and the vibrometer has a flat noise floor except for three very narrow peaks. When a 60 second 0 - 20 kHz frequency sweep was used to excite the specimen as shown in Figure 5-2, the noise floor was actually lower, possibly due to a change in the laser signal received from the defect. Similarly three very narrow peaks were in the frequency response. Since they appear in both the passive background and active frequency sweep measurement, and they have very narrow widths, they must be due to some sort of noise in the system. If they are present in the passive background measurement where the specimen is not being acoustically excited, they are not due to a surface vibration of the specimen. Any resonance peak due to some physical measured feature, would have an associated damping, characterized in the frequency peak by the full width at half maximum (FWHM). Since the peaks were

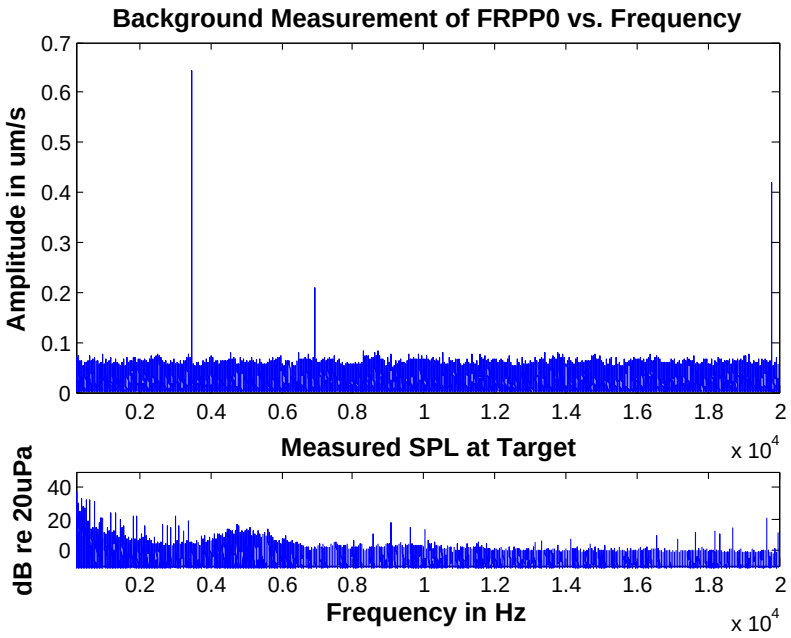

Figure 5-1: Background measurement of FRPP0

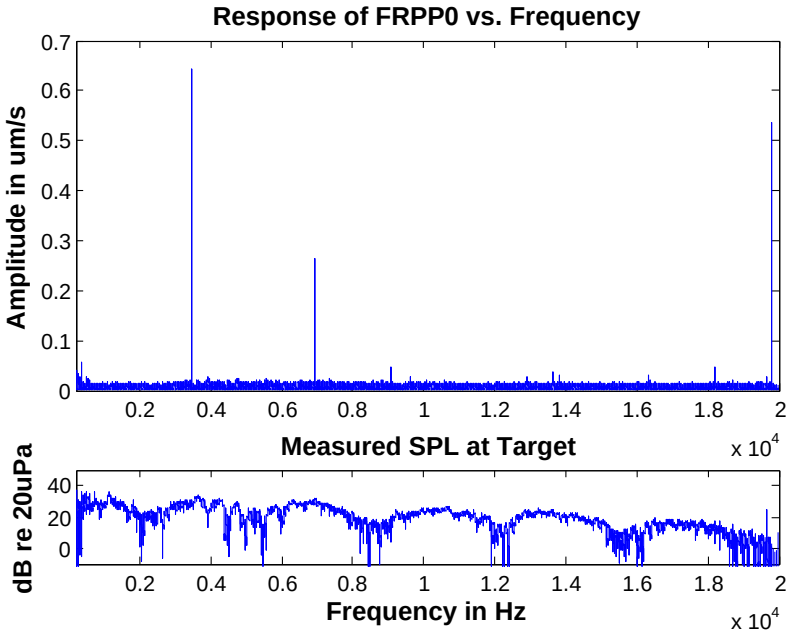

Figure 5-2: Frequency sweep measurement of FRPP0

very narrow, they are not due to some physically measured feature. It is likely that the noise peaks are due to some sort of electrical noise that would exhibit such a narrow peak. Similar peaks are seen throughout all the plots and are a sort of system noise that appears in the measurements and can be ignored. Measurements over areas where the FRP is well bonded to the concrete are given for each specimen, so the comparison can be made between defective and intact areas to ensure that the peaks seen are true resonant peaks of the defect.

5.2 Frequency Sweep Defect Measurements

For the initial measurements, a determination of the resonant frequencies of the defects on the specimens was conducted. Typically a 60 second measurement was done, where the laser vibrometer measured the surface vibration at a point on the defect, and a 0 - 20 kHz bandwidth frequency sweep excitation was played over the speaker. In some cases only a 10 second measurement or a 2 kHz - 22 kHz frequency sweep bandwidth was used. The defect on the specimen was measured in three locations: center of defect, side of defect, and corner of defect. These measurement locations were chosen to obtain both the maximal response amplitude and the most varied frequency responses from the defect. The response vibration amplitudes were scaled by a normalization factor, the square root of the sweep bandwidth times the sweep duration. A measurement was also made in an area of the specimen where the FRP-concrete system was undamaged and intact, for a control vibration signature that identifies peaks due to noise. The following figures show the response velocity frequency spectrums of these measurements for different specimens.

5.2.1 FRPP1

FRPP1 is a concrete panel specimen with a 1.5" $\times$ 1.5" square defect with a depth of 1". The predicted resonant frequency is approximately 5 kHz from either plate theory or finite element analysis, as previously determined. A 60 second 0 - 20 kHz bandwidth frequency sweep was used to acoustically excite the specimen.

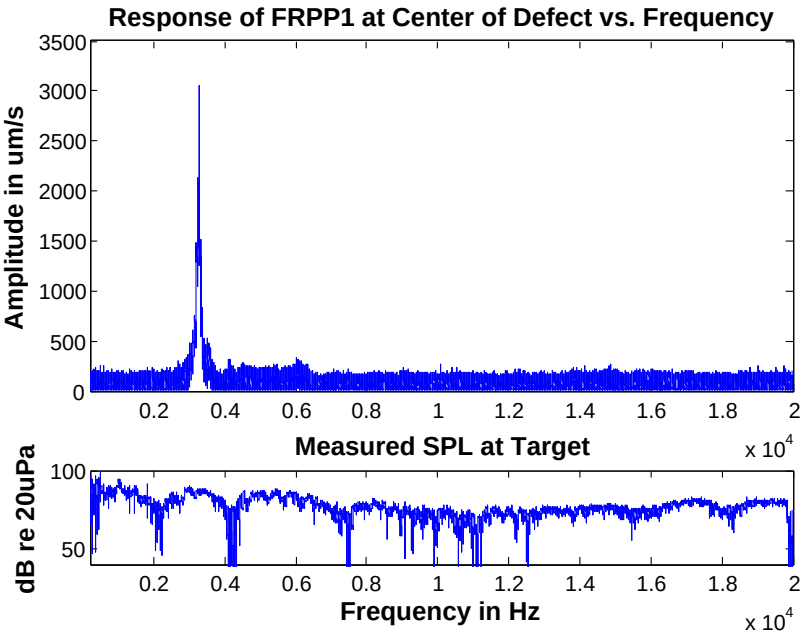

Figure 5-3: Frequency response of FRPP1 at center of defect

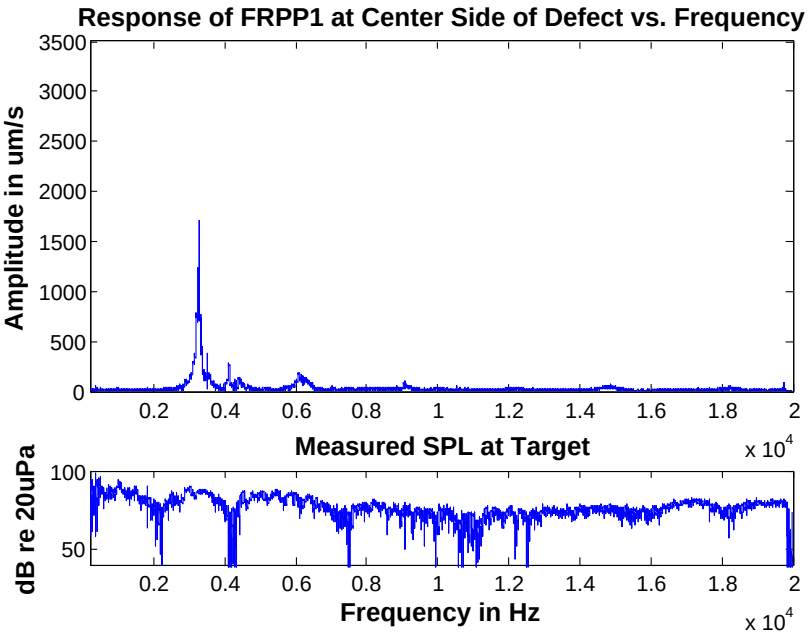

Figure 5-4: Frequency response of FRPP1 at center side of defect

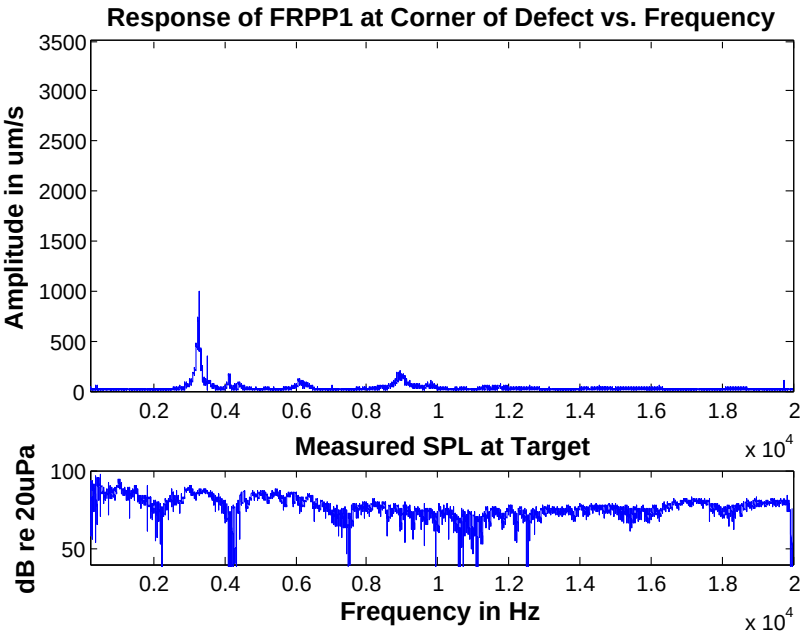

Figure 5-5: Frequency response of FRPP1 at corner of defect

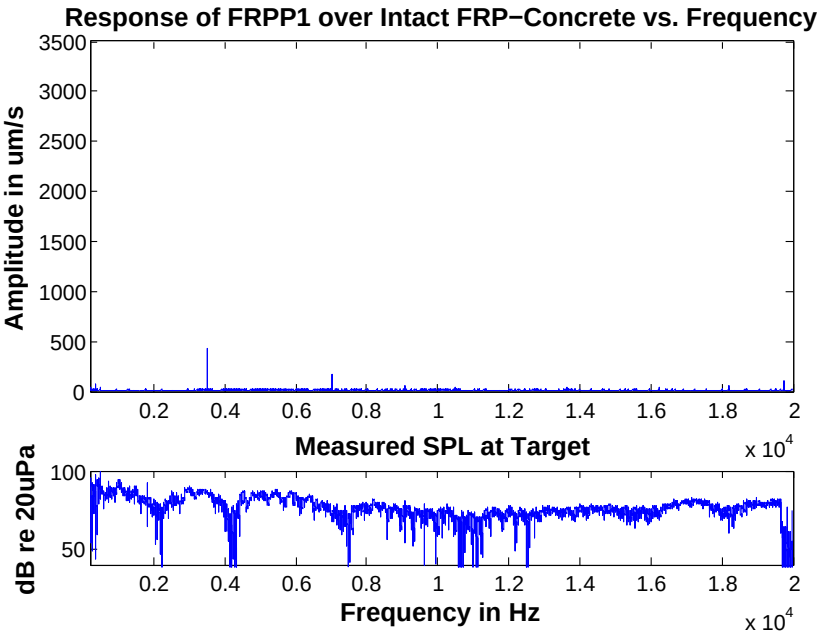

Figure 5-6: Frequency response of FRPP1 over intact FRP-concrete system

The base frequency observed of 3.2 kHz in Figure 5-3 was comparable to the predicted resonant frequency of 5 kHz from finite element analysis, especially when taking into consideration the possible variances in the material properties of the FRP. Also the theory considered an isotropic material, while in reality, FRP is less stiff in the direction perpendicular to the fibers, resulting in a lower actual resonance frequencies. These plots also show that there was a significant difference in the observed response whether the measurement was made on or off of the defect. Over the center of the defect, the scaled response velocity was upwards of 3000 $\frac{\mu m}{s}$, while over the intact FRP-concrete system, the noise floor was under 20 $\frac{\mu m}{s}$. The response amplitude was much greater over the defect, and Figures 5-3, 5-4, and 5-5 show distinct resonant peaks whereas the measurement over intact concrete in Figure 5-6 shows only a noise floor with some extraneous peaks due to noise.

Frequency (kHz) Location	3.2	4.1	6.1	8.9	14.8
Center	•	•	•		
Center Side	•	•	•		•
Corner	•	•	•	•	

Table 5.1: Visually determined resonant frequencies for specimen FRPP1

5.2.2 FRPP2

FRPP2 is a concrete panel specimen with a 3" × 3" square defect with a depth of 0.2". The predicted resonant frequency is approximately 1.3 kHz from plate theory. A 60 second 0 - 20 kHz bandwidth frequency sweep was used to acoustically excite the specimen.

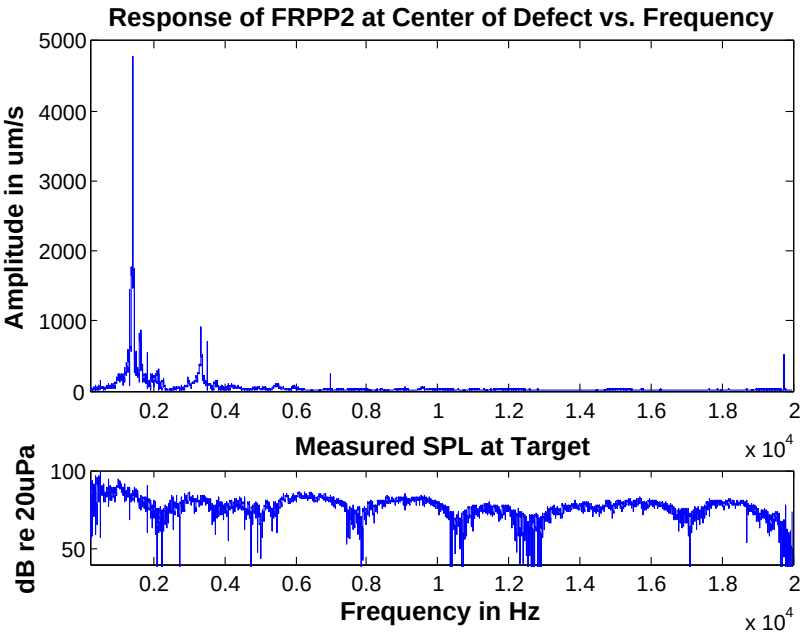

Figure 5-7: Frequency response of FRPP2 at center of defect

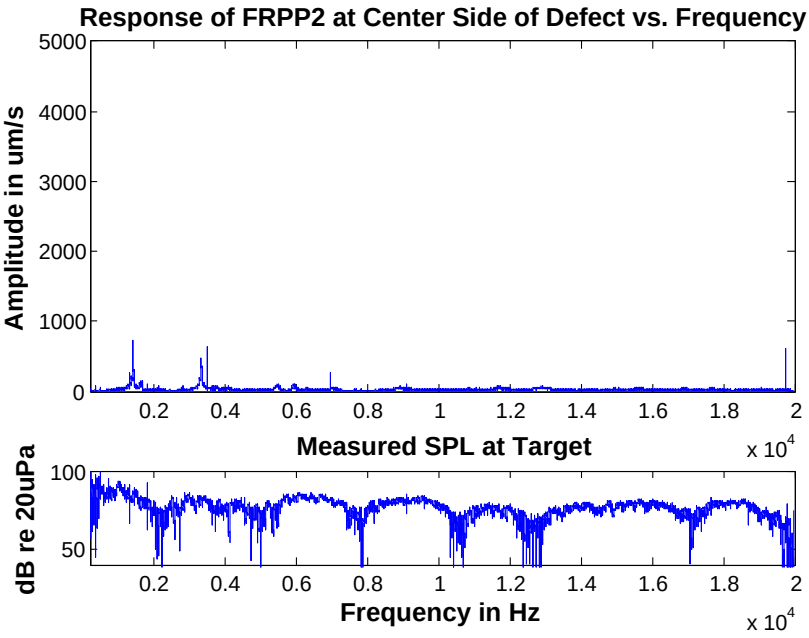

Figure 5-8: Frequency response of FRPP2 at center side of defect

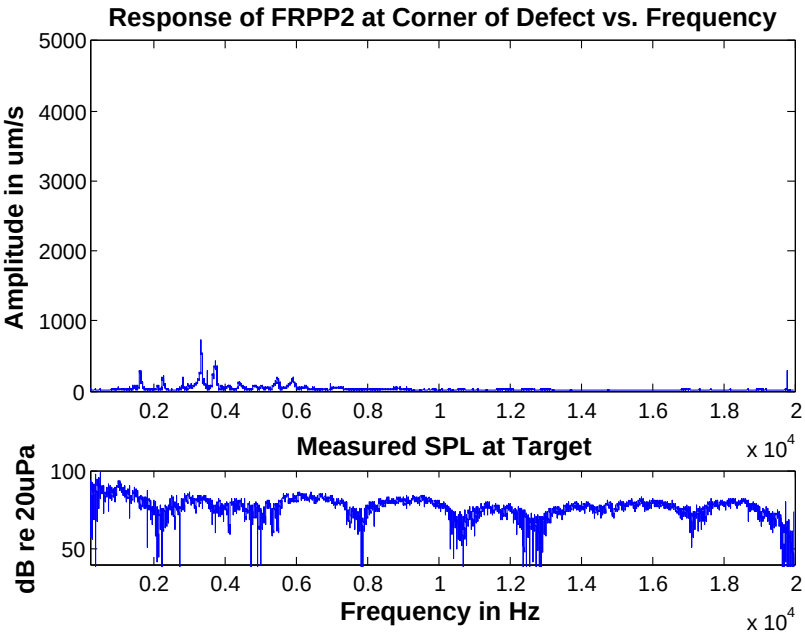

Figure 5-9: Frequency response of FRPP2 at corner of defect

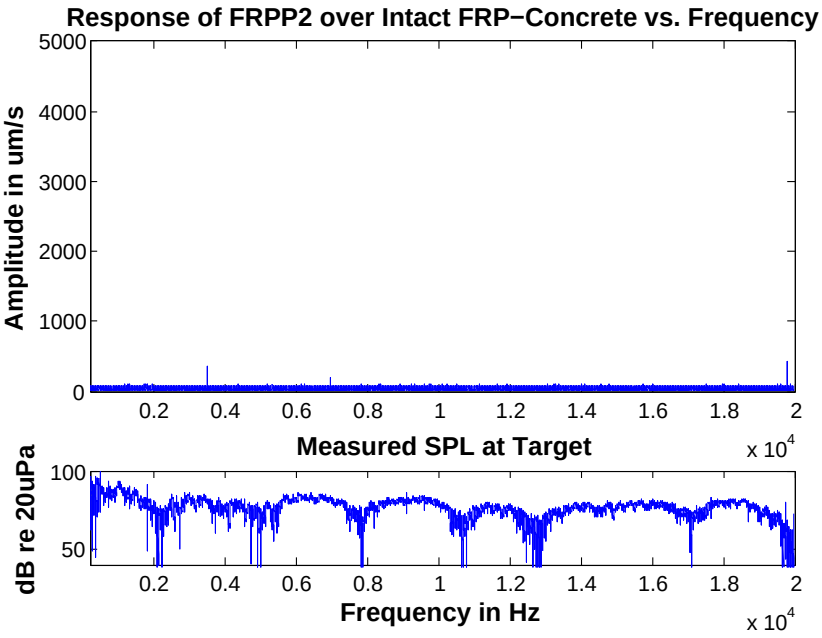

Figure 5-10: Frequency response of FRPP2 over intact FRP-concrete system

The base frequency observed of 1380 Hz in Figure 5-7 was comparable to the estimated predicted resonant frequency of 1288 Hz from plate theory, when taking into consideration the possible variances in the material properties of the FRP. These plots also show that the response amplitude was much greater over the defect, with distinct resonant peaks of scaled response velocities ranging from 100 $\frac{\mu m}{s}$ to upwards of 4500 $\frac{\mu m}{s}$. There was a clear distinction between a measurement made over a defect or over intact FRP-concrete system.

Frequency (kHz) Location	1.4	1.6	2.3	2.8	3.3	3.7	4.4	5.5	5.9	7.0	8.9
Center	•	•			•						
Center Side	•	•			•	•	•	•	•	•	•
Corner		•	•	•	•	•	•	•	•	•	•

Table 5.2: Visually determined resonant frequencies for specimen FRPP2

5.2.3 FRPC1

FRPC1 is a concrete cylinder specimen with a 1.5" × 1.5" square defect with a depth of 1". The predicted resonant frequency is approximately 7.9 kHz from finite element analysis. A 60 second 0 - 20 kHz bandwidth frequency sweep was used to acoustically excite the specimen.

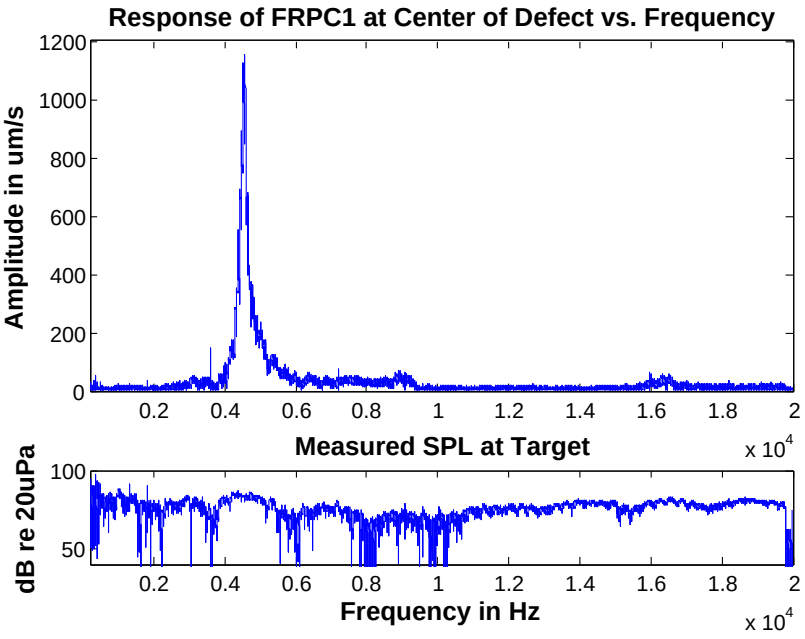

Figure 5-11: Frequency response of FRPC1 at center of defect

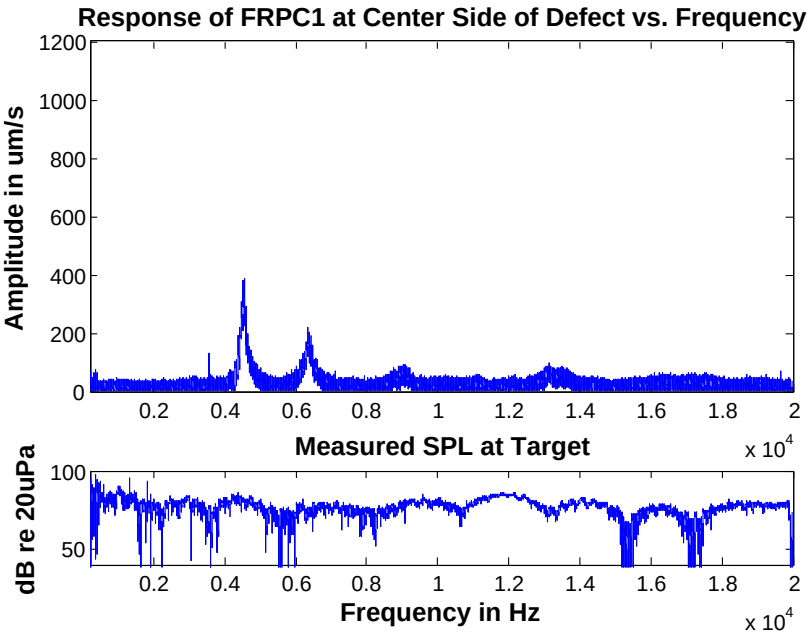

Figure 5-12: Frequency response of FRPC1 at center side of defect

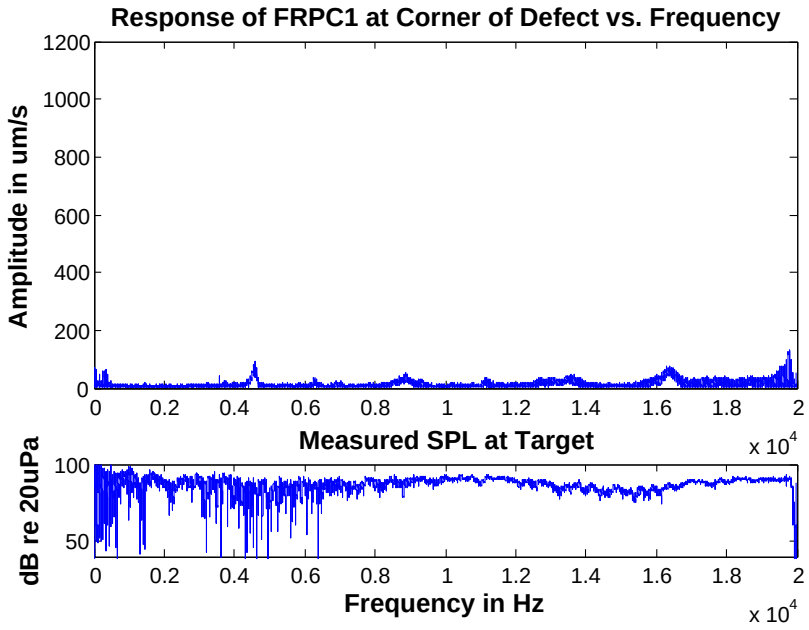

Figure 5-13: Frequency response of FRPC1 at corner of defect

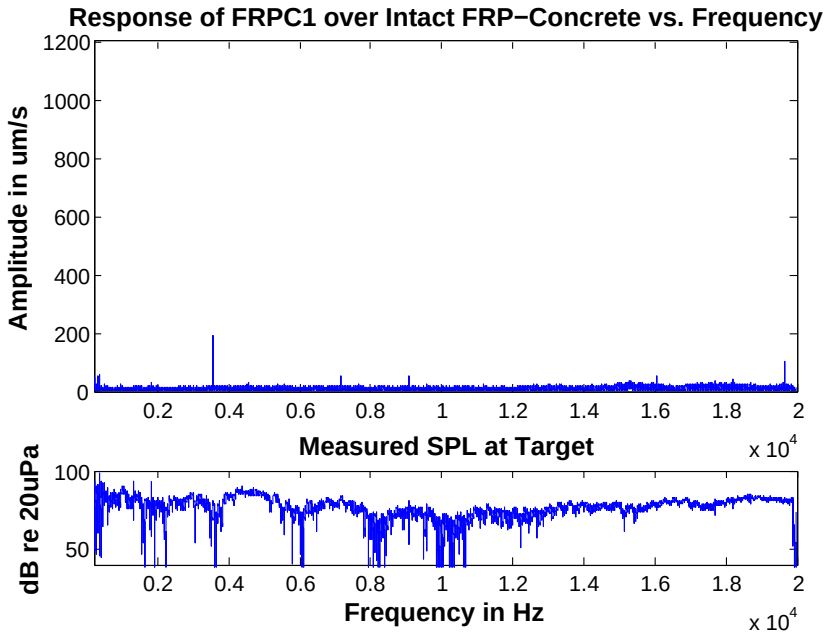

Figure 5-14: Frequency response of FRPC1 over intact FRP-concrete system

The base frequency observed of 4.5 kHz in Figure 5-11 was less than, but comparable to the estimated predicted resonant frequency of 7.9 kHz from finite element analysis, when taking into consideration the possible variances in the material properties of the FRP and possible inaccurate modeling of the curvature. These plots also show that the response amplitude was much greater over the defect with a scaled vibration response amplitude of 1100 $\frac{\mu m}{s}$ over the center of the defect. There was a clear distinction between a measurement made over a defect or over intact FRP-concrete system.

Frequency (kHz) Location	4.5	6.3	8.9	11.2	13.0	13.2	16.3	19.8
Center	•		•				•	
Center Side	•	•	•		•			
Corner	•	•	•	•	•	•	•	•

Table 5.3: Visually determined resonant frequencies for specimen FRPC1

5.2.4 FRPC2

FRPC2 is a concrete cylinder specimen with a 3" × 3" square defect with a depth of 0.2". The predicted resonant frequency is approximately 3.75 kHz from finite element analysis. A 60 second 0 - 20 kHz bandwidth frequency sweep was used to acoustically excite the specimen.

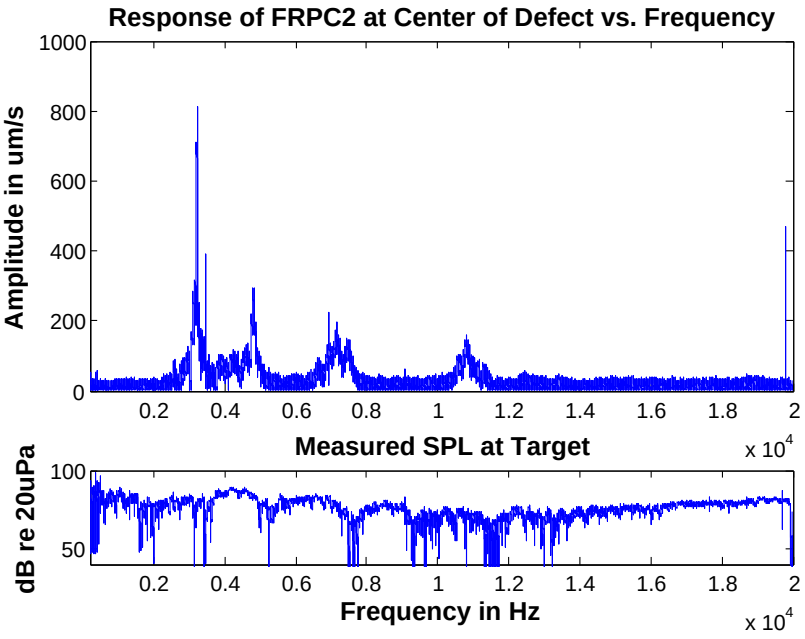

Figure 5-15: Frequency response of FRPC2 at center of defect

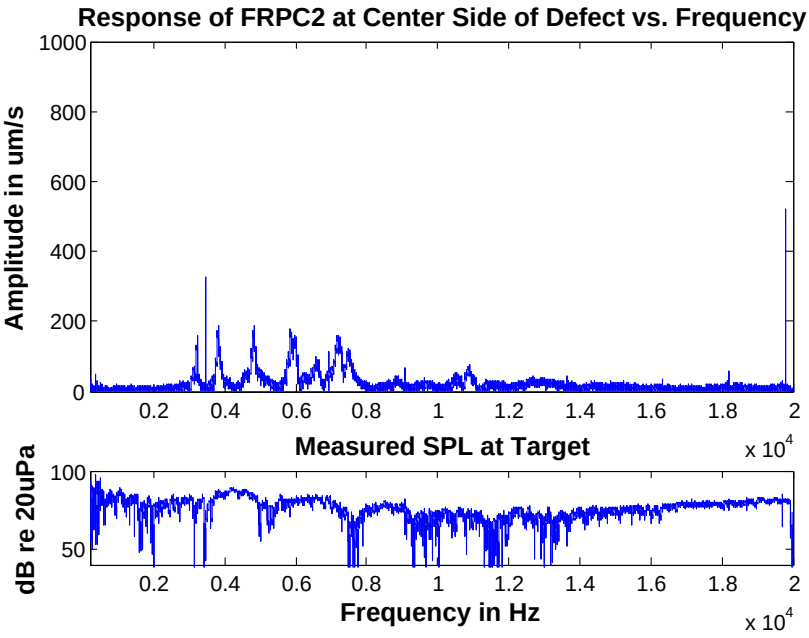

Figure 5-16: Frequency response of FRPC2 at center side of defect

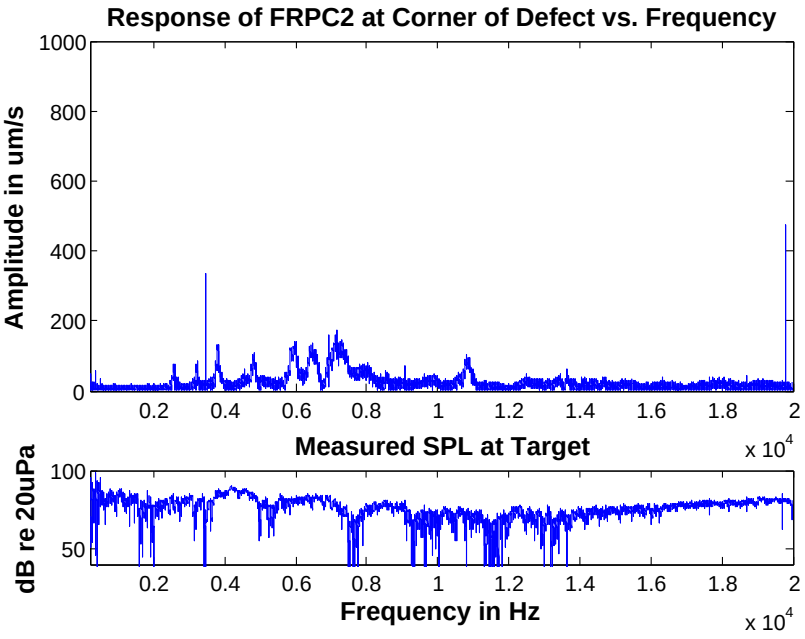

Figure 5-17: Frequency response of FRPC2 at corner of defect

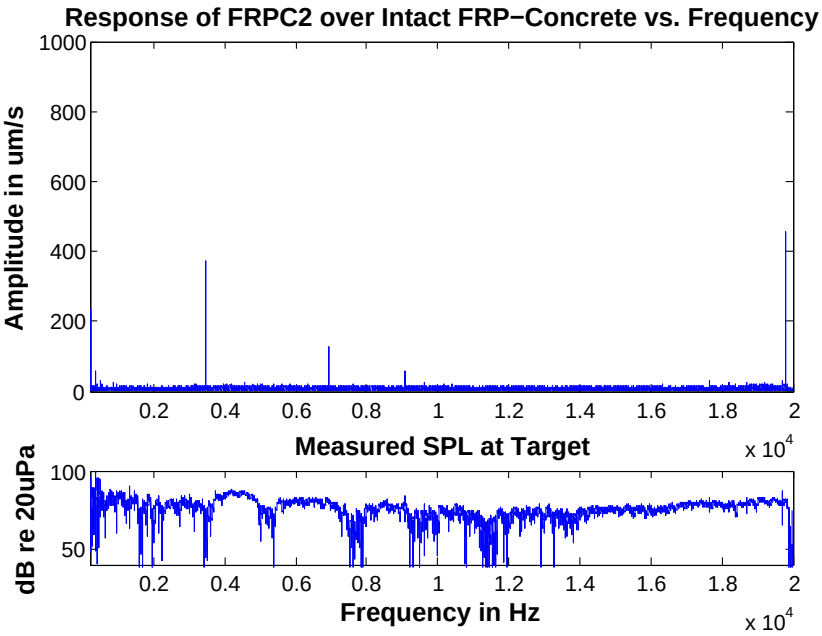

Figure 5-18: Frequency response of FRPC2 over intact FRP-concrete system

The base frequency observed of 3.2 kHz in Figure 5-15 was comparable to the estimated predicted resonant frequency of 3.75 kHz from finite element analysis. These plots also show that the response amplitude was much greater over the defect with a scaled vibration response amplitude of 800 $\frac{\mu m}{s}$ over the center of the defect. There was a clear distinction between a measurement made over a defect or over intact FRP-concrete system.

Frequency (kHz) Location	2.6	3.2	3.8	5.8	5.95	6.5	6.8	7.2	7.5	10.8
Center		●		●		●	●	●	●	●
Center Side		●	●	●	●	●	●	●	●	
Corner	●	●	●	●	●	●	●	●	●	●

Table 5.4: Visually determined resonant frequencies for specimen FRPC2

5.2.5 FRPCAD3

FRPCAD3 is a concrete cylinder specimen with a 15" × 1" full length defect with a depth of 1". A 60 second 0 - 20 kHz bandwidth frequency sweep was used to acoustically excite the specimen.

The base frequency observed was 6 kHz with a scaled vibration amplitude of 600 $\frac{\mu m}{s}$.

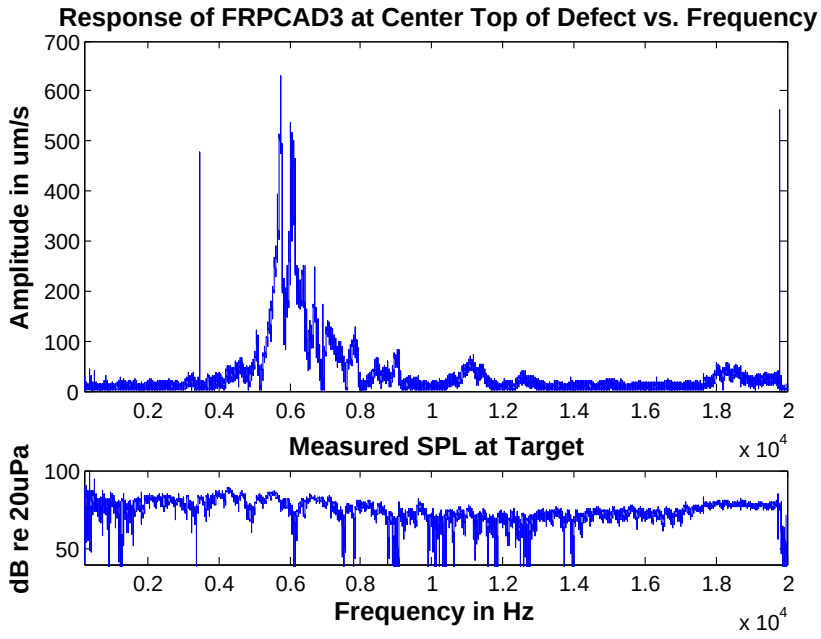

Figure 5-19: Frequency response of FRPCAD3 at center top of defect

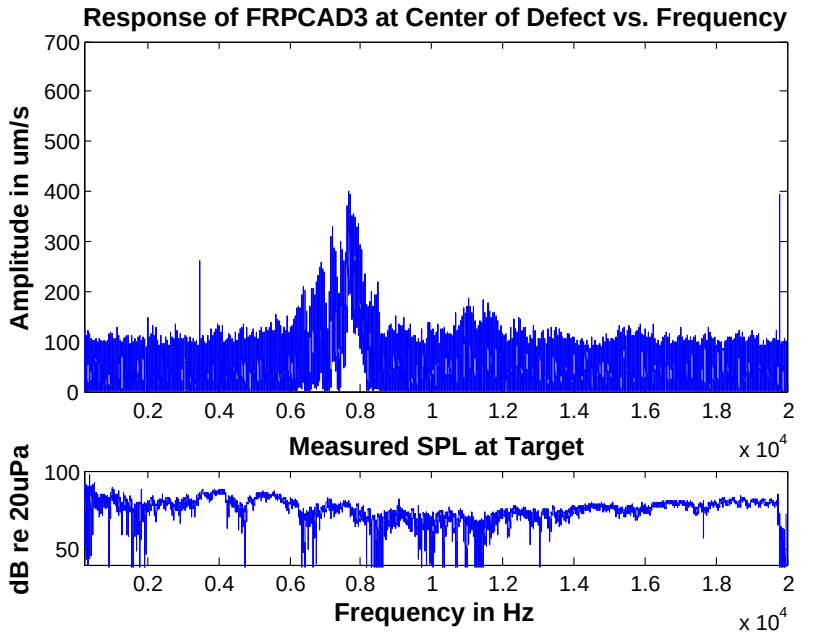

Figure 5-20: Frequency response of FRPCAD3 at center of defect

Frequency (kHz) Location	5.1	5.7	6.0	6.7	7.8	9.0	11.1	12.6	18.3
Top Center	●	●	●	●	●	●	●	●	●
Center				●	●		●		

Table 5.5: Visually determined resonant frequencies for specimen FRPCAD3

5.2.6 FRPC4

FRPC4 is a concrete cylinder specimen with an irregular 5" × 1.5" delamination. A 10 second 0 - 20 kHz bandwidth frequency sweep was used to acoustically excite the specimen.

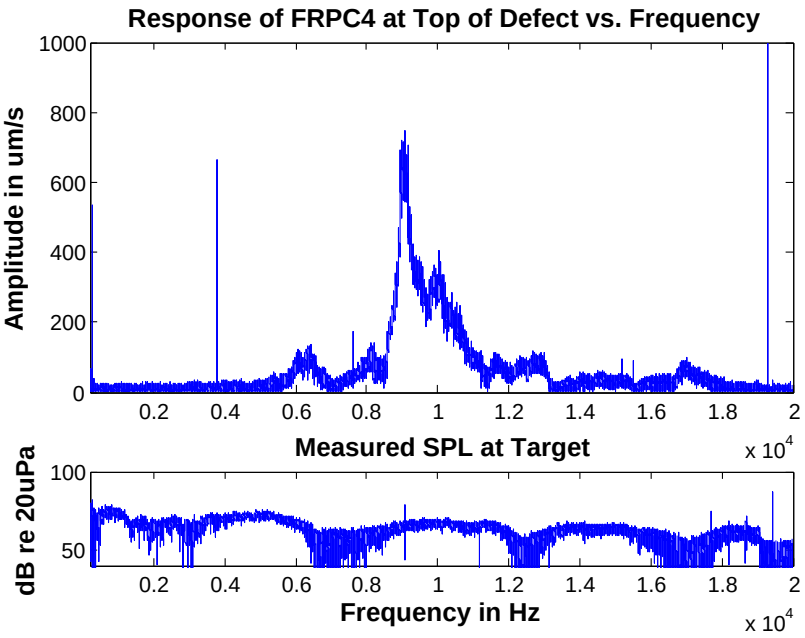

Figure 5-21: Frequency response of FRPC4 at top of defect

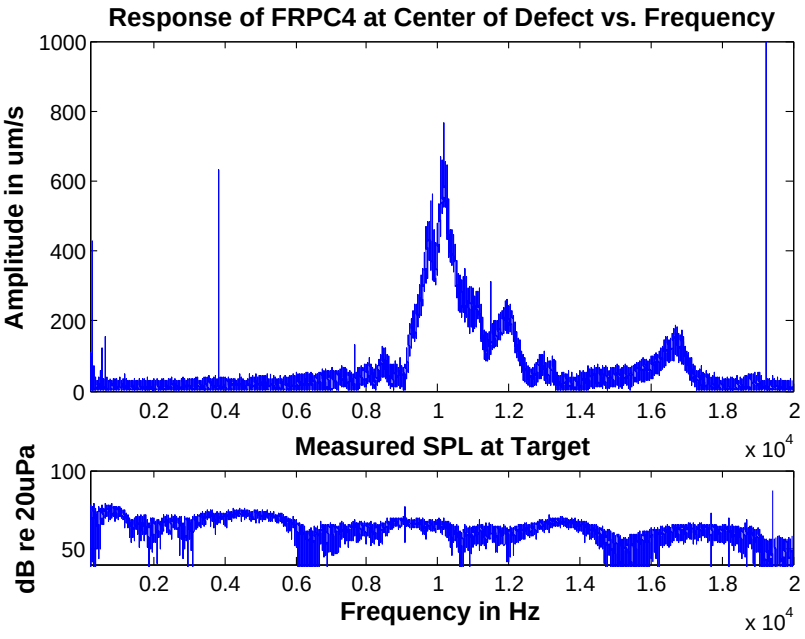

Figure 5-22: Frequency response of FRPC4 at center of defect

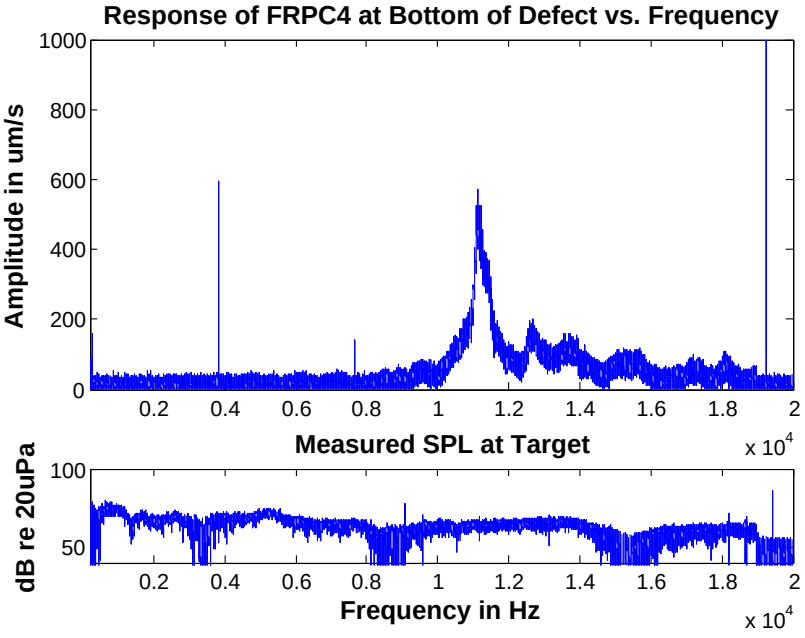

Figure 5-23: Frequency response of FRPC4 at bottom of defect

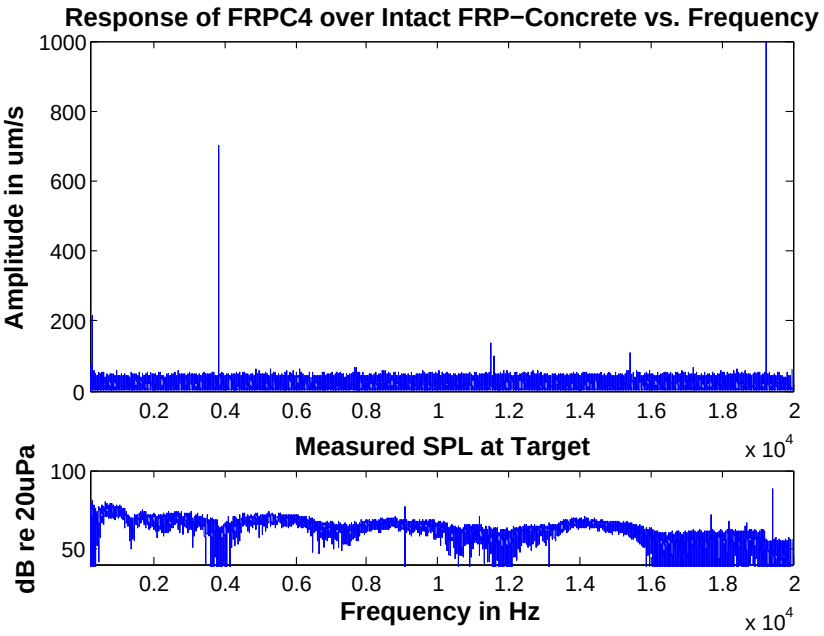

Figure 5-24: Frequency response of FRPC4 over intact FRP-concrete system

Since this defect was more irregular, no clear base resonant frequency was observed. At the top of the defect the 9 kHz peak was strongest with an amplitude of 700 $\frac{\mu m}{s}$. At the center of the defect the 10.2 kHz peak was strongest with an amplitude of 700 $\frac{\mu m}{s}$. At the bottom of the defect the 11.1 kHz peak was strongest with an amplitude of 500 $\frac{\mu m}{s}$.

Frequency (kHz) Location	6.2	8.1	9.0	9.9	10.2	11.1	12.0	12.7	17.0
Top	●	●	●	●				●	●
Center		●		●	●		●	●	●
Bottom						●		●	

Table 5.6: Visually determined resonant frequencies for specimen FRPC4

5.2.7 FRPP3

FRPP3 is a concrete panel specimen with a 0.25" × 3" defect. A 60 second 2 - 22 kHz bandwidth frequency sweep was used to acoustically excite the specimen.

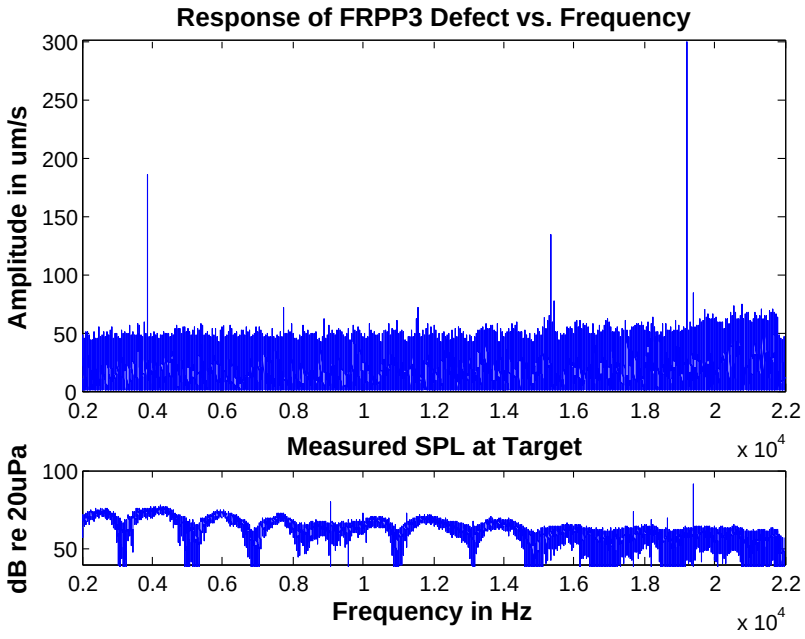

Figure 5-25: Frequency response of FRPP3 over defect

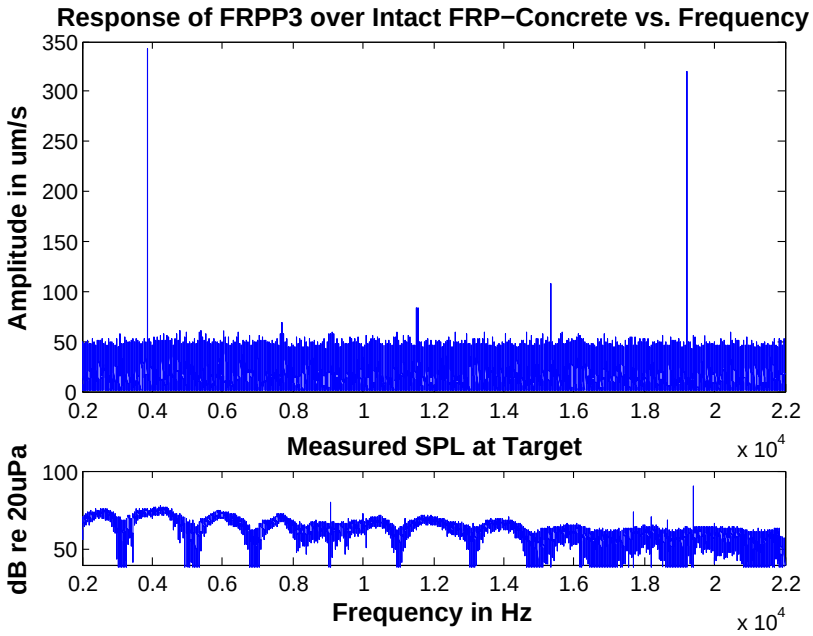

Figure 5-26: Frequency response of FRPP3 over intact FRP-concrete system

No resonant peaks were clear from the frequency response velocity spectrums for the 0.25" wide defect. There may be a limit as to the minimum width of a crack or defect in the concrete under the FRP cover that the method can detect.

5.2.8 FRPP4

FRPP4 is a concrete panel specimen with a 0.25" × 3" angled defect. A 60 second 2 - 22 kHz bandwidth frequency sweep was used to acoustically excite the specimen. The cracked region measured refers to an area over the defect where the FRP-concrete is intact, however the crack extends underneath the location just less than a centimeter.

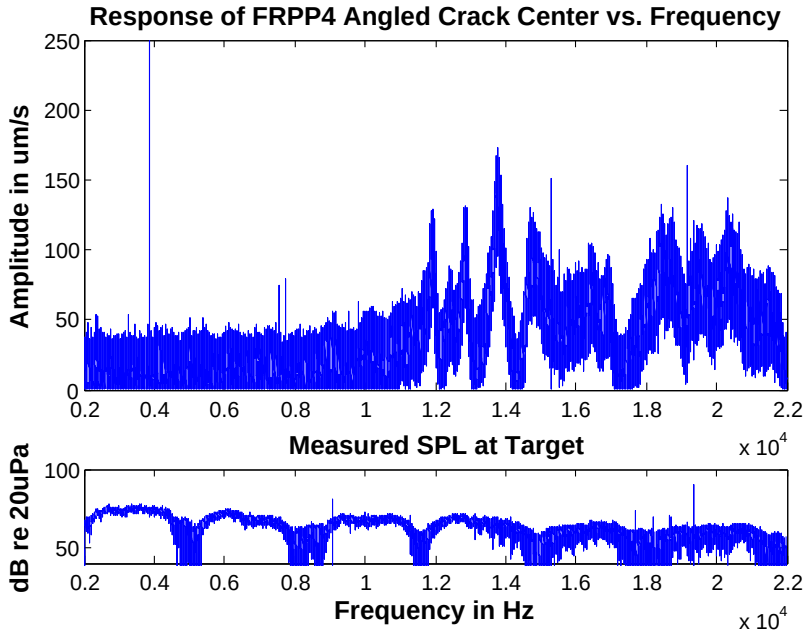

Figure 5-27: Frequency response of FRPP4 at center of defect

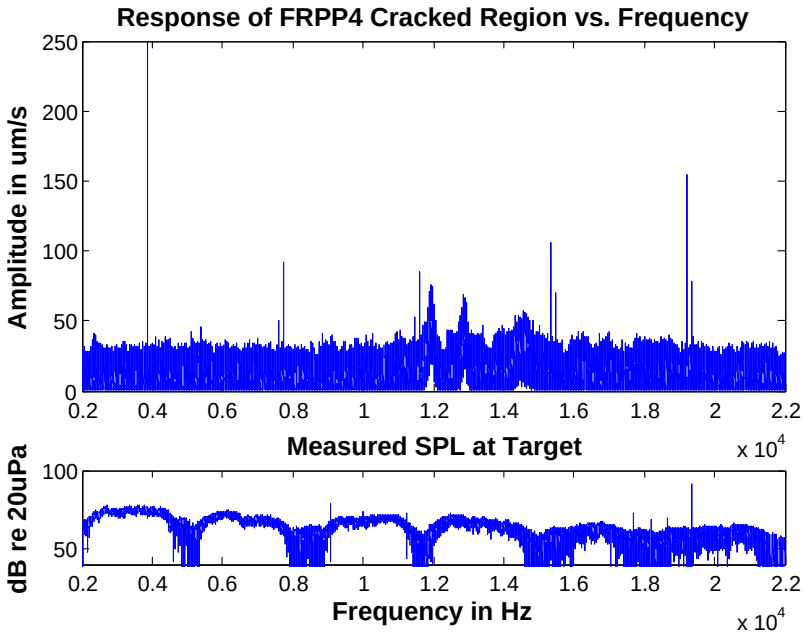

Figure 5-28: Frequency response of FRPP4 over internally cracked region

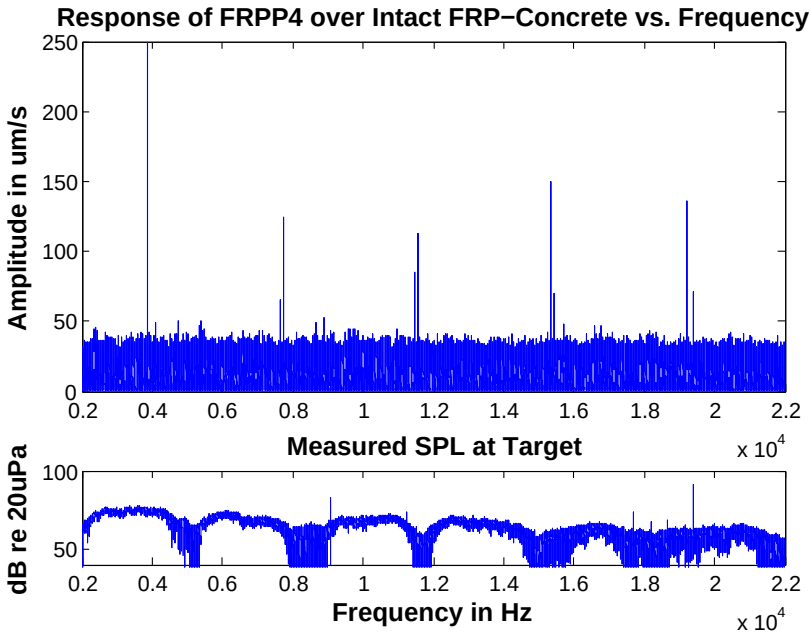

Figure 5-29: Frequency response of FRPP4 over intact FRP-concrete system

Over the FRP-covered void of the crack, the response amplitude of the defect was greater than 100 $\frac{\mu m}{s}$ at many frequencies. The cracked region did exhibit a small response at some of the resonant frequencies seen over the crack, at double the amplitude of the noise floor. This was interesting because in that location the FRP was still bonded to the concrete, although there was a crack approximately 1 cm below the surface.

Frequency (kHz) Location	11.9	12.9	13.8	14.7	16.4	18.6	19.5	20.3
Center	•	•	•	•	•	•	•	•
Cracked Region	•	•		•				

Table 5.7: Visually determined resonant frequencies for specimen FRPP4

5.2.9 FRPP5

FRPP5 is a concrete panel specimen with multiple widths of 3" long defects. The purpose of these measurements is to determine the smallest crack width that exhibits a detectable response vibration amplitude. A 60 second 2 - 22 kHz bandwidth frequency sweep was used to acoustically excite the specimen. Additional plots over different areas of the 1" wide and 0.75" wide defects are given in Appendix A, Section A.1.1.

FRPP5 Intact Region

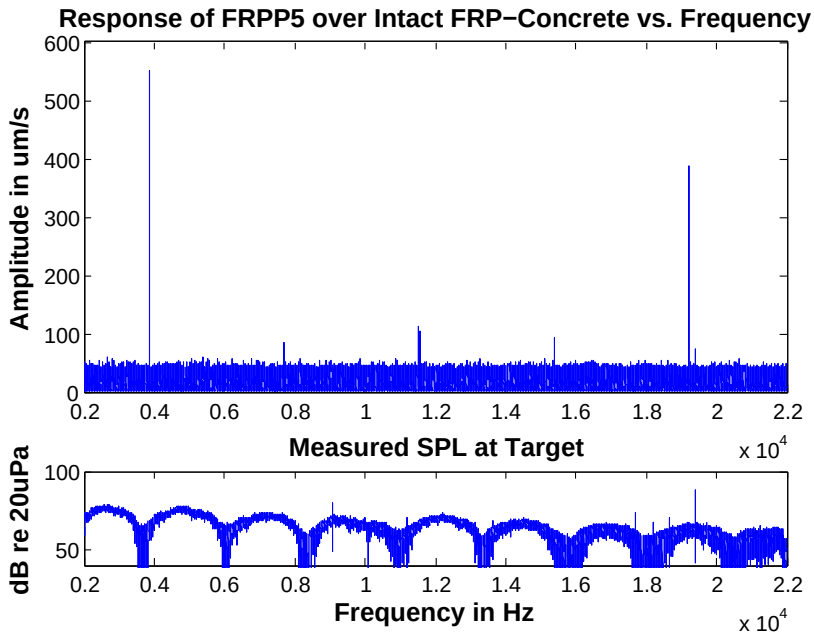

Figure 5-30: Frequency response of FRPP5 over intact FRP-concrete system

Figure 5-30 shows the response over the intact region of the specimen to show the expected noise peaks.

FRPP5 1" × 3" Defect

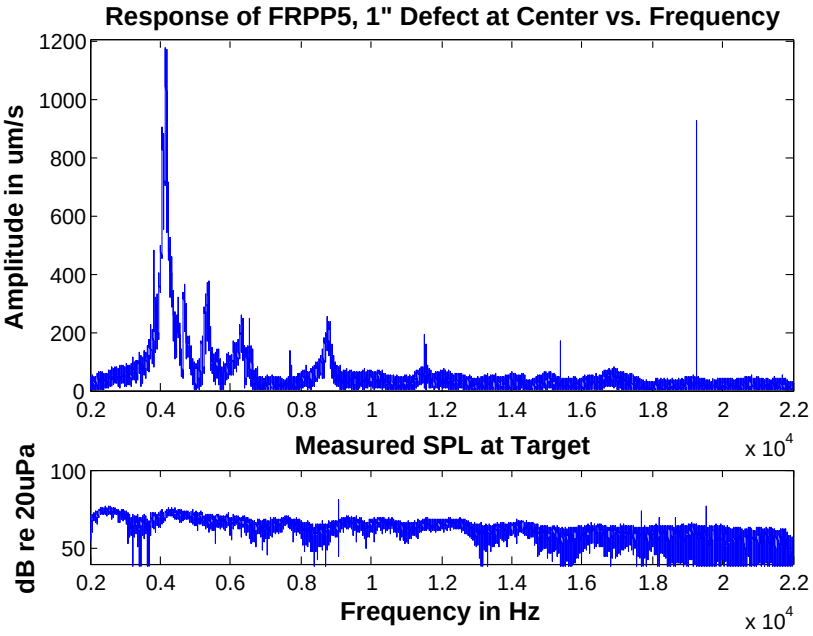

Figure 5-31: Frequency response of FRPP5 at center of 1" wide crack defect

There was a clear resonance peak at 4.1 kHz with a scaled velocity of 1150 $\frac{\mu m}{s}$. This was clearly distinguishable from the intact area of FRP-concrete system.

FRPP5 0.75” × 3” Defect

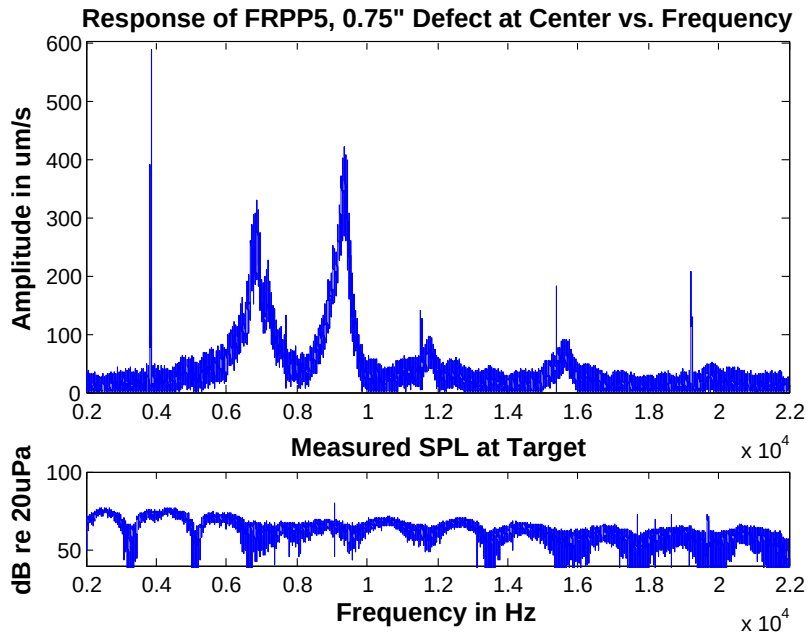

Figure 5-32: Frequency response of FRPP5 at center of 0.75” wide crack defect

There were two clear resonance peaks at 6.8 kHz and 9.4 kHz with scaled amplitudes of 300 $\frac{\mu m}{s}$ and 400 $\frac{\mu m}{s}$. These peaks were clearly distinguishable from the intact area of FRP-concrete system.

FRPP5 0.5" × 3" Defect

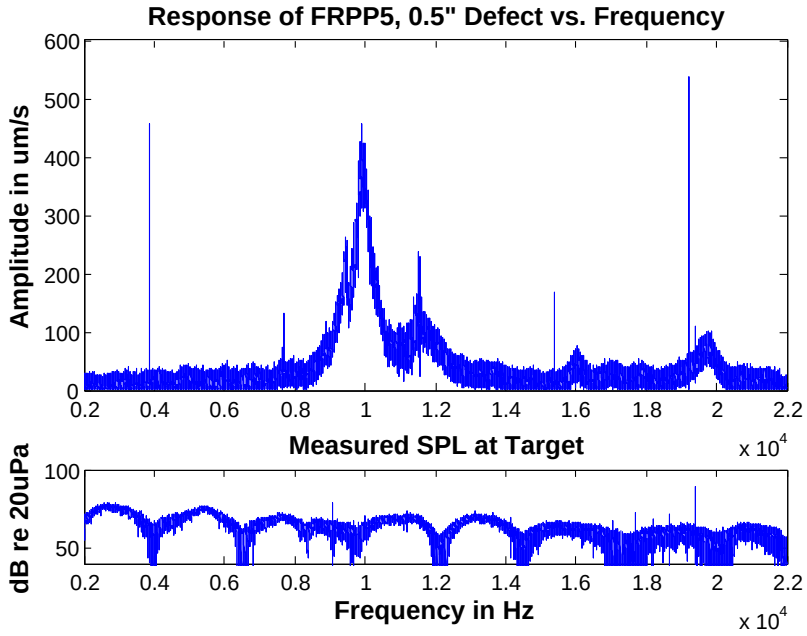

Figure 5-33: Frequency response of FRPP5 at center of 0.5" wide crack defect

There was a clear resonance peak at 10 kHz with a scaled velocity of 400 $\frac{\mu m}{s}$. This was clearly distinguishable from the intact area of FRP-concrete system.

FRPP5 0.25" × 3" and 0.125" × 3" Defect

These response velocity spectrums were indistinguishable from that of the measurement over an intact area of the FRP-concrete system. The conclusion was that a 0.25" crack is too small to exhibit a response velocity within the 2 kHz - 22 kHz frequency band. Since the 0.5" crack has a resonant frequency at 10 kHz, to first order, the 0.25" crack would have a resonant frequency around 20 kHz and the 0.125" crack would have a resonant frequency of around 40 kHz. With an ultrasonic speaker as the excitation source, the crack might be able to be excited at a great enough amplitude to exhibit a clear vibration response.

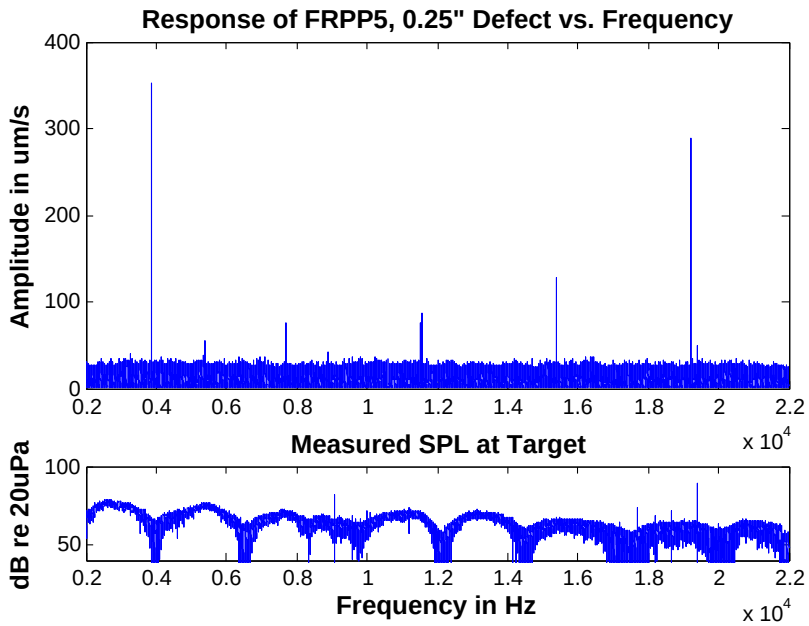

Figure 5-34: Frequency response of FRPP5 at center of 0.25" wide crack defect

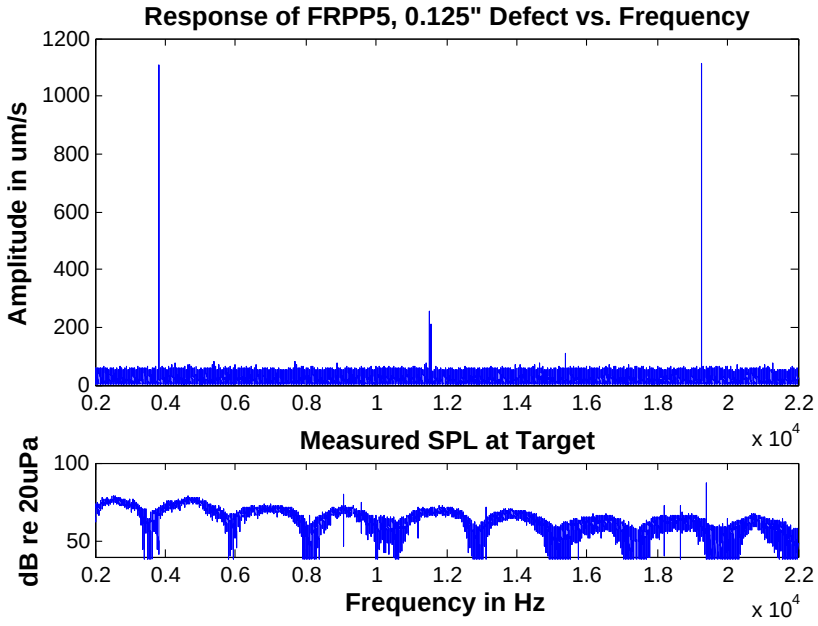

Figure 5-35: Frequency response of FRPP5 at center of 0.125" wide crack defect

5.2.10 Summary: Frequency Sweep Defect Measurements

The frequency responses of simple cubic and delamination type defects on concrete panels and cylinders, was quantified and compared to results obtained from finite element analysis, and the base resonant frequencies roughly matched. With the available frequency range of the acoustic excitation, of up to 22 kHz, the narrowest defect that could be detected was 0.25" wide in some cases. It is possible that with a more sensitive vibrometer and a higher frequency excitation, even narrower defects can be detected, as they exhibit smaller vibration amplitudes at higher resonant frequencies. An irregular delamination and angled crack were also measured. In the case of the angled crack, an interesting result was that identifiable resonant frequency peaks, signifying a defect was obtained from a measurement made over an area where the FRP-concrete system intact, but with a crack underneath the concrete at a shallow depth. This means that it may be possible to detect shallow internal cracks with the acoustic-laser vibrometry method in plain reinforced-concrete. These measurements characterized the frequency response of the defects in different locations, but to get a better sense of the actual vibration of the defect, an image needs to be constructed in some way.

5.3 Image Construction

In order to try and determine the modal behavior of the resonances, a grid of measurements were made over the defects to create an image of the surface response velocity spectrum of the defect. A frequency sweep of the acoustic excitation and a laser vibrometer measurement was made at each point on the grid to determine the frequency response at each point. The amplitudes at resonant peaks, with some tolerance in the frequency, were recorded to be plotted vs. their location on the grid to generate the following surface plots. As many possible coherent surface plots were made for each defect, however some other resonant frequencies may not have had large enough vibration amplitudes to stand out above the noise floor. They give an image of how the defect vibrates at the specified frequency and the location of

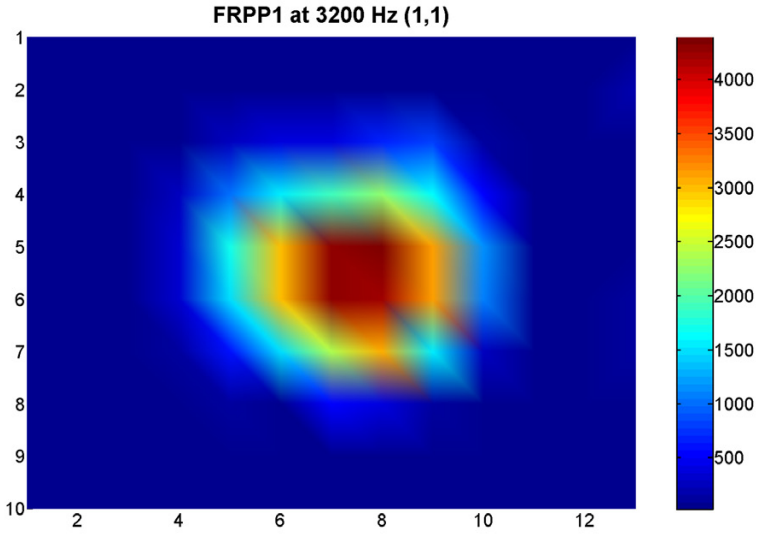

Figure 5-36: Surface plot of vibration amplitude for specimen FRPP1 at 3200 Hz, 1,1 mode

modal lines.

5.3.1 FRPP1

For the FRPP1 defect a measurement over a 2" × 2" grid, consisting of 13 × 10 measurements, enclosing the 1.5" × 1.5" defect was done. The area over the defect consisted of the central 7 × 6 grid of measurements. Surface plots of the vibration amplitude were made at 3200 Hz, 4050 Hz, and 6050 Hz. The 3200 Hz plot is the 1,1 mode, the 4050 Hz plot is the 2,1 mode, and the 6050 Hz plot is the 1,2 mode.

Figure 5-36 shows the surface plot of vibration amplitudes at the first resonant mode of the FRPP1 specimen defect, at 3200 Hz. The image shows a mode shape that we expect for the first resonant mode of what is effectively a clamped plate. There are no nodes and the velocity only goes to zero at the edges of the defect. The boundary of the defect and areas of intact FRP-concrete material are shown by the lack of vibration amplitude around the border.

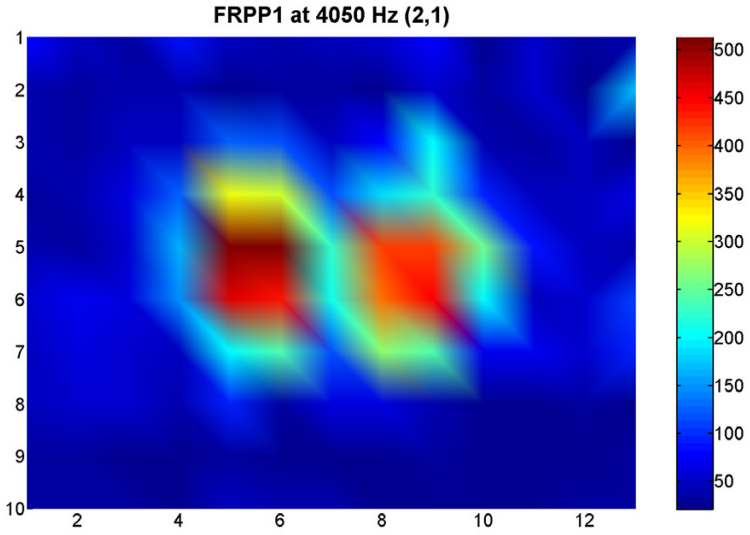

Figure 5-37: Surface plot of vibration amplitude for specimen FRPP1 at 4050 Hz, 2,1 mode

Figure 5-37 is a surface plot of the same defect, but at the second resonant mode of the defect at 4050 Hz. This is the mode shape we expected for the second resonant mode of the defect, as there is one vertical nodal line and presumably on either side, two portions of the plate that vibrate opposite to each other. The frequency of this mode, however was not approximately double that of the first which was expected from the basic theory of plate vibration. Recall that it was only accurate for isotropic materials, and that FRP is not an isotropic material. FRP is a directional material with greater tensile strength in the direction of the glass fibers, therefore the vibrational modes beyond the first have modal lines in the same direction of the fibers, because perpendicular to that direction, the material is less stiff. Therefore, the resonant frequency of the second mode is not double the frequency of the first.

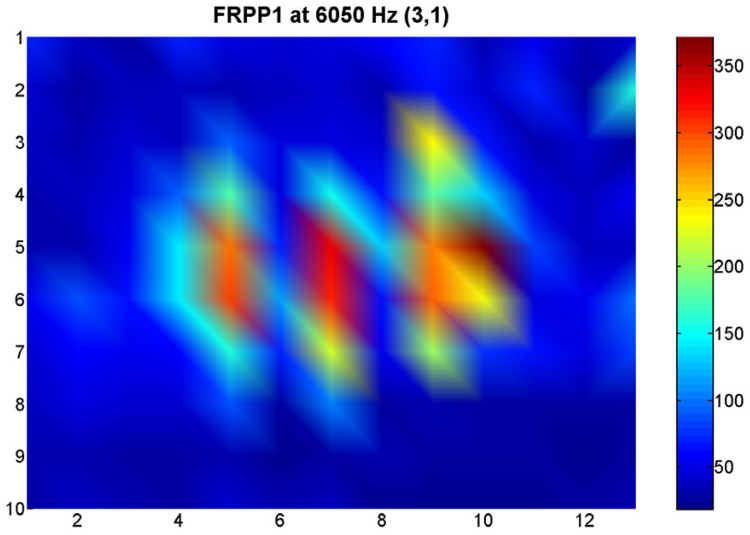

Figure 5-38: Surface plot of vibration amplitude for specimen FRPP1 at 6050 Hz, 3,1 mode

Figure 5-38 shows the third resonant mode of the defect at a frequency of 6050 Hz. The image shows two vertical nodal lines running in the same direction of the fibers of the FRP, and the resonant frequency was slightly less than double that of the first resonant mode.

5.3.2 FRPP2

For the FRPP2 specimen, a grid of 15 × 15 measurements covering a 3.5" × 3.5" area over the 3" × 3" defect were made. The area over the defect consisted of the central 13 × 13 grid of measurements. Surface plots of the vibration amplitude were made at 1380 Hz, 1490 Hz, 1580 Hz, 2050 Hz, 2750 Hz, 3260 Hz, 3580 Hz, and 3940 Hz. The plot at 1380 Hz is a 1,1 mode, 1490 Hz is a 2,1 mode, 1580 Hz is another 2,1 mode, 2050 Hz is a 3,1 mode, 2750 Hz is a 4,1 mode, 3260 Hz is a 1,3 mode, 3580 Hz is a 2,3 mode, and 3940 is a 3,3 mode.

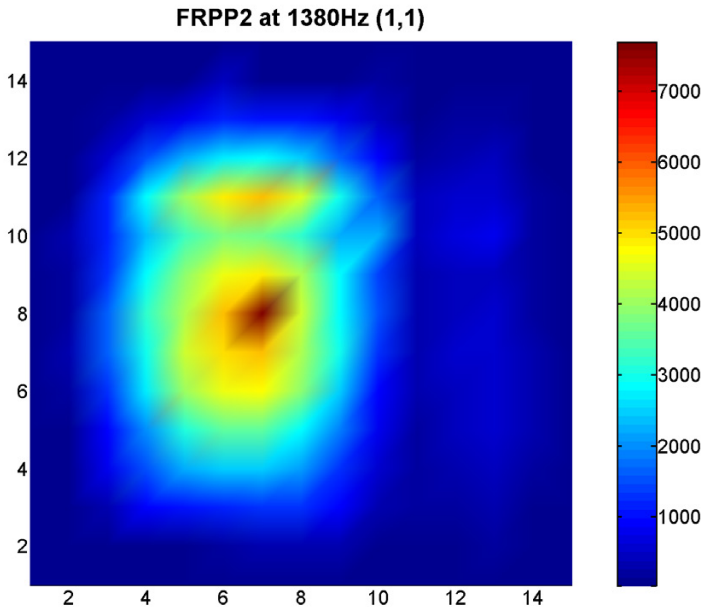

Figure 5-39: Surface plot of vibration amplitude for specimen FRPP2 at 1380 Hz, 1,1 mode

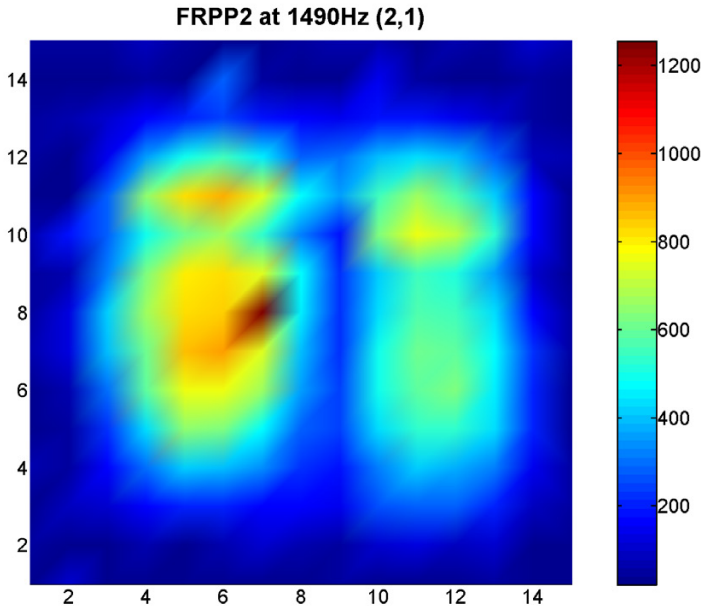

Figure 5-40: Surface plot of vibration amplitude for specimen FRPP2 at 1490 Hz, 2,1 mode

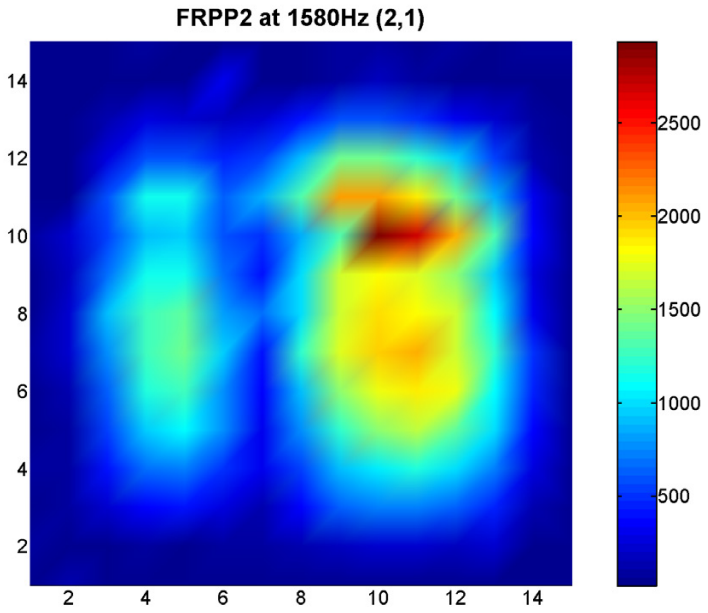

Figure 5-41: Surface plot of vibration amplitude for specimen FRPP2 at 1580 Hz, 2,1 mode

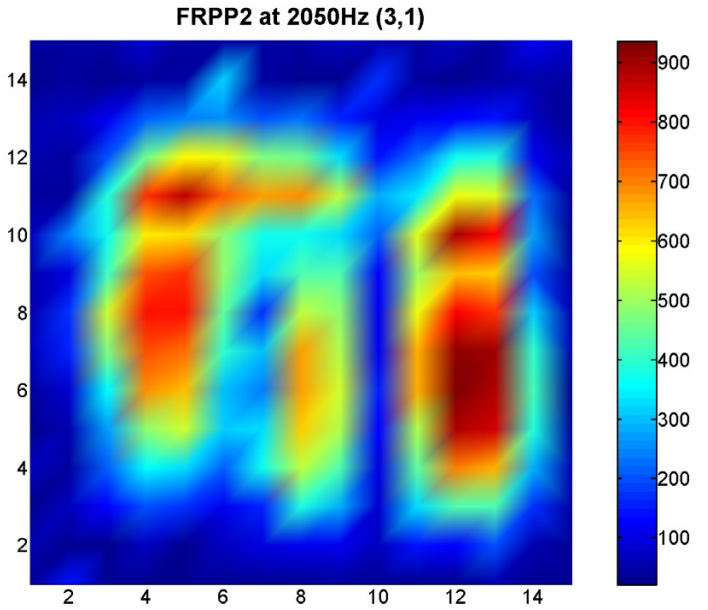

Figure 5-42: Surface plot of vibration amplitude for specimen FRPP2 at 2050 Hz, 3,1 mode

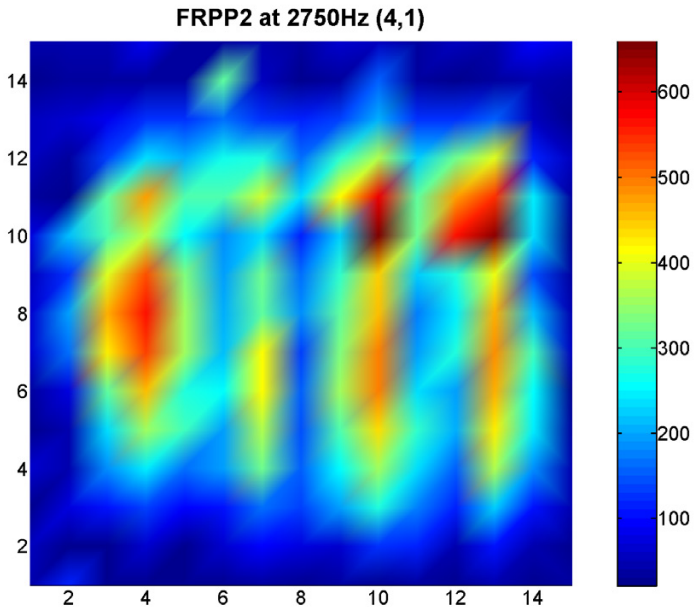

Figure 5-43: Surface plot of vibration amplitude for specimen FRPP2 at 2750 Hz, 4,1 mode

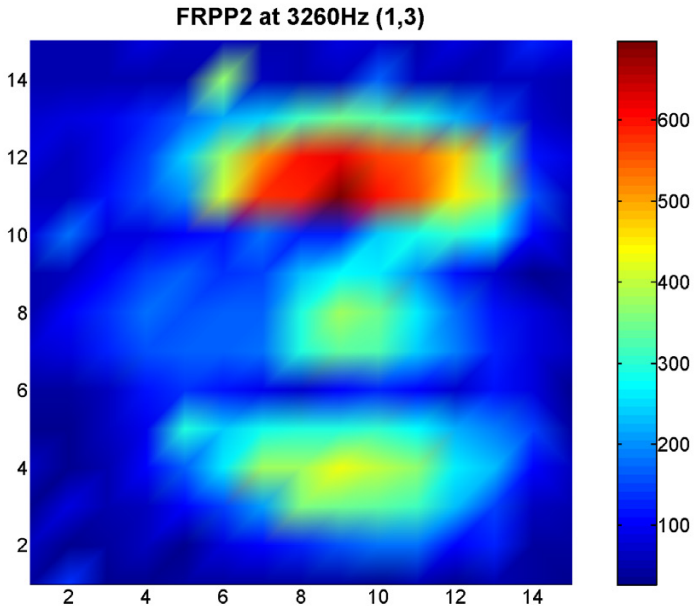

Figure 5-44: Surface plot of vibration amplitude for specimen FRPP2 at 3260 Hz, 1,3 mode

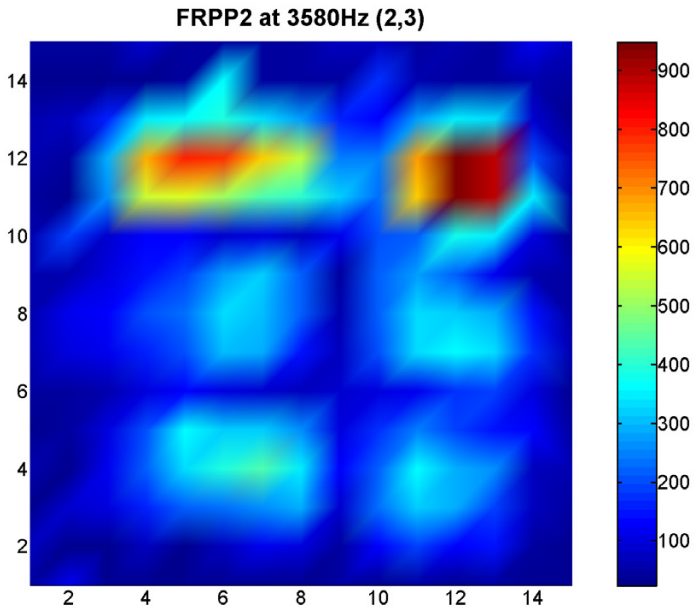

Figure 5-45: Surface plot of vibration amplitude for specimen FRPP2 at 3580 Hz, 2,3 mode

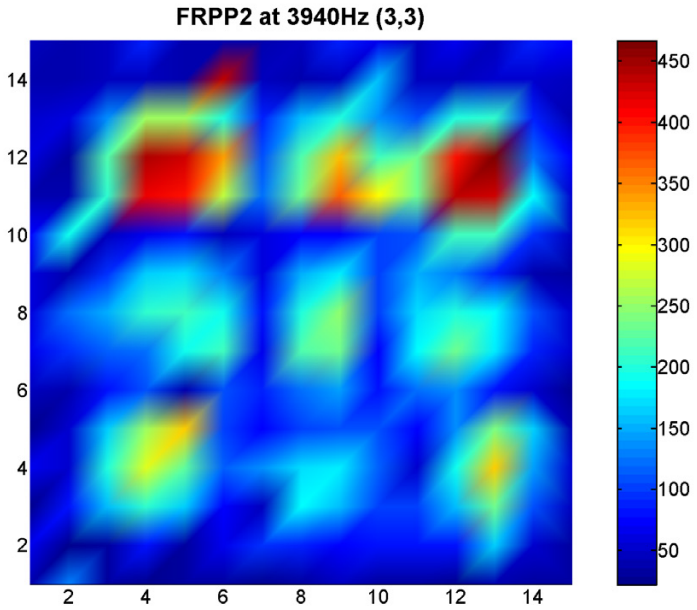

Figure 5-46: Surface plot of vibration amplitude for specimen FRPP2 at 3940 Hz, 3,3 mode

5.3.3 FRPC1

For the FRPC1 specimen, a grid of 9 × 9 measurements covering a 2" × 2" area over the 1.5" × 1.5" defect were made. The area over the defect consisted of most of the central 8 × 8 grid of measurements. Surface plots of the vibration amplitude were made at 4400 Hz, 6040 Hz, and 8860 Hz. The 4400 Hz plot shows the fundamental 1,1 mode, the 6040 Hz plot shows the 1,2 mode, and the 8860 Hz plot shows the 2,1 mode.

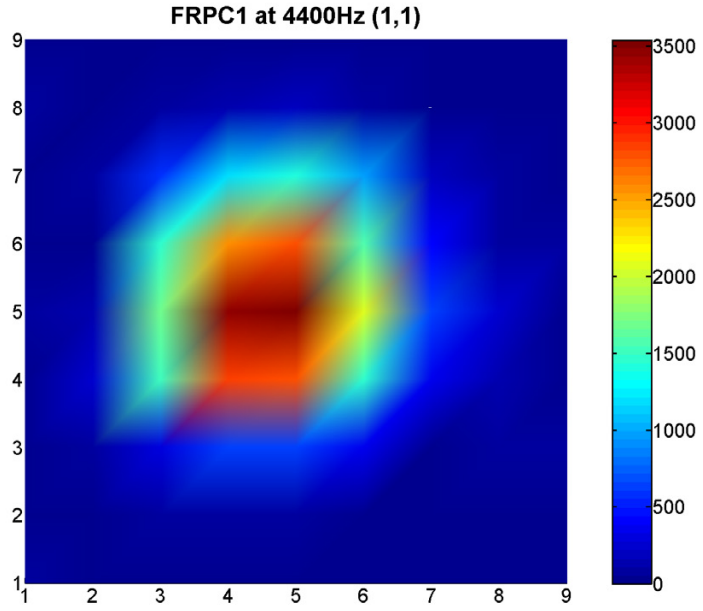

Figure 5-47: Surface plot of vibration amplitude for specimen FRPC1 at 4400 Hz, 1,1 mode

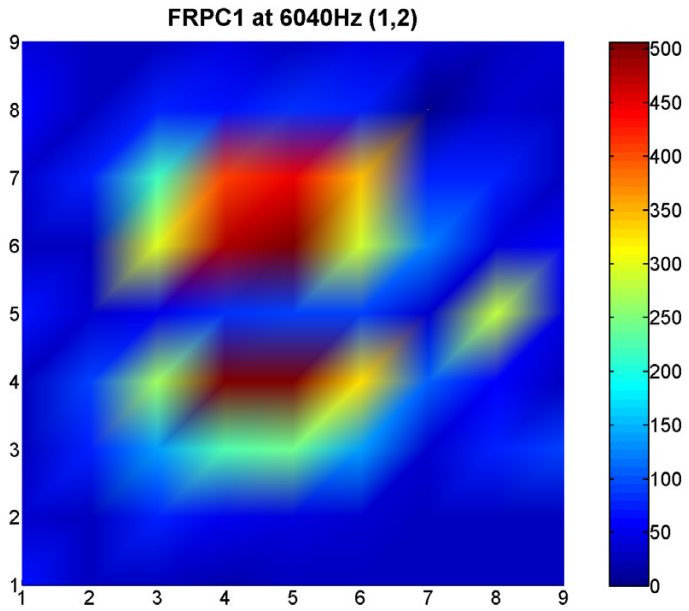

Figure 5-48: Surface plot of vibration amplitude for specimen FRPC1 at 6040 Hz, 1,2 mode

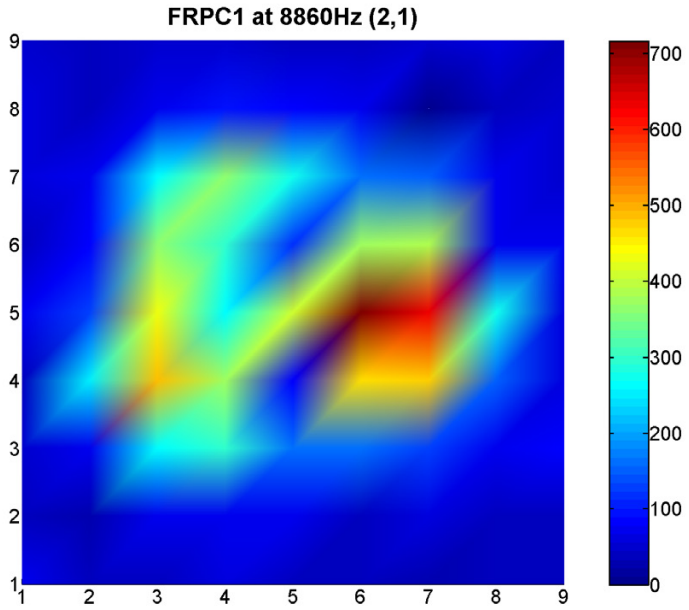

Figure 5-49: Surface plot of vibration amplitude for specimen FRPC1 at 8860 Hz, 2,1 mode

5.3.4 FRPC2

For the FRPC2 specimen, a grid of 9 × 9 measurements covering a 3.5" × 3.5" area over the 3" × 3" defect were made. The area over the defect consisted of the central 8 × 8 grid of measurements. Surface plots of the vibration amplitude were made at 2740 Hz and 3150 Hz. The plot at 2740 Hz shows the 2,1 vibrational mode, while the plot at 3150 Hz shows a 1,1 vibrational mode.

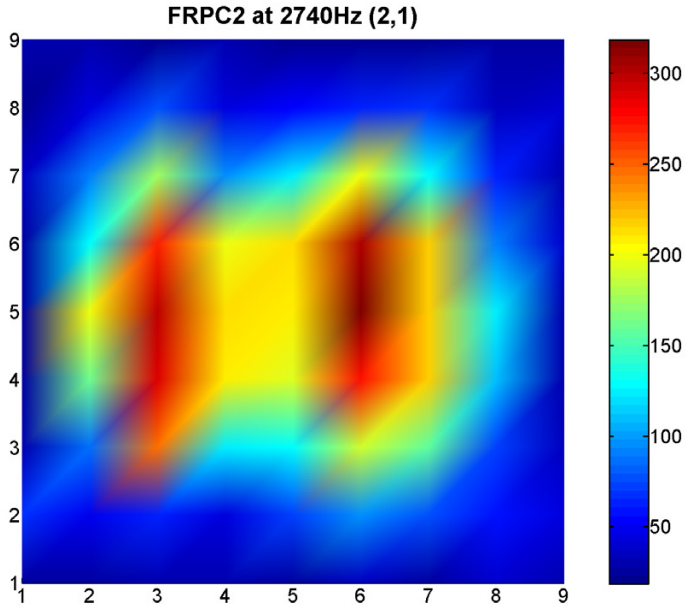

Figure 5-50: Surface plot of vibration amplitude for specimen FRPC2 at 2740 Hz, 2,1 mode

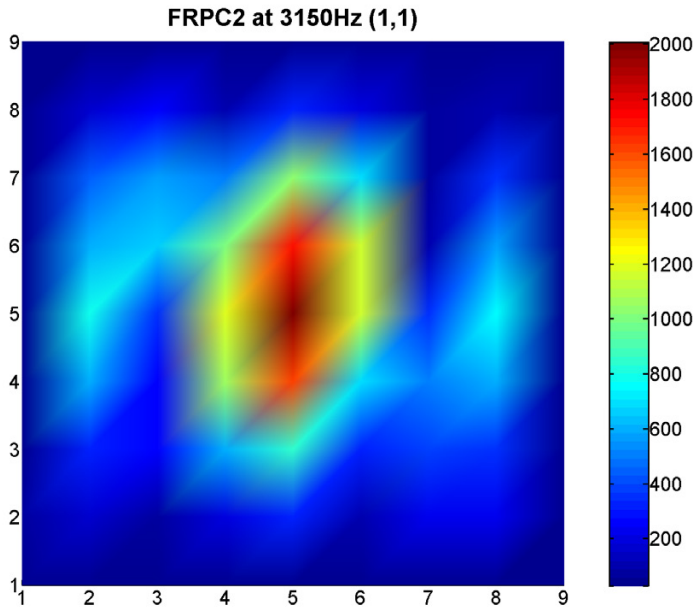

Figure 5-51: Surface plot of vibration amplitude for specimen FRPC2 at 3150 Hz, 1,1 mode

5.3.5 FRPC4

For the FRPC4 specimen, a grid of 5 × 6 measurements covering a 3" × 5" area over the 1.5" × 5" defect were made. Most of the central 3 × 5 measurements were over the delamination defect. Surface plots of the vibration amplitude were made at 6300 Hz, 8100 Hz, 9090 Hz, 10000 Hz, 11000 Hz, 12000 Hz, 13000 Hz, 14700 Hz, and 16700 Hz.

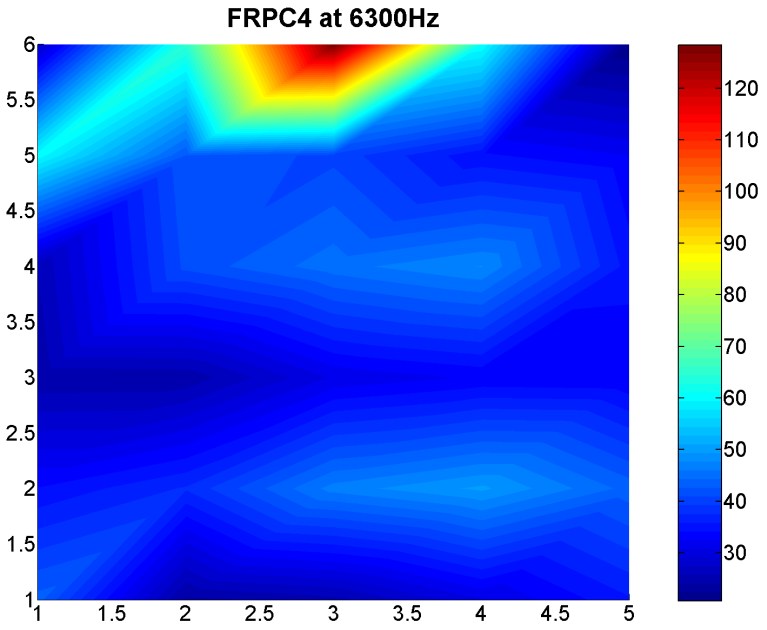

Figure 5-52: Surface plot of vibration amplitude for specimen FRPC4 at 6300 Hz

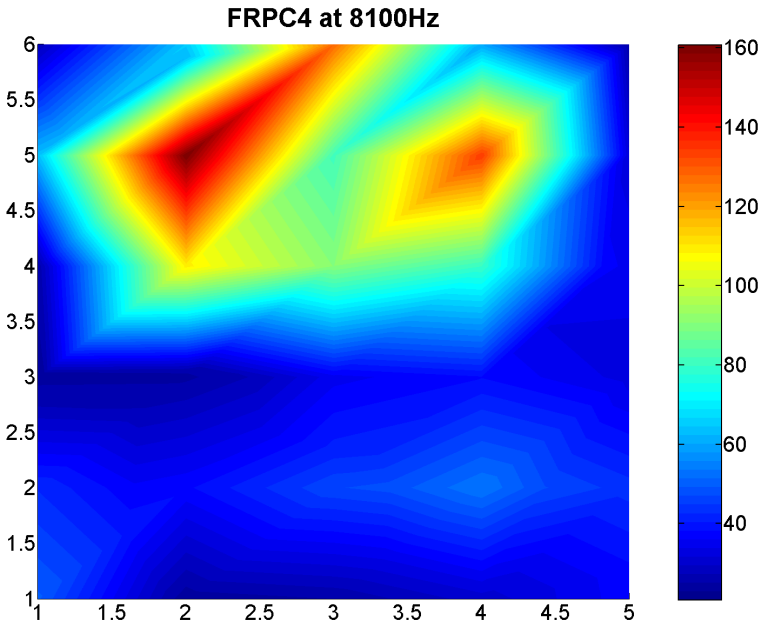

Figure 5-53: Surface plot of vibration amplitude for specimen FRPC4 at 8100 Hz

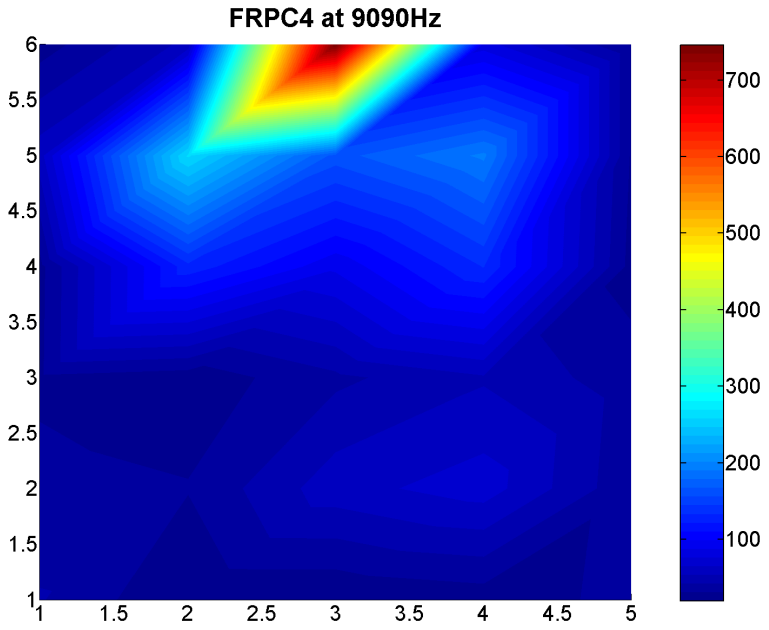

Figure 5-54: Surface plot of vibration amplitude for specimen FRPC4 at 9090 Hz

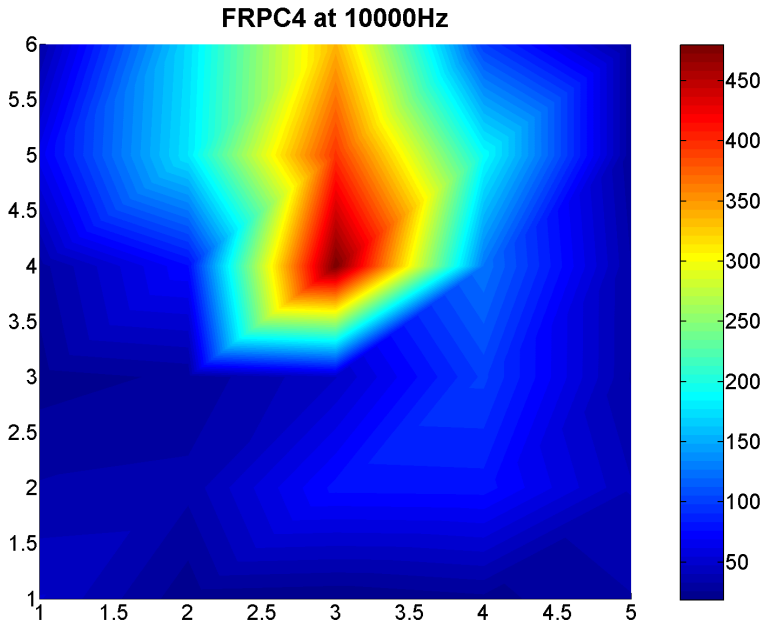

Figure 5-55: Surface plot of vibration amplitude for specimen FRPC4 at 10000 Hz

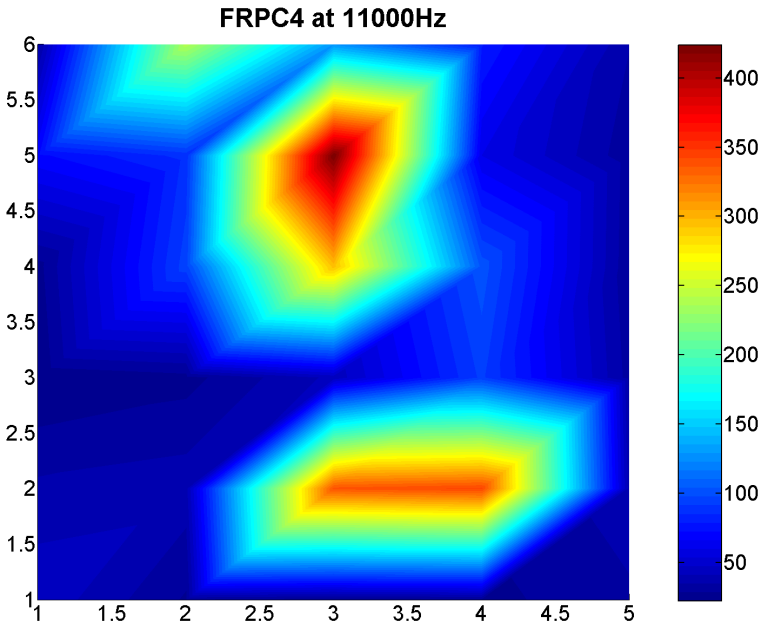

Figure 5-56: Surface plot of vibration amplitude for specimen FRPC4 at 11000 Hz

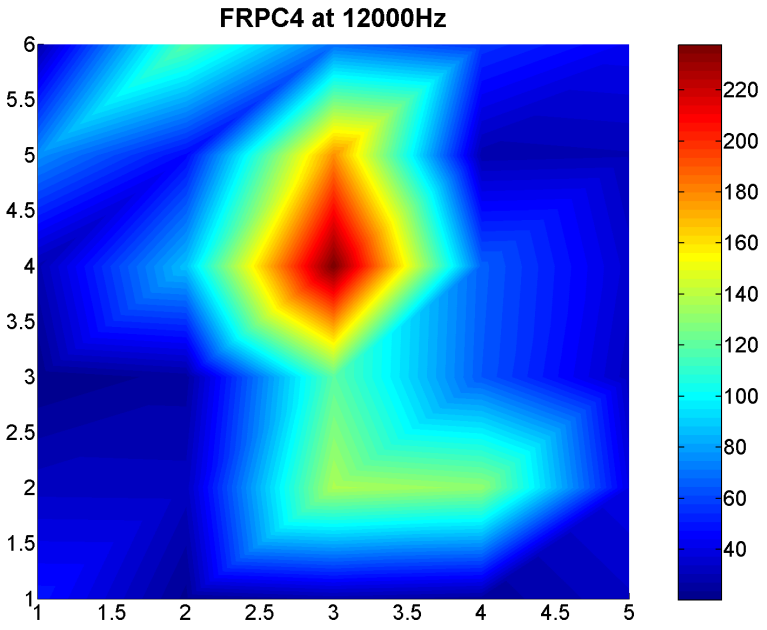

Figure 5-57: Surface plot of vibration amplitude for specimen FRPC4 at 12000 Hz

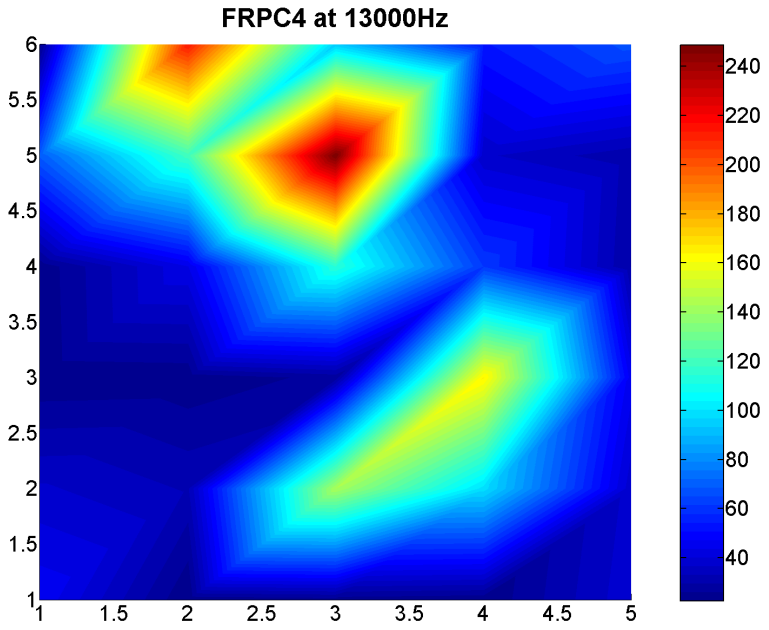

Figure 5-58: Surface plot of vibration amplitude for specimen FRPC4 at 13000 Hz

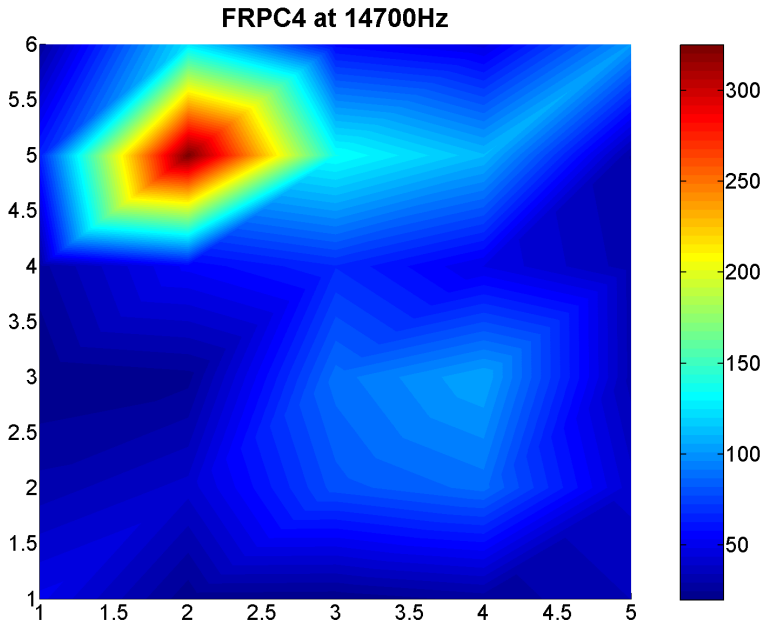

Figure 5-59: Surface plot of vibration amplitude for specimen FRPC4 at 14700 Hz

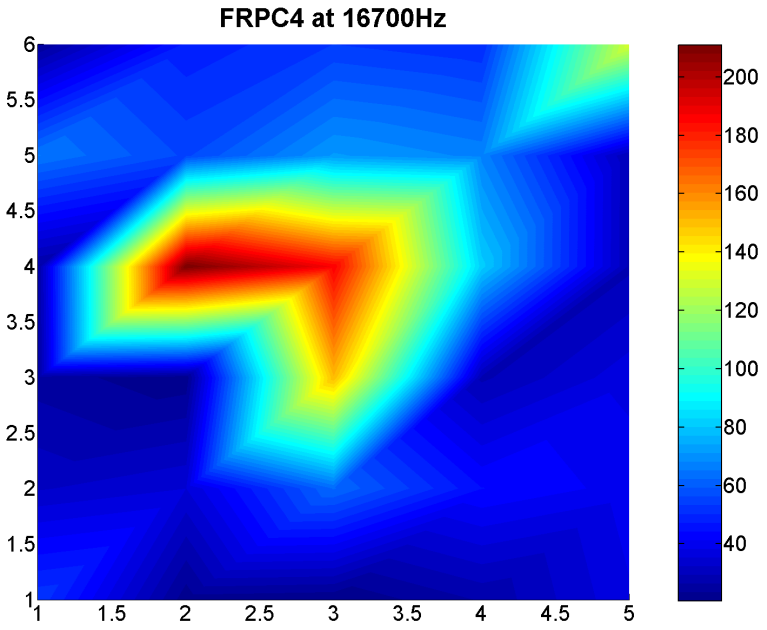

Figure 5-60: Surface plot of vibration amplitude for specimen FRPC4 at 16700 Hz

5.3.6 FRPP5 0.5" Defect

For the 0.5" width defect on the FRPP4 specimen, a line of 15 measurements covering a 3.5" length over the 0.5" $\times$ 3" defect were made. The center 13 measurements were over the defect. Plots of the vibration amplitude were made at 9390 Hz, 10010 Hz, 11340 Hz, 16300 Hz, and 20000 Hz.

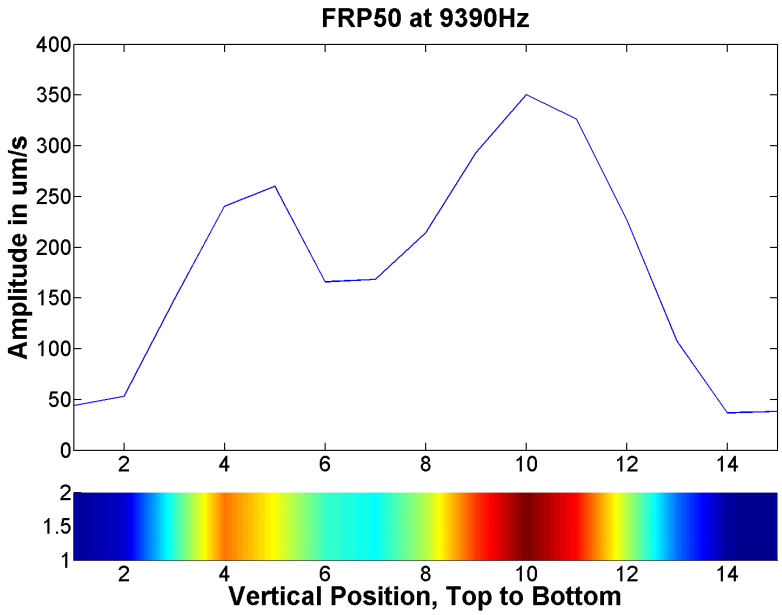

Figure 5-61: Plot of vibration amplitude for specimen FRPP5, 0.5" width defect at 9390 Hz

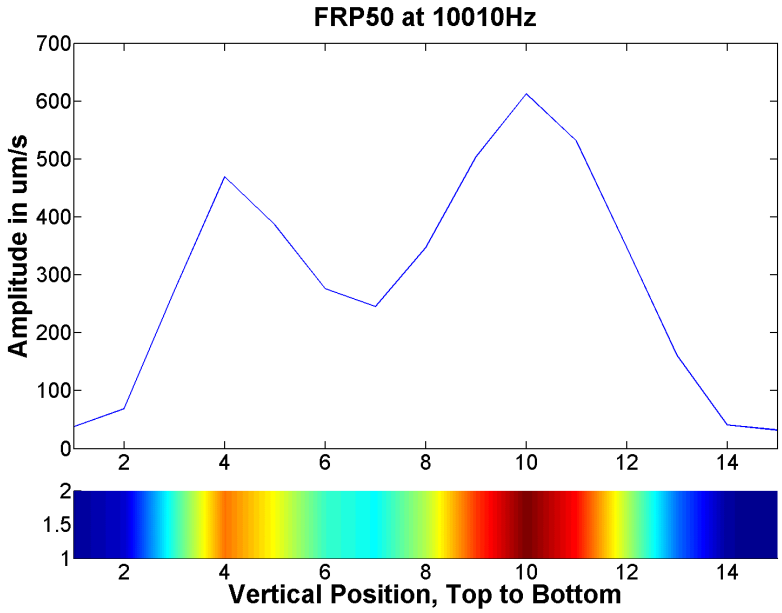

Figure 5-62: Plot of vibration amplitude for specimen FRPP5, 0.5" width defect at 10010 Hz

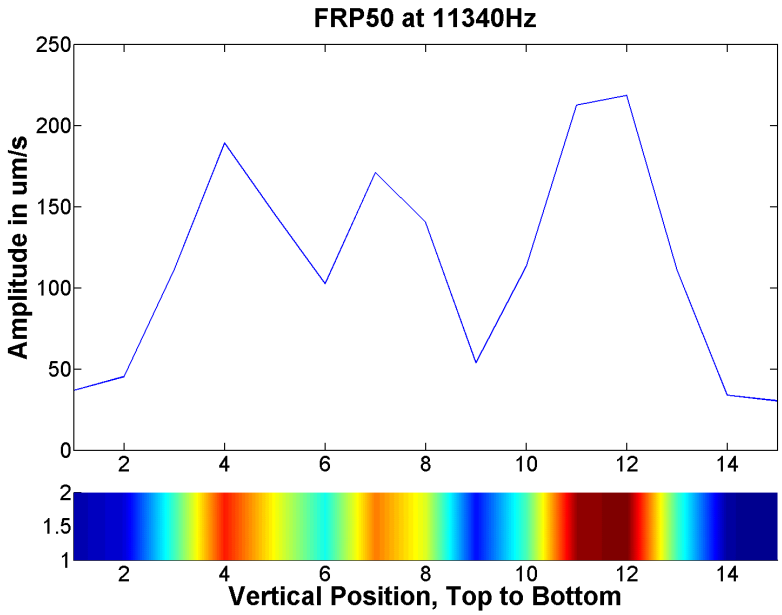

Figure 5-63: Plot of vibration amplitude for specimen FRPP5, 0.5" width defect at 11340 Hz

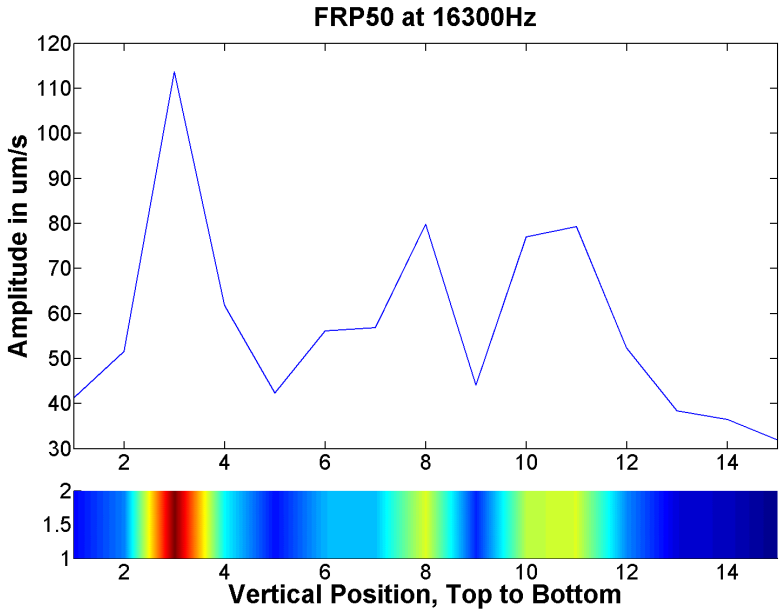

Figure 5-64: Plot of vibration amplitude for specimen FRPP5, 0.5" width defect at 16300 Hz

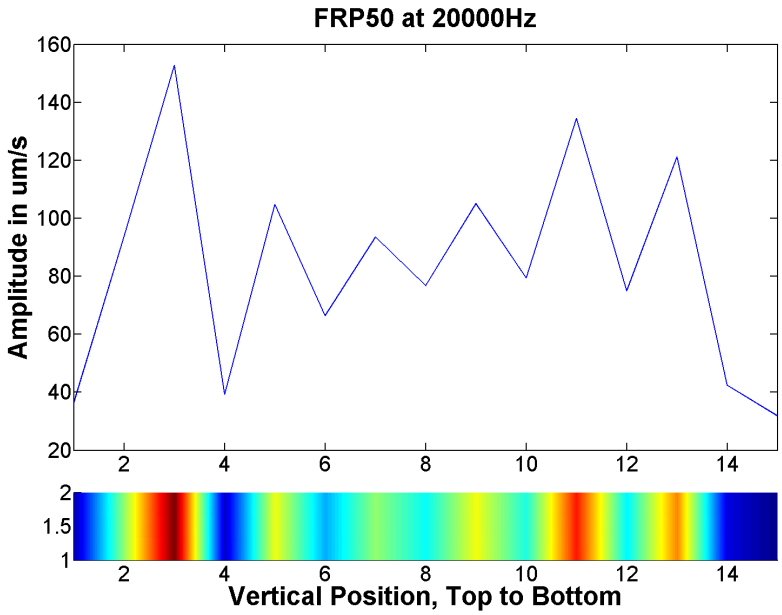

Figure 5-65: Plot of vibration amplitude for specimen FRPP5, 0.5" width defect at 20000 Hz

5.3.7 Summary: Image Construction

Images were constructed from a grid of measurements made over the general area surrounding and including the defect. At each point, a frequency response measurement was made, and by compiling the response velocities at a number of frequencies for all of the points on the grid, an image of the surface velocity can be made. When these frequencies coincide with resonant frequencies of the defect, relatively higher amplitudes will be shown in defective areas of the measurement relative to intact areas. This can be used to determine locations on a specimen that have defects. An operational methodology for a commercial system might be as follows. A system makes many frequency sweep measurements over an area and saves the responses. Then, an image is constructed and the vibration frequency is swept through the measurement range, and the operator looks for a "hot spot" of larger vibration amplitudes to find a defect. Since defects will exhibit resonant behavior at multiple frequencies, false positives can be minimized by looking for

areas that have greater amplitude at a number of different frequencies. In order to determine how to improve the detectability of the system, various parameters that influenced the measurement were studied.

Chapter 6

Parametric Studies

In order to better characterize the methodology, a series of parametric studies were conducted. The sound pressure level (SPL), laser signal level, angle of incidence, dwell time, and frequency sweep duration were varied to determine their effect on the noise floor, vibration amplitude, or the signal to noise ratio. These studies help determine ways of improving system performance by means of increasing the probability of detection or increasing the speed of measurement.

6.1 Sound Pressure Level

A series of measurements were made to determine the relationship between the incident SPL and the amplitude of vibration that was measured by the laser vibrometer. This determined a minimum SPL necessary for the detected vibration amplitude to be above a given noise floor level. The measurements were made at the center of the defects on each sample, with a constant frequency sine wave at the resonant frequency as determined in Chapter 5, the acoustic frequency dependence measurements. Measurements were taken at a number of different SPL and were fitted to an exponential curve. A plot showing these measurements and fitted functions for specimen FRPP1 is shown in Figure 6-1. Plots for the other specimen FRPP2, FRPC1, and FRPC2 are shown in Appendix A, Figures A-7, A-8, and A-9 respectively.

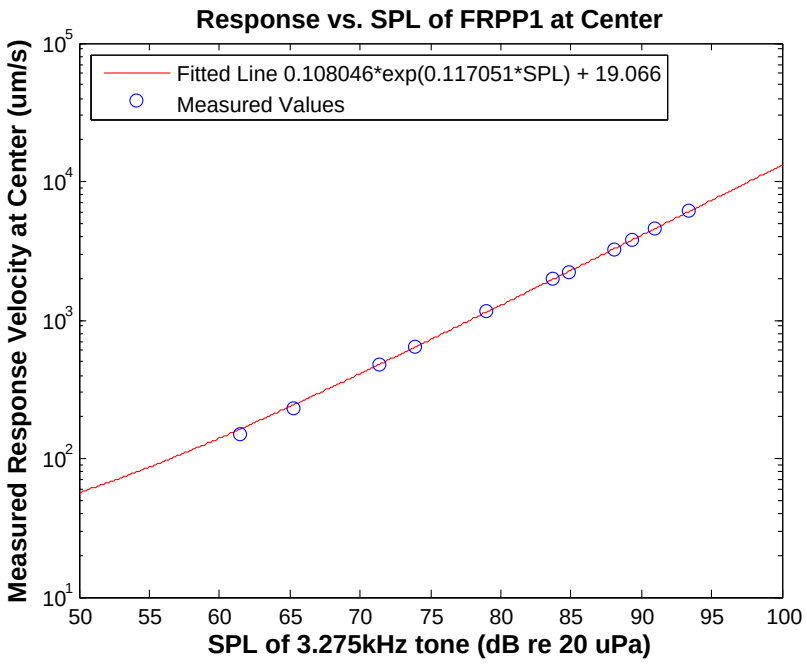

Figure 6-1: Vibration amplitude of specimen FRPP1 vs. sound pressure level and fitted curve

In general, defects on a flat panel had greater vibration amplitude for a given SPL than the defects on the curved cylinder. This was expected because the curvature adds stiffness and decreased the vibration amplitude. Similarly the smaller 1.5" $\times$ 1.5" defects had a relatively greater vibration amplitude than the larger 3" $\times$ 3" defects, but not by as much of a margin as the difference between the curved and the flat defects. For the two defects on concrete cylinders, a SPL of greater than 70dB at a resonant frequency caused the sample to respond at an amplitude of at least 100 $\frac{\mu m}{s}$, which is considerd to be detectable in the laboratory. Likewise, for the two defects on panels, a SPL of greater than 60dB is enough to ensure a vibration amplitude of the defect of about 100 $\frac{\mu m}{s}$. The caveat here is that these measurements were done in a best case scenario condition, where the laser vibrometer measured the center of the defect where vibration was greatest, and the frequency of the acoustic excitation was tuned to the primary resonant frequency of the defect. Despite being a best case scenario, this is valuable information that helps determine the resolution of the system.

6.2 Angle of Incidence

Angle of incidence is an important factor for the measurement system that greatly influences the measured response vibration amplitude. The laser vibrometer only measures movement collinear to the direction of the beam, and the amount of power the acoustic excitation imparts to the specimen is greatest at normal incidence. We expect a cosine dependence for the laser vibrometer measurement and the acoustic excitation. If a measurement is made where the specimen alone is rotated to change the angle of incidence, and the laser vibrometer and speaker position stay fixed, a cosine squared dependence from the multiplication of both cosine dependences is expected.

Measurements were made with the FRPP1 specimen at 4 different angles of incidence, 0°, 10°, 20°, and 45°. The surface of the FRP was slightly rippled, with surface roughness greater than the laser spot size, making measurements at any greater angle of incidence difficult. The plot of the measurements is shown in Figure 6-2.

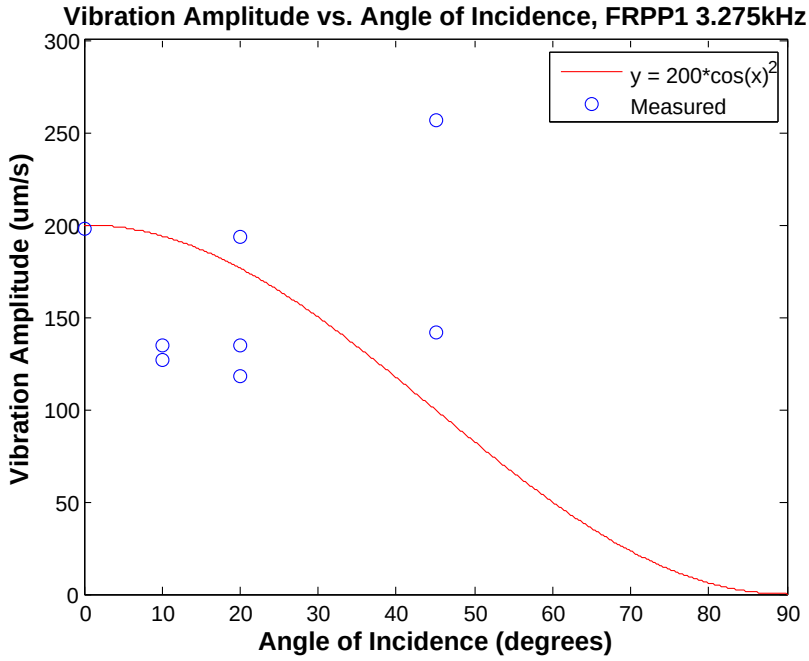

Figure 6-2: Vibration amplitude vs. angle of incidence for FRPP1 specimen

This set of measurements was highly inconsistent with a predicted cosine squared dependence, and highly dependent on fine positioning of the laser beam on the specimen. The rippling of the FRP surface caused the amount of movement measured by the laser vibrometer, to be different than what would be seen with a flat surface, depending on where on the surface it hit. With a rippled surface, where the laser spot size was smaller than the approximate surface roughness, the various slopes of the surface distorted the amount of movement in the direction of the laser beam. The problem that the rippled surface caused is shown in the Figure 6-3.

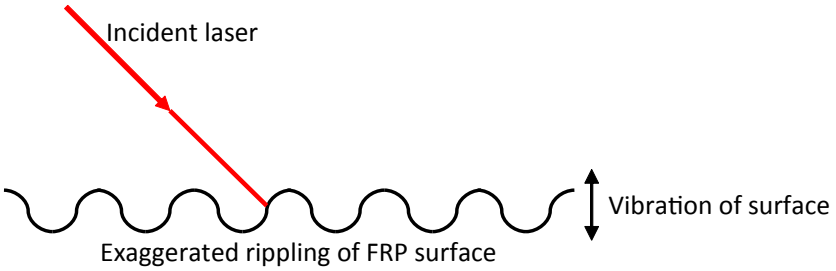

Figure 6-3: Diagram of rippled FRPP1 surface measurement

In order to make an accurate measurement of the effect of angle of incidence, a different specimen was measured, which was a flat prefabricated FRP plate bonded with epoxy to a steel plate [32, 33]. The flatness of the FRP surface allowed measurement of the vibrational amplitude at angles of incidence, 0°, 15°, 30°, 45°, 60°, and 75°. Figure 6-4 shows the plot of the vibration amplitude measurements vs. the angle of incidence with an approximate cosine squared line superimposed over the data. This data validated the cosine squared dependence for the acoustic-laser vibrometry system, given a surface that is flat. Following the cosine squared dependence, 18.3° off of normal incidence would be allowed, before the measured vibration amplitude to decreased to 90% of the maximum vibration amplitude.

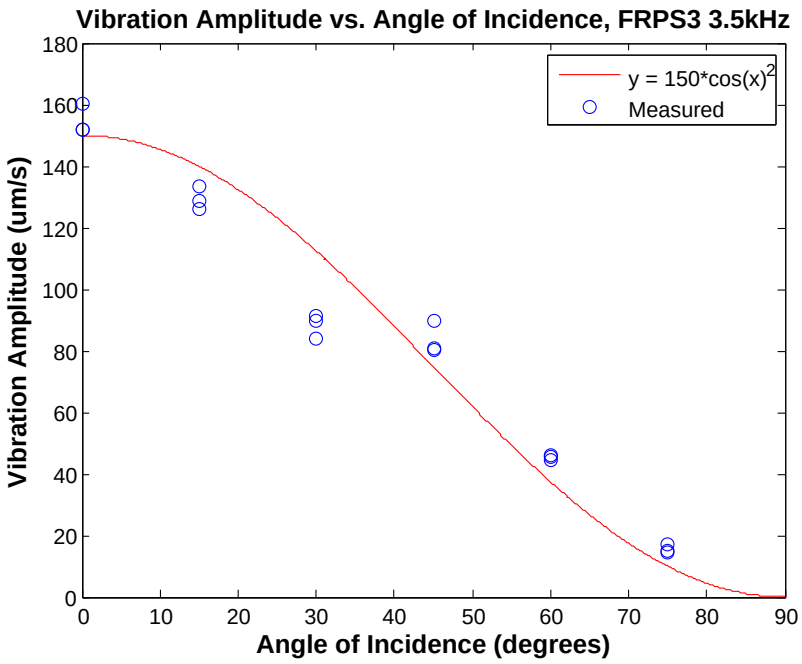

Figure 6-4: Vibration amplitude vs. angle of incidence for FRPS3 specimen

6.3 Laser Signal Level

The laser signal level is an important parameter that determines the noise floor of the laser vibrometer system. When less power is reflected back from the specimen, either because of poor surface quality, or increase in distance that reduces the amount of light captured by the laser vibrometer lens, the noise floor increases. In most of the measurements for the experiment, to ensure ideal conditions, retroreflective tape was used on the specimen, which reflects almost all of the incident laser power back to the laser vibrometer lens.

In order to systematically investigate the effect of less received laser power on the noise floor, neutral density filters were placed in front of the lens to reduce the amount of laser power both transmitted and received, with the most restrictive being an ND64 filter, which results in 1/128th or 0.78125% of the normal amount of power being reflected back to the laser vibrometer. Measurements were made with different amounts of filters to record the noise floor of the measurement and plotted in Figure 6-5.

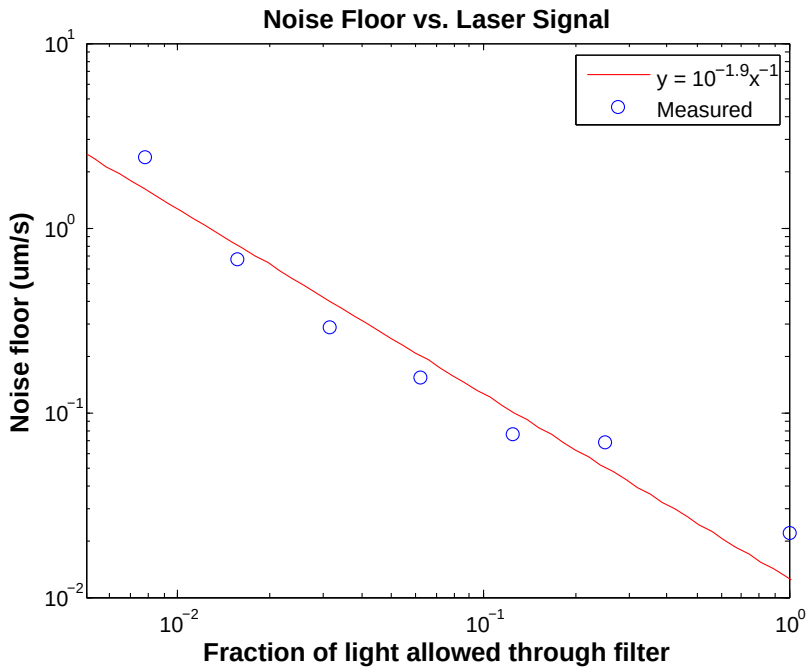

Figure 6-5: Noise floor vs. fraction of light allowed through back into the laser vibrometer

For a factor of 10 reduction in the fraction of light allowed to return to the laser vibrometer, the noise floor increased by a factor of 10. Since the amount of light reflected back into the laser vibrometer off of an ideal diffuse or Lambertian surface follows an inverse square law, a factor of 10 reduction in the fraction of light would correspond to a square root of 10 (3.16) increase in distance from the specimen without the use of retroreflective tape.

6.4 Dwell Time

Dwell time is an important parameter because of the ability to improve the signal to noise ratio (SNR) with longer measurements. Two different acoustic excitations to study the effect of dwell time on the measurement were used, a single frequency sine wave and a gaussian white noise waveform. Since the data was fast Fourier transformed (FFT), they excited the defect differently and changed how the vibration signal peak integrated with time. A coherent signal stays the same amplitude as the

FFT length increases, while an incoherent or signal with phase jumps will decay. As the dwell time increases, the random noise floor should decrease because the incoherent noise floor is being divided between a larger amount of bins because of the increase in FFT length. A doubling of the dwell time should result in a noise floor of half the amplitude. For the sake of brevity, plots for the measurement with the FRPP1 specimen are shown. Figure 6-6 shows the measurements conduced with a sine wave single tone acoustic excitation while Figure 6-7 shows the measurements conducted with a broadband white noise acoustic excitation. Measurements of the other specimens are given in Appendix A, Section A.2.2 and show similar results.

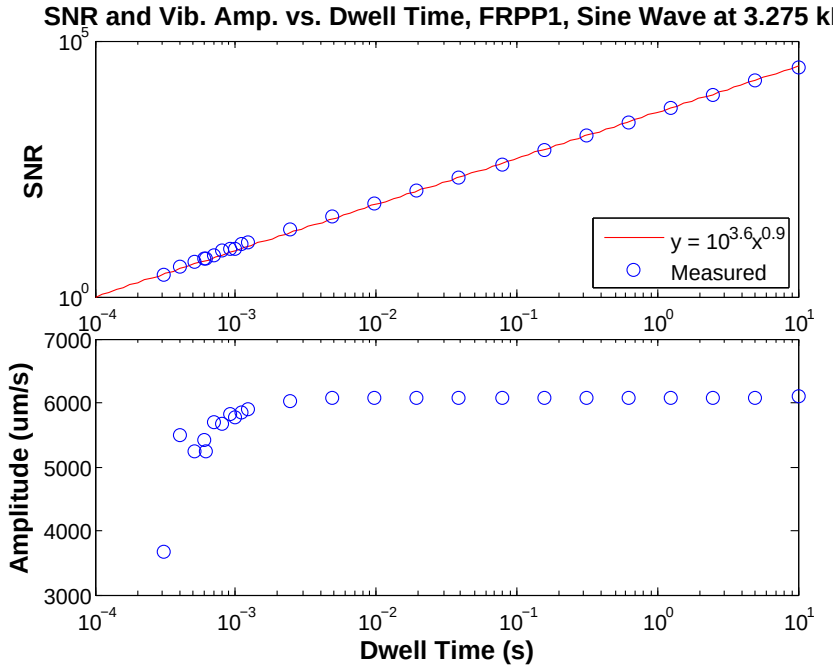

Figure 6-6: SNR and vibration amplitude as a function of dwell time for a sine wave excitation for FRPP1

In the case of both measurements, for the plots of the raw amplitude at the first resonant mode, the amplitudes experienced a sharp increase at a dwell time of 0.5 milliseconds. The reason for this was that the frequency of the resonant mode at 3.275 kHz corresponds to a period of 0.305 milliseconds, meaning that the FFT needed at least one full cycle of the vibration to resolve the signal and the corresponding amplitude. In the case of the single tone excitation, the vibration amplitude held

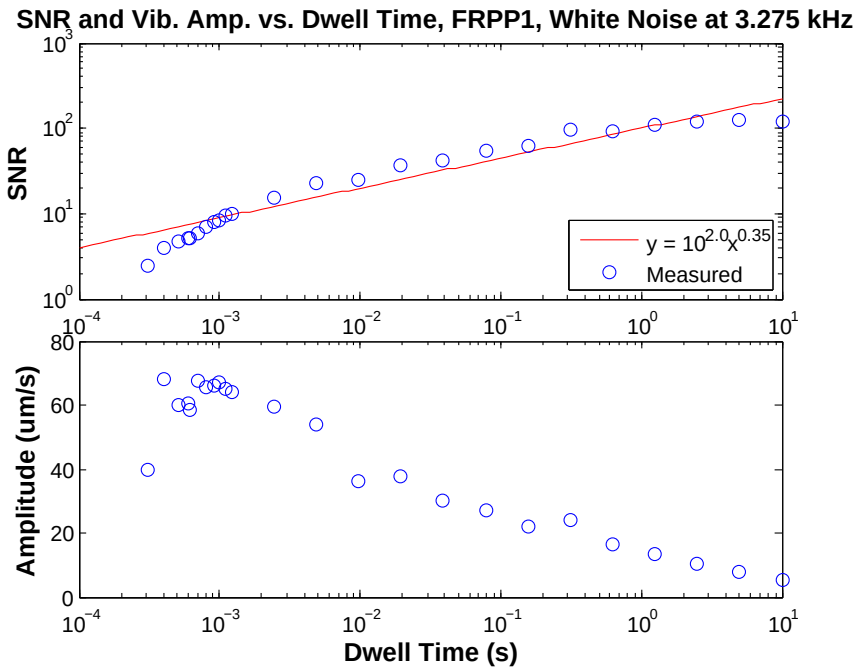

Figure 6-7: SNR and vibration amplitude as a function of dwell time for a white noise excitation for FRPP1

steady right around 6000 $\frac{\mu m}{s}$ for a wide range of dwell time, from 1 millisecond up to 10 seconds. The vibration amplitude in the white noise excitation measurement however, had a general declining trend from 1 millisecond to 10 seconds. This was because the white noise excitation, being random, did not induce the defect to vibrate regularly. As the dwell time increased, the signal from the defect was being integrated incoherently, so the vibration amplitude decreased.

As dwell time increased, SNR improved, however at different rates depending on the type of acoustic excitation. For the case of the constant sine wave excitation, when the dwell time increased by a factor of 10^4 from 1 millisecond to 10 seconds, and the SNR improved by the same factor. With the white noise excitation, when the dwell time increased from 1 millisecond, to 0.1 seconds, by a factor of 100, the SNR improved by a factor only 10, because the amplitude declines as well.

6.5 Frequency Sweep Duration Study

Analogous to the dwell time study, the time duration of the frequency sweep and the measurement can be varied to determine the effect on the amplitude and noise floor. The measurements were made on the FRPP1 specimen with a 0 - 20 kHz frequency sweep with durations of 0.1 seconds, 1 second, 10 seconds, and 60 seconds. SPL was held constant between these measurements and they were made on the same day with no changes in the experimental setup. The associated frequency response plots are shown in Appendix A, Figures A-16, A-17, A-18, and A-19.

Sweep Length (s)	**Frequency (Hz)**	**Average SPL (dB)**	**Amplitude ($\frac{\mu m}{s}$)**	**Noise Floor ($\frac{\mu m}{s}$)**	**SNR**
0.1	3247.8	80.3481	5068.0	74.0646	68.4268
1	3245.7	80.4217	4909.4	74.6392	65.7751
10	3246.6	80.4584	4972.1	73.1881	67.9359
60	3247.0	80.2238	5097.8	73.5018	69.3561

Table 6.1: Results from frequency sweep duration study

Table 6.1, summarizes the results. The amplitude, frequency, and noise floor, and as a result the SNR, stays somewhat constant at these frequency sweep durations. Looking at the previous analysis, the SNR of approximately 67 for all the measurements corresponded to a constant tone of only approximately 0.01 seconds in the case of a single frequency sine wave excitation. The FFT was just taken over the whole length of the measurement, not just near the time that the speaker is near the resonant frequency, which is why the SNR was not as good. Since the SNR did not improve with increasing frequency sweep length, this suggests that a more complicated processing method for frequency sweep measurements would be optimal for extracting the best SNR out of the measurement, with multiple FFTs taken over smaller windows over the length of the measurement. The amplitude of the resonant peak does not vary with frequency sweep duration which verifies that we have chosen the correct normalization constant of the square root of the bandwidth times the sweep duration.

6.6 Summary: Parametric Studies

Sound pressure level, angle of incidence, laser signal level, dwell time, and frequency sweep duration were studied to determine their effects on the measurement. Sound pressure level and angle of incidence affect the amplitude of the vibration measured by the laser vibrometer, with angle of incidence not having much effect within 18.3° of normal incidence. Laser signal level and dwell time in the case of a sine wave coherent excitation affect the noise floor. Dwell time with a white noise excitation affects both the noise floor and amplitude of the vibration. Frequency sweep duration was found not to have an effect on either the noise floor or the amplitude of the vibration. In summary, higher SPL, normal angle of incidence, more return laser power, and longer dwell time will improve detectability of defects.

Chapter 7

Receiver Operating Characteristic Curve Analysis

7.1 ROC Curves

In order to analyze the performance of the acoustic-laser vibrometry method, the receiver operating characteristic (ROC) curve was generated. They are a simple way to visualize the measures of binary detector performance, true positive and false positive rates as a function of some detection level parameter [52]. A detection vibration level was chosen, above which the measurement was classified as a positive detection of a defect, and below it was classified as a negative detection, or intact material. Since it is known which measurements were actually made on the defect or competent material, the true positive rate and false positive rate can be determined. A perfect detector has a positive rate of 1 or 100% corresponding to all defect measurements being detected as positive, and a false positive rate of 0 or 0% corresponding to no intact measurements being registered as defective. The measurements that were used to generate the ROC curve are shown in Figure 7-1. Measurements made on a defect are signified by a red circle, while measurements made on intact FRP-concrete system are signified by a green cross. The results of the classification into positive or negative detections are shown as a ROC curve in Figure 7-2, and the true and false positive rates as a function of the detection

vibration level is shown in Figure 7-3. Since the measurements are made where the defect represents a significant portion of the area being measured, the resulting ROC curve may not be truly representative of a real world measurement where the number of measurements of a defective area would be much smaller than the number of intact measurements.

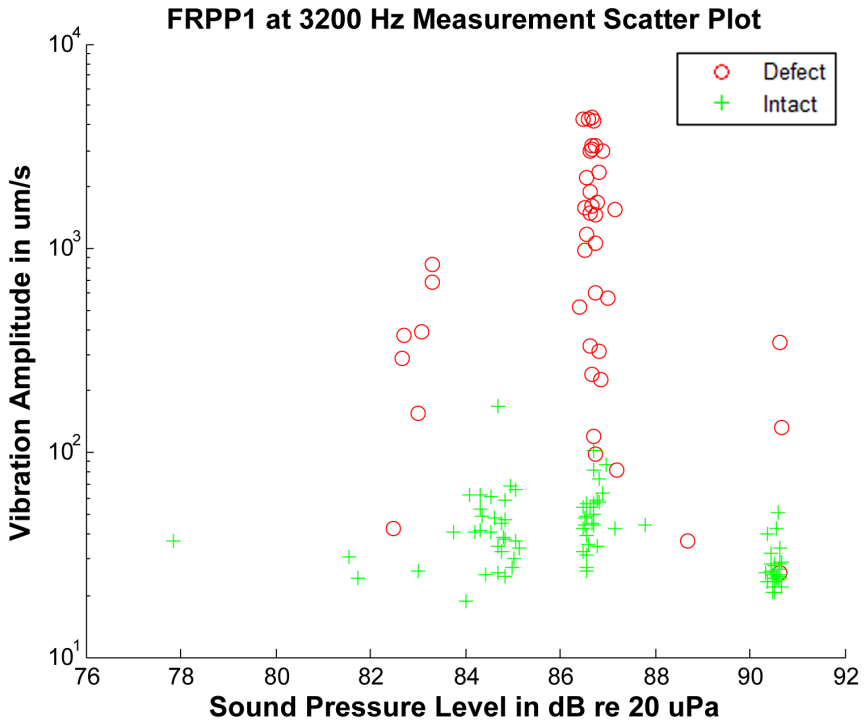

Figure 7-1: Scatter plot data from FRPP1 grid measurement at 3200 Hz

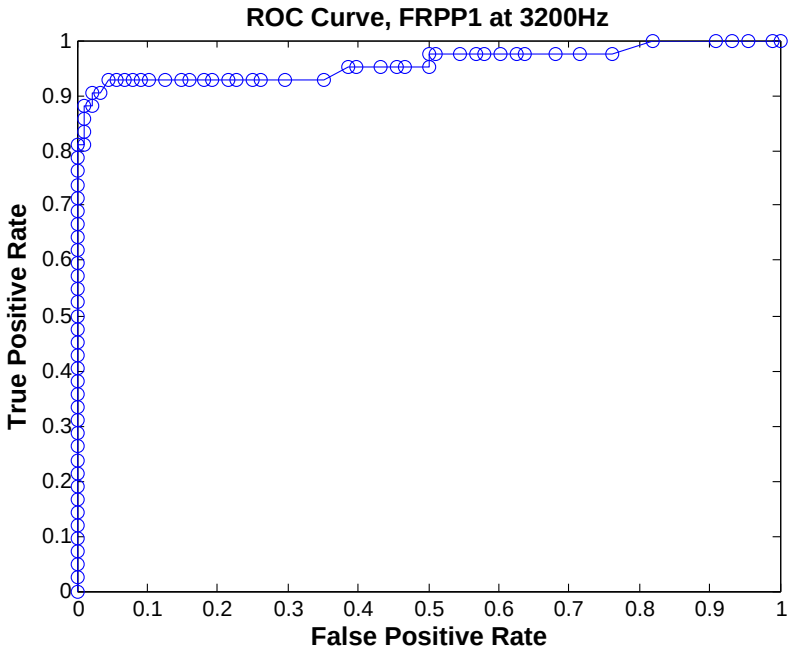

Figure 7-2: ROC curve for FRPP1 at 3200 Hz

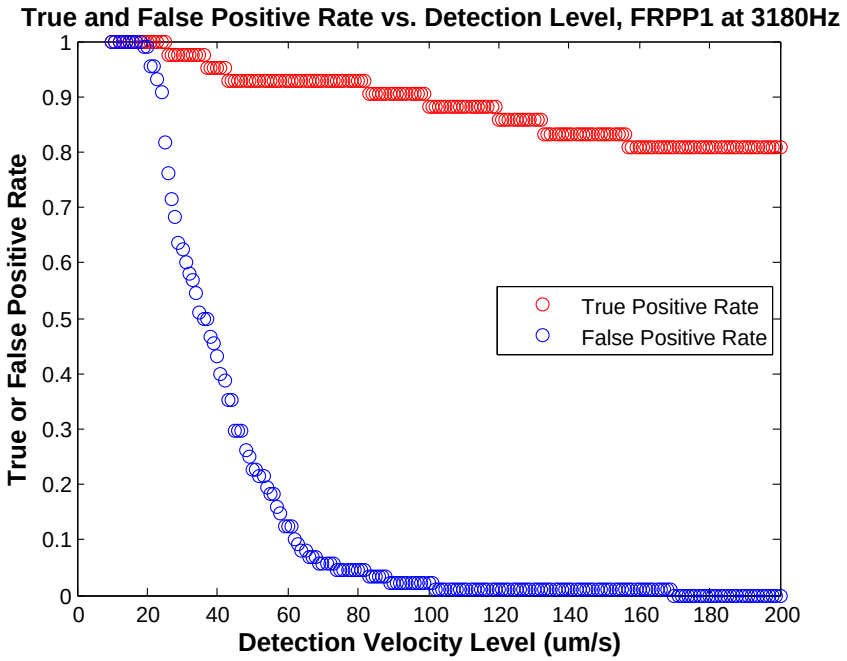

Figure 7-3: Plot of true and false positive rate vs. detection velocity level for FRPP1 at 3200 Hz

This ROC curve showed that making a series of frequency sweep measurements on the FRPP1 specimen, a 92.9% positive detection rate with a false positive rate of only 4.5% can be achieved. A higher positive detection rate of 95.2% is possible, however the false positive rate is increased to 38.6%. The proportionally larger number of measurements done near the edges of the defect where the vibration amplitude is close to that of intact material could explain this large increase in false positive rate without much improvement in positive detection rate. In the case of a real world measurement where the number of measurements over a defect is low relative to the number of mesurements over intact material, measurements are more likely to be made near the center of a defect rather than the boundary, so the positive detection rate may improve. Also, it is assumed that there will be a relatively low area of defects relative to intact material, therefore a low false positive rate is more important than a marginal improvement in positive detection rate. Therefore, the more useful detection criteria is one that results in the low false positive rate of 4.5%, where positive detection rate is maximized without any significant increases in false positive rate. This is a preliminary determination of the probability of detection of the laboratory system under ideal conditions. The detection velocity level that resulted in these detection rates was 74 μm/s. Since the maximum vibration velocity of the defect is 4380 μm/s, this gave a very good SNR of 59.2 or 17.7 dB.

The ROC curves for the FRPP2, FRPC1, and FRPC2 specimens using the data set collected in the image construction study are shown in Figures 7-4, 7-5, and 7-6 respectively. The associated measurement scatter plots, relationships between the true and false positive rates, and the detection velocity level are shown in Appendix A, Section A.3. From a series of frequency sweep measurements of the FRPP2 specimen at the fundamental resonant frequency of 1380 Hz, a 90.5% positive detection rate was achieved with a false positive rate of 5.4%, as shown in Figure 7-4. Frequency sweep measurements of the FRPC1 specimen at the fundamental resonant frequency of 4400 Hz yielded an 85.7% positive detection rate with a false positive rate of 4.5%, as shown in Figure 7-5. Frequency sweep measurements of the FRPC2 specimen at the fundamental resonant frequency of 3150 Hz yielded a 98.0% positive detection

rate with a false positive rate of 2.3%, as shown in Figure 7-6.

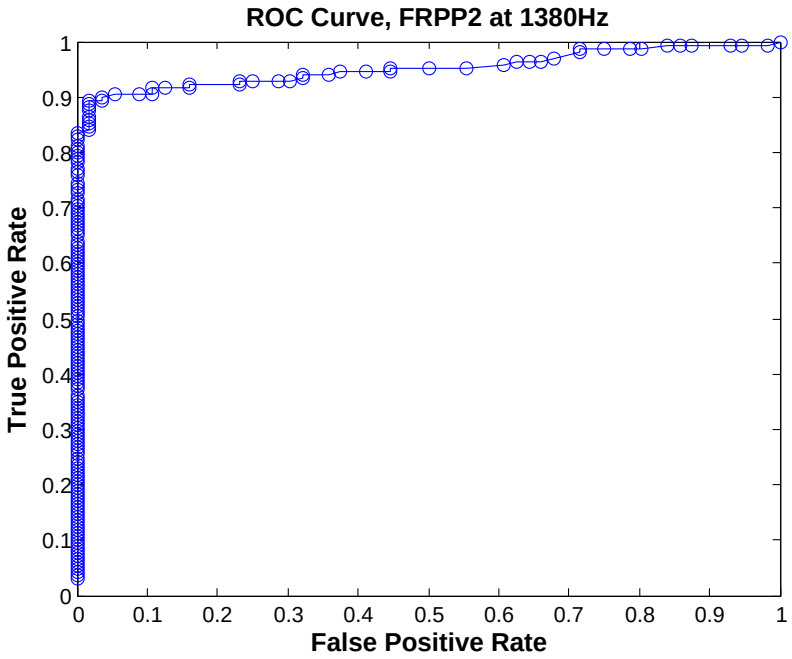

Figure 7-4: ROC curve for FRPP2 at 1380 Hz

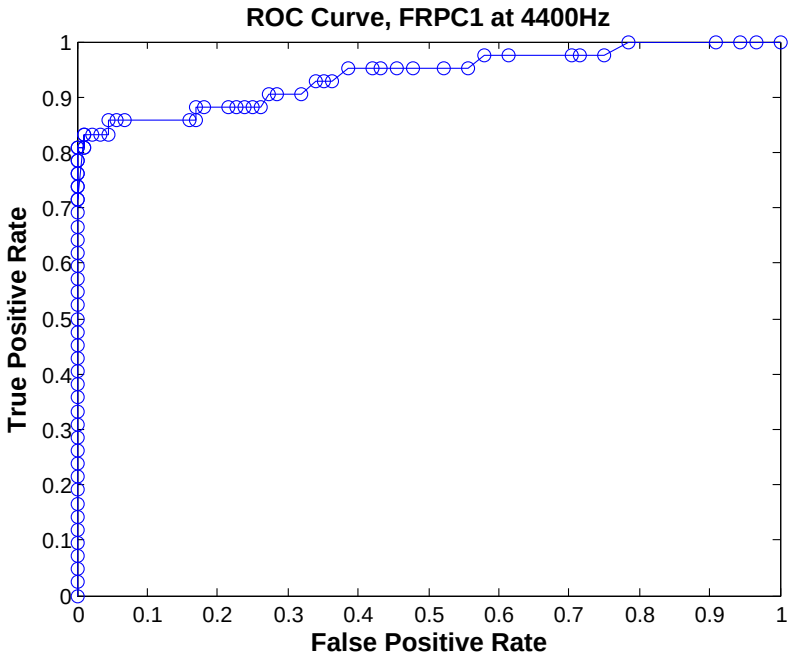

Figure 7-5: ROC curve for FRPC1 at 4400 Hz

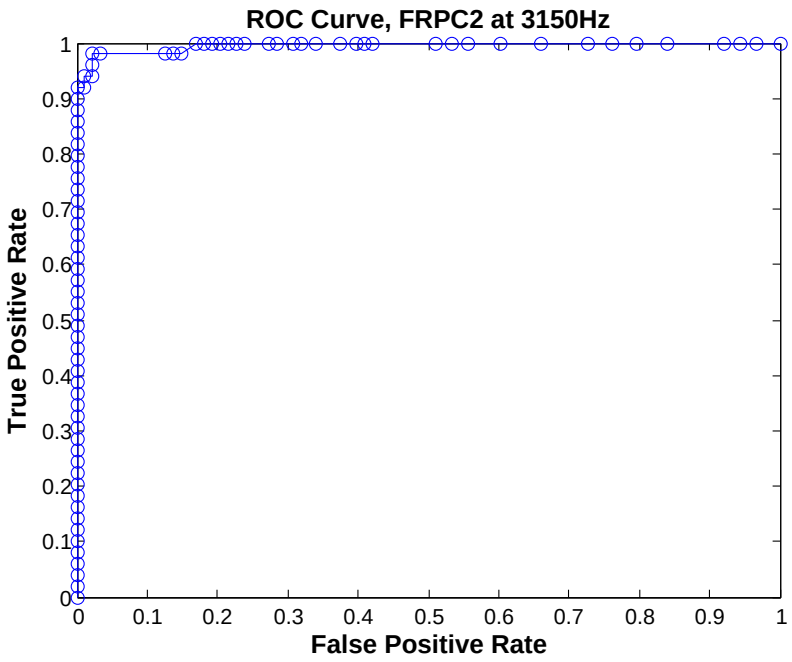

Figure 7-6: ROC curve for FRPC2 at 3150 Hz

7.2 Scaling of ROC Curve with Parametric Study Results

Using the results from the parametric studies, the effect of the SPL, laser power or signal level, and angle of incidence on the amplitude or noise floor of the measurements can be estimated and extrapolated, to construct an estimated ROC curve under those varying conditions. Since sweep duration seemed to not change either the vibration amplitude or noise floor of the signal and left the SNR constant, it is omitted from this study. The data sets used to generate the FRPP1 specimen ROC curve were scaled by the relationships determined in the Chapter 6 due to hypothetical changes in the parameters. For the case of SPL and angle of incidence, shown in Figures 7-7 and 7-9, the amplitude of the measurements done over the defect were scaled by a suitable amount to match the different condition. For the laser power or signal level parameter, shown in Figure 7-8, the noise floor of the measurement, which primarily consisted of the areas where the FRP-concrete system was intact, was scaled to reflect

the hypothetical effect of increasing the distance of the system from the specimen.

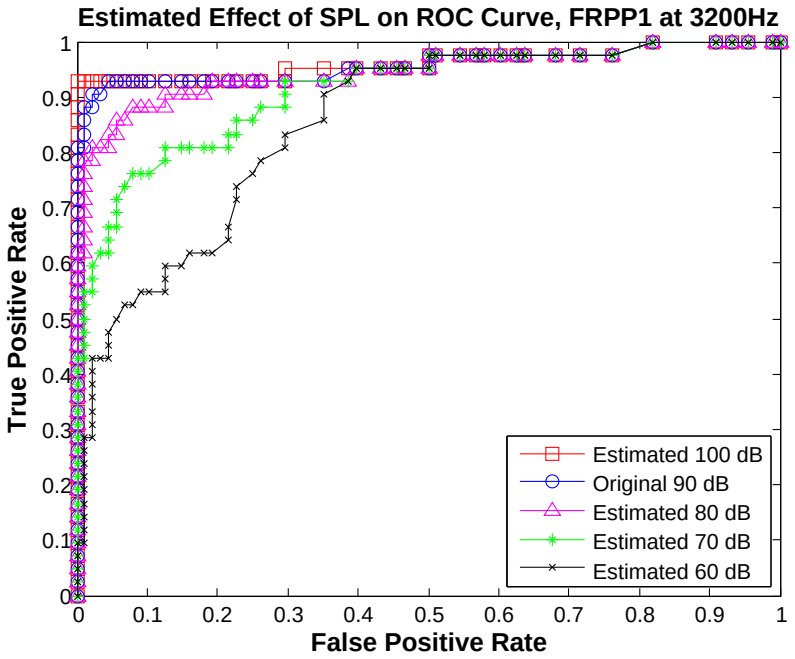

Figure 7-7: Estimated effect of sound pressure level on FRPP1 ROC curve

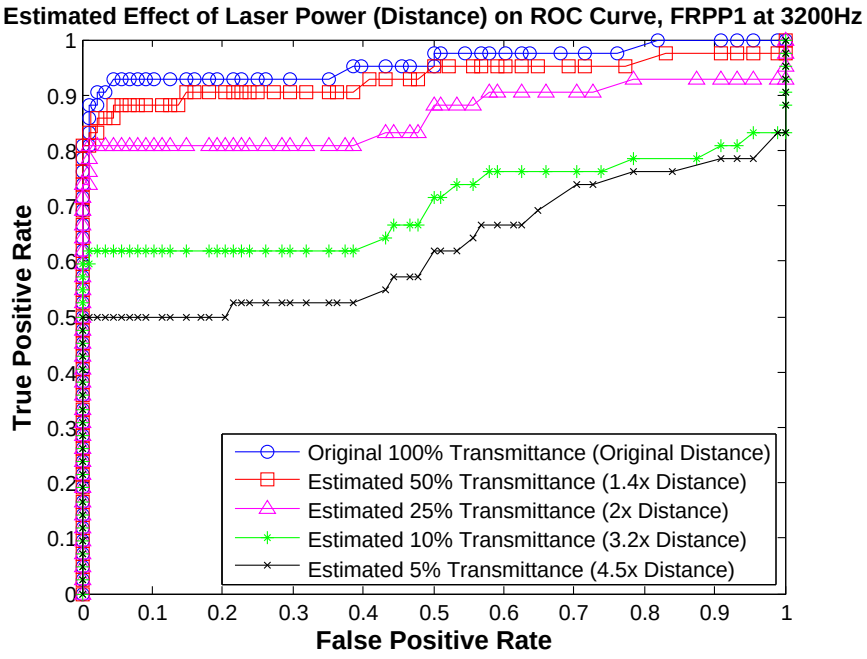

Figure 7-8: Estimated effect of laser power or distance on FRPP1 ROC curve

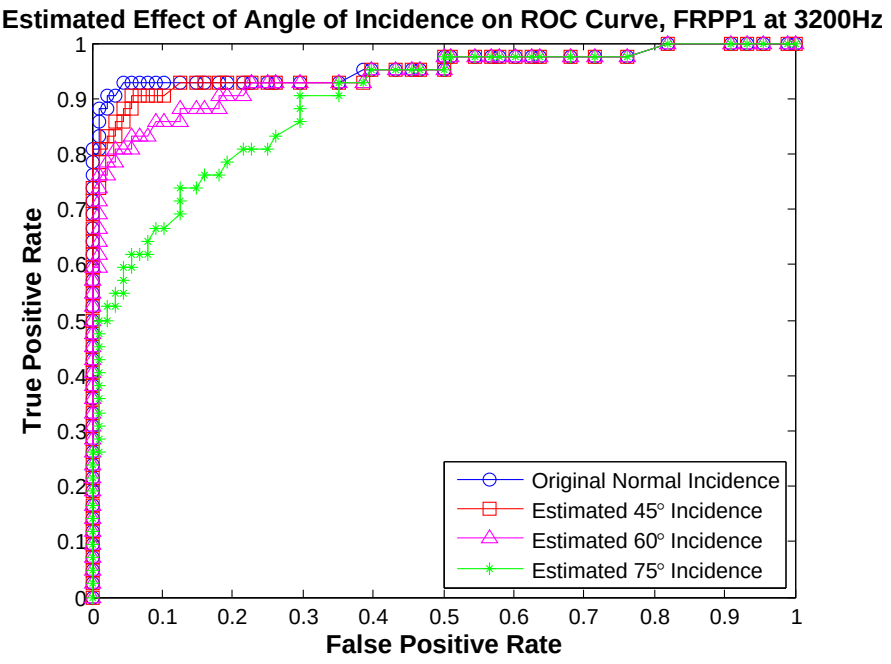

Figure 7-9: Estimated effect of angle of incidence on FRPP1 ROC curve

The results of these measurements suggest a couple of effects that are due to the phenomenology of the defect. On the SPL scaled ROC curve, despite increasing the SPL which increased the defect vibration amplitudes, the true positive rate did not improve beyond a certain point at a low false positive rate because of the measurements at the borders of the defect where the vibration amplitude was minimal. Similarly in the other situations where the noise floor was raised or the defect vibration amplitude was lowered, it is likely that these boundary measurements that display minimal vibration response amplitude at the first resonant mode that will be lowered to the same level of the noise floor and will be counted as false negative detections. More improvements in the ROC curve and probability of detection can come from more sophisticated detection algorithms; in this work only the simple case of finding the greatest amplitude peak for the whole defect which occurs at the first resonant frequency of the defect was considered.

7.3 Summary: ROC Curve Analysis

From a series of frequency sweep measurements made of the specimens, and making a decision based on a simple detection velocity level, ROC curves were generated for four specimens: FRPP1, FRPP2, FRPC1, and FRPC2. True and false positive detection rates varied among the specimens, with the average of the true positive detection rate 91.8% and the average of the false positive detection rate 4.2%. These preliminary ROC curves may not be truly representative of a real world test because in this experiment, the defect was a significant portion of the measured area, while in the real world defects are not expected to be as common or large relative to the measurement area. The results from Chapter 6 were used to approximately scale the ROC curve for the FRPP1 measurement to estimate the effect of changing SPL, laser power, and angle of incidence on the detectability. Above the 90 dB SPL used in the test, there wasn't much beneficial effect, and below 80 dB the test was significantly less accurate. For laser power, 50% power still gave acceptable detectability. For changes in the angle of incidence, 45° gave results almost as good as normal incidence. In general, because of the cosine squared dependence, within 18.3° of normal incidence, there will not be much effect because the measured amplitude is still greater than 90% of the normal incidence amplitude. These results can be used to provide some information about the performance characteristics of a conceptual commercial acoustic-laser vibrometry system.

Chapter 8

Summary, Conclusions, and Future Work

8.1 Summary

The acoustic-laser vibrometry method can identify areas of FRP-reinforced concrete where there is damage at the FRP-concrete interface by measuring the surface vibration of the defect under acoustic excitation. The defects of many different specimens with different sizes were characterized. Theoretical calculations and finite element analysis predicting the resonant frequencies of the defects were conducted showing that estimations of the defect resonant frequencies were relatively accurate. This provides the basis for using a measured resonant frequency for determining the approximate size of a defect using appropriate known material property values. Measurements were made covering the complete area of a defect, obtaining images of the vibration amplitude at the different resonant frequencies showing the mode shapes of the defect. Various parameters such as the sound pressure level, laser signal level, angle of incidence, dwell time, and frequency sweep length were varied to determine their effect on the performance of the system. Using data from the image construction measurements, receiver operating characteristic curves of the system for those defects were generated showing the performance of the system as a defect detection system. Estimated receiver operating characteristic curves under

different parametric conditions were generated. The laboratory experimental system was characterized and demonstrated detecting defects in laboratory created specimens using the acoustic-laser vibrometry method.

8.2 Conclusions

8.2.1 Measurement Methodology

A good number of measurements and parametric studies were made, the purpose of which was to further develop the acoustic-laser vibrometry method for use in detecting defects in FRP-reinforced concrete. In Chapter 5, the frequency sweep defect and image construction measurements, in Sections 5.2 and 5.3, give a basis for the process of simple defect discrimination in a commercial system. In order to characterize an area of interest, frequency sweep measurements would be made in a grid over that area, as in the image construction measurements. The measurement spacing would be predetermined with finer spacing allowing for the detection of smaller defects, but more measurements and therefore longer total measurement time. The simplest method of reviewing the measurements for defect identification would be an operator-independent method that simply looks for measurements with maximum vibration amplitudes that are greater than some detection level. This was the same methodology used to generate the ROC curves in Chapter 7. This methodology works in the case where it is expected that a defect may be small enough to be captured by only one measurement.

If the measurements made are finer than the expected defect size, such that if a defect was present, many measurements would be made over a defect, a better detection methodology involving image construction could be used. Images of the surface vibration of the defect would be constructed at frequencies spanning the whole bandwidth of the frequency sweep, in increments smaller than the typical width of a frequency peak, or approximately every 200 Hz. In this case, the actual images are only for visualization by an operator; a computer would process the underlying

data for detection of defects. For a 0 - 20 kHz frequency sweep, this is 100 images of the surface vibration field of the measured area. Areas of the image or data that show excessive response over many frequencies would likely be defective. There could be detection levels for, not only the maximum vibration amplitude, but also the number of local measurements exhibiting excessive vibration amplitude, and the number of different frequencies that excessive vibration amplitude is observed. Using these multiple criteria would reduce the number of false positives.

8.2.2 Area Rate of Coverage

The key statistic that will govern the functionality of the system will be the area rate of coverage of the system. One of the strengths of a standoff method is the improved area rate of coverage of the NDT methodology, because equipment does not need to be repositioned, only reaimed. Additionally, achieving a low false positive rate, while maintaining a high true positive rate, typically of at least 90% is also important. From the measurements and parametric studies, a preliminary area rate of coverage for the system under specified conditions can be determined.

As shown in the frequency sweep duration study in Section 6.5, the differences in SNR between frequency sweep measurement durations of 0.1 seconds and 60 seconds for a bandwidth of 0 - 20 kHz is negligible. Since resonant peaks of the defects are relatively wide, on the order of 1 kHz, the amount of time the frequency sweep would spend in a 1 kHz band is 5 milliseconds. From the dwell time parametric study in Section 6.4, this means that the minimum frequency that the frequency sweep is able to excite would be on the order of 200 Hz, which would correspond to a defect size of approximately 0.2 square meters, which would be large enough to exhibit an obvious response. Any higher frequencies would easily have enough dwell time to be excited. With a scanning laser vibrometry system, which uses a movable or scanning mirror to reposition the laser spot, up to 30 spots per second can be scanned [53]. A generous assumption would be that each frequency sweep measurement would only take 0.2 seconds with a scanning laser vibrometer to allow for settling and measurement time. Another contribution to the measurement time

would be the number of false positives. The assumption is that there are no real false positives, because what is being measured is the actual surface velocity of the specimen under excitation from an acoustic source. Therefore, with enough time to repeat a measurement, the true nature of the FRP-concrete system can be determined. The time penalty per false positive would be some extra time to remeasure and fully characterize the location of a false positive to obtain a more accurate response frequency response and correctly classify it as a defect or intact material. Therefore, the assumptions made for the time necessary for a measurement of a specified area, are that each measurement takes 0.2 seconds, and each false positive incurs a penalty of some time for a new measurement.

The other factor besides measurement speed that determines the area rate of coverage is the measurement spacing. The measurement spacing will determine how the size of the defect that can be detected, because if a measurement is not made directly over a defect, the defect escapes detection. Without taking into account the time penalty from false positives, the simple equation that determines the time required to measure one square meter dependent on the measurement spacing in a simple grid is given in Equation 8.1. From this equation, the relationship for an individual measurement time of 0.2 seconds can be plotted, shown in Figure 8-1.

$$t = t_m \frac{1}{s^2} \tag{8.1}$$

t = time required to measure one square meter with a square grid of measurements

t_m = time required for one measurement

s = spacing between measurements in meters

As determined in Chapter 5 from the measurement of the FRPP4 and FRPP5 specimens which have various crack widths, it is likely that the smallest defect size that can be detected is 0.25" or 0.625 cm. For a square grid of measurements, a spacing of 0.44 cm is necessary to ensure the maximum circular defect diameter that can be missed is 0.625 cm. The resulting measurement time is 10331 seconds, or approximately 172 minutes. For a maximum circular defect diameter of 0.5" or

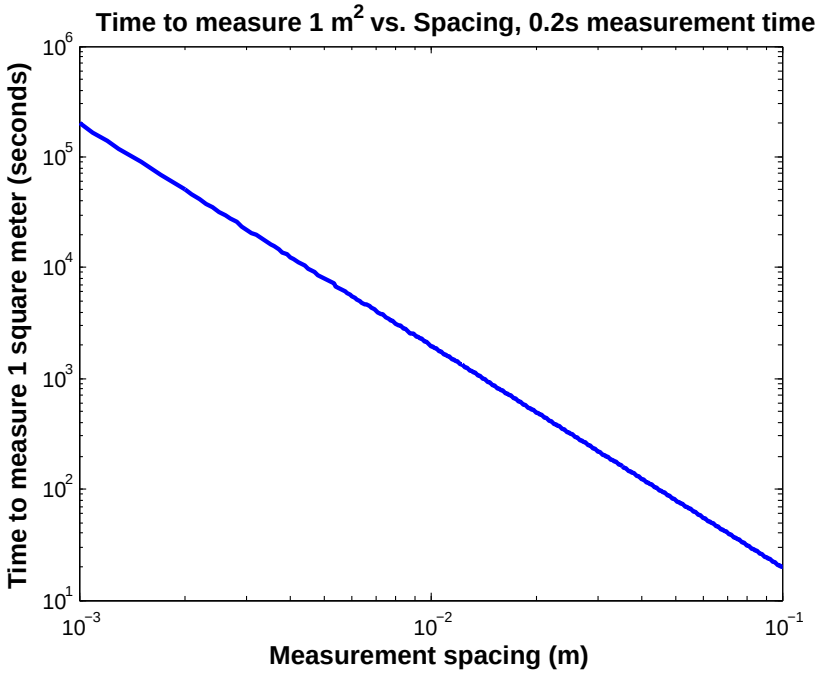

Figure 8-1: Time required to measure 1 square meter vs. measurement spacing, 0.2s measurement time

1.27 cm, the spacing is 0.898 cm, and the measurement time is 2480 seconds, or approximately 41 minutes. For a maximum circular defect diameter of 1" or 2.54 cm, the spacing is 1.796 cm, and the measurement time is only 620 seconds, or just over 10 minutes. If measurements could be made more quickly, such as 0.01 seconds per measurement, for the spacing of 0.44 cm, the resulting measurement time is reduced to 516.5 seconds, or approximately 9 minutes.

When the false positive time penalty is taken into account, the relationship between the time to measure 1 square meter and measurement spacing is given in Figure 8-2. Assuming a false positive rate of 4.2%, which is the average rate from the measurements made in Chapter 7, for the measurement grid spacing of 0.44 cm, with a false positive penalty time of 0.1 seconds, the resulting total measurement time is 10548 seconds or 176 minutes. For a false positive penalty time of 1 second, the total measurement time is 12500 seconds or 208 minutes, and for a false positive penalty time of 10 seconds, the total measurement time is 32025 seconds or 534 minutes. Halving the false positive rate to 2.1%, in the case of the 10 second false

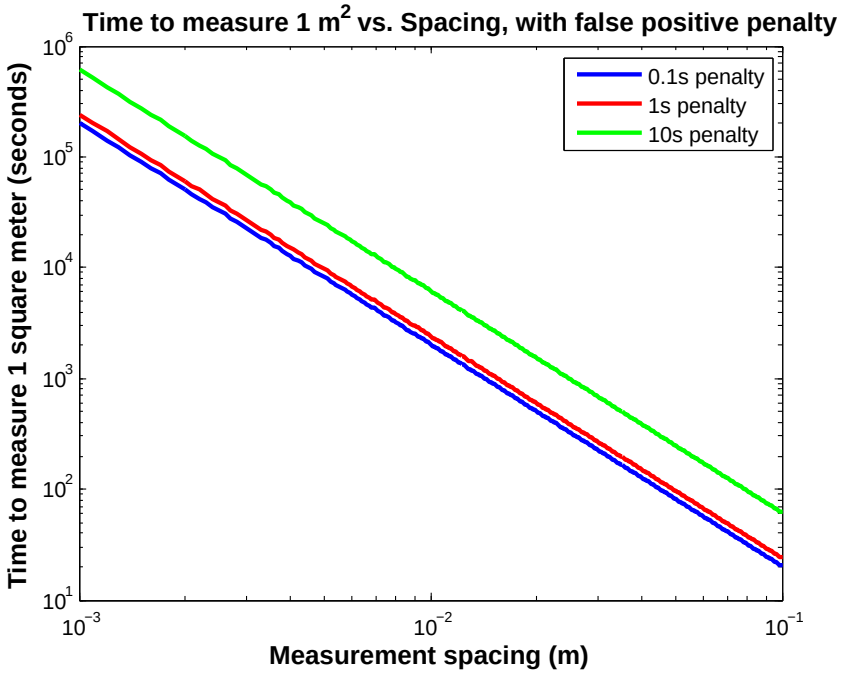

Figure 8-2: Time required to measure 1 square meter vs. measurement spacing, with false positive time penalty

positive penalty time lowers the total measurement time to 21178 seconds or 353 minutes.

In order to completely measure an area of interest, a grid of measurements needs to be made with a spacing smaller than the size of the smallest defect of interest. This spacing is unlikely to be able to be changed to decrease the number of measurements necessary for a given area, because a measurement needs to be made over a defect to detect it. The time necessary per measurement, with a scanning laser vibrometer, is likely to be on the order of 0.2 seconds. Improvement in the speed of measurement by using fewer frequencies of interest for a shorter duration frequency sweep, or the use of a chord of frequencies, to reduce the dwell time will reduce the time necessary for a measurement and increase the area rate of coverage. Reduction of the false positive rate and the time necessary to repeat and confirm a false positive measurement will also increase the area rate of coverage.

8.2.3 Distance Limitations

The overriding limitation on the distance the system can operate at is likely to be due to the acoustic source, because the SPL at the specimen determines the amplitude of the defect vibration and therefore the amplitude measured by the laser vibrometer. The laser vibrometer range is determines the noise floor and can be improved by simply increasing the power of the laser. High power acoustic sources are less common and more difficult to construct.

From the SPL parametric study in Section 6.1, and the ROC curve scaling study in Figure 7-7, 80 dB is the threshold for an acoustic excitation to sufficiently excite a defect. Since sound intensity follows an inverse square law, SPL decreases by 20 dB for an increase in distance from the acoustic source by a factor of 10. The maximum peak SPL at 1 meter from the commercial loudspeaker used is 110 dB, from Table 4.4 [47]. The curve for the SPL of the speaker with distance is shown in Figure 8-3. At 32 meters the speaker has a peak SPL of 80 dB. Accounting for real world conditions, a more realistic target SPL is 90 dB which results a maximum distance of 10 meters from the commercial loudspeaker.

Another candidate acoustic source is the parametric acoustic array (PAA), which is capable of much longer range acoustic excitation and was demonstrated to be capable of 100 dB at just under 10 meters distance and 80 dB at 100 meters distance at a frequency of 1000 Hz, with the source being more powerful for higher frequencies [25]. For the more realistic target SPL of 90 dB, the maximum range would be approximately 30 meters at a frequency of 1000 Hz.

Distance of an operational commercial system will be likely limited by the available acoustic excitation. With a commercial loudspeaker the maximum operational range would be 10 meters, while with a PAA the maximum range would be 30 meters. This is without taking into account angle of incidence, which would be important if the system were looking up at the surface of a column, however within 18.3° of normal incidence, there is only a small effect on system performance.

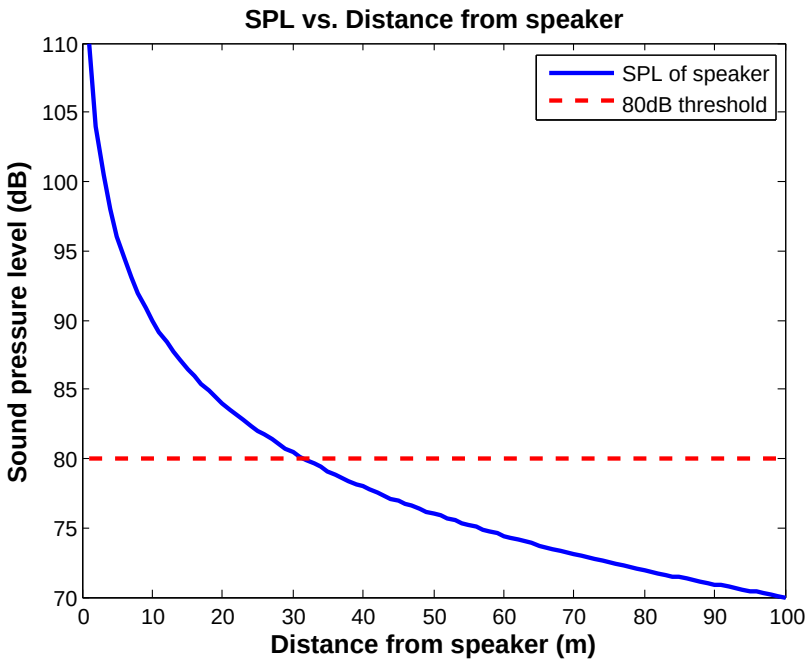

Figure 8-3: Sound pressure level vs. Distance for commercial loudpseaker

8.2.4 Defect Discrimination

In the simplest manner, the acoustic-laser vibrometry system detects defects by looking for areas with much greater vibration amplitude than the surrounding intact FRP-concrete material. Frequency sweep measurements were made which determined the vibration frequency response of the location on the specimen. Defects exhibited resonance peaks at frequencies characteristic of their approximate size. From Equation 2.2, the inverse calculation from the resonant frequency can be made to obtain an approximate side length of the defect assuming it is square with fixed edges. With a similar equation, the same calculation could be made for a circular defect if it is found to be more representative of a typical defect. Another way to determine the size and shape of the defect is to make enough measurements and use an image construction technique, shown in Section 5.3. Once a defect on a specimen is located with a grid of measurements, a fine grid of measurements of the local area can image the defect, where the region excessive vibration response corresponds to the defect shape.

In addition to discrimination of defect size from the frequency of the resonance peaks, it is possible that the vibration frequency response contains features that would determine the type of defect detected. The goal would be to be able to determine more characteristics of the defect such as if the defect is a void, delamination, crack, or concrete spall. A void or delamination will likely look quite similar, however a crack that is narrow in one direction and long in the other, has different characteristics. From the frequency sweep defect measurement results in Section 5.2, the measurements of the cracks on specimen FRPP5 have much lower quality factors, or wider resonance peaks, when compared with the measurements of the void or delamination defect specimens. The spacing of the resonance peaks will also depend on the geometry of a defect, whether it is square, rectangular, or circular, though this is confounded by the anisotropy of the fiberglass material [38]. Concrete spall would also exhibit different characteristics due to extra mass of concrete attached to the defect, which would likely result in a lower vibration amplitude with a much lower quality factor than a void or delamination. It is likely that defect discrimination methods can be developed using characteristics of the vibration frequency response of the defect. Resonant frequencies, peak spacing, peak quality factor, and vibration amplitude are important characteristics to consider.

8.3 Future Work

Future work regarding the acoustic-laser vibrometry method primarily consists of three main efforts: improvement of the method through use of better equipment, investigation into more sophisticated data processing methods that improve the detection capability of the method, and applying the method to other types of defects and problems.

Potential improvements for the method with better equipment will be due to improvements of either the excitation source or the laser vibrometer. In this work a commercial loudspeaker was used which had a relatively minimal range of a couple of meters. A parametric acoustic array can be used which uses an ultrasonic beam

to nonlinearly generate audible sound at a lower audible frequency [25, 31]. The benefits of this is that the ultrasonic beam will be much narrower because of the higher frequency, and therefore able focus the sound onto a specimen and still achieve the necessary frequency range by the nonlinear generation of lower frequency sounds to excite defects. Any increase in the SPL delivered to the target will improve the SNR because defects will vibrate with greater amplitudes. Another improvement would be the use of a scanning or multi-beam laser vibrometry system so that a series of measurements can be made more quickly [26, 53]. A scanning laser vibrometer uses a moveable mirror to steer the laser beam to allow the system to scan up to 30 points per second, instead of having to manually reaim the laser vibrometer for a different measurement. Similarly a multi-beam laser vibrometry system has the capability of measuring from multiple laser beams on the specimen at once. Either would allow for the image construction measurements to be generated much more quickly and the mode shapes more easily identified. An improvement in the laser vibrometry system itself will also lower noise floors and improve the SNR. By using a different wavelength of light where the eye is less sensitive, more power can be used while still being eye safe, improving the noise floor of the laser vibrometer and eliminating the need for retroreflective tape on the specimen. With certain technology, measurements can also be made while moving thus improving the area rate of coverage of the system [54].

Once the data is collected by the system, there are also improvements that can be made in the algorithms that detect resonant peaks. In this work, the maximum amplitude peaks were simply identified and a vibration amplitude higher than a set detection level was classified as a detection, and lower was classified as a negative result. Instead of taking the FFT of the whole time series of a frequency sweep measurement, a better SNR may be obtained by processing the data as many smaller windows that can better identify resonant peaks because the bandwidth of interest is narrower. Also, previous work has been done in specific feature detection methods for identifying resonance peaks using techniques from spectral peak identification [31, 55]. Techniques from system identification to identify the frequency and damping of a resonant peak can also be used to better characterize the vibration frequency

responses and make better determinations of whether or not a defect is present or provide defect discrimination.

The acoustic-laser vibrometry method is a robust methodology that has already been applied to a couple of problems such as the detection of defects in FRP-reinforced concrete as discussed in this work [34], FRP-steel bonded systems [32, 33], and landmine detection [25, 31]. There are many other potential defects or discontinuities in objects that this method may be able to detect. Some other possible applications include the detection of defects in bridge decks and roadways, inspection for corrosion in reinforced concrete, and detection of defects in composite materials. For these potential applications some challenges need to be overcome. In general, the difficulty is in figuring out a standoff method of exciting the specimen with enough energy such that the differences in vibration amplitude between intact and damage material is apparent through the laser vibrometer measurement. Through an improvement in laser vibrometry technology it is possible more inspection opportunities will present themselves because of improvements in the vibrometer noise floor. There is also some precedence for the underwater operation of a laser vibrometer [56, 57]. Sound couples into solid materials better underwater because of the closer acoustic impedances of water and common building materials such as steel and concrete. This means that there is the potential for underwater inspection of metal pipelines and reinforced concrete structures such as oil platform columns, bridge piers, dams, and levies.

It is hoped that the future work suggested will improve the acoustic-laser vibrometry method, expand the scope of potential applications, and eventually help improve the state of the nation's infrastructure.

Appendix A

A.1 Chapter 5: Defect Measurements

A.1.1 Frequency Sweep Defect Measurements

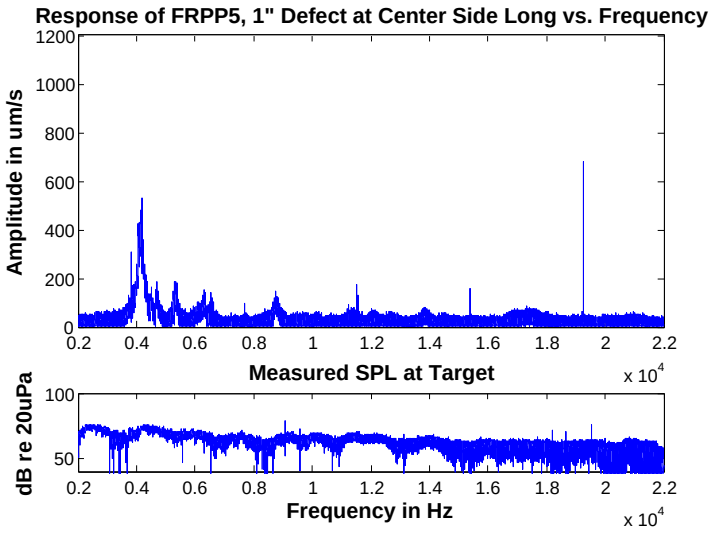

Figure A-1: Frequency response of FRPP5 at center side long of 1” wide crack defect

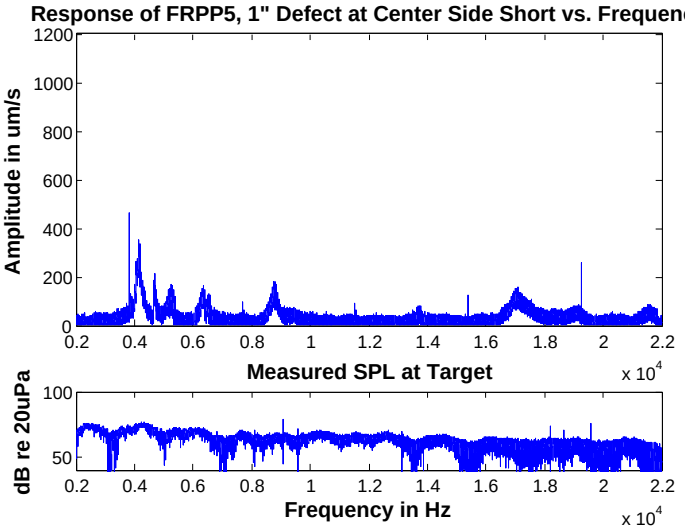

Figure A-2: Frequency response of FRPP5 at center side short of 1" wide crack defect

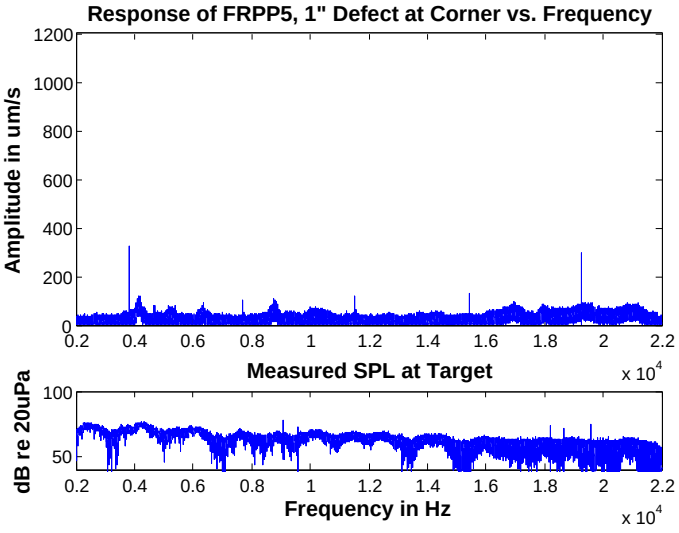

Figure A-3: Frequency response of FRPP5 at corner of 1" wide crack defect

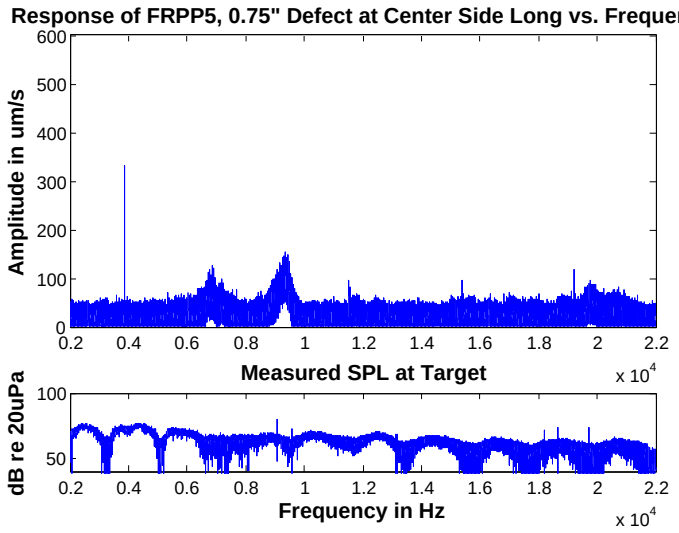

Figure A-4: Frequency response of FRPP5 at center side long of 0.75" wide crack defect

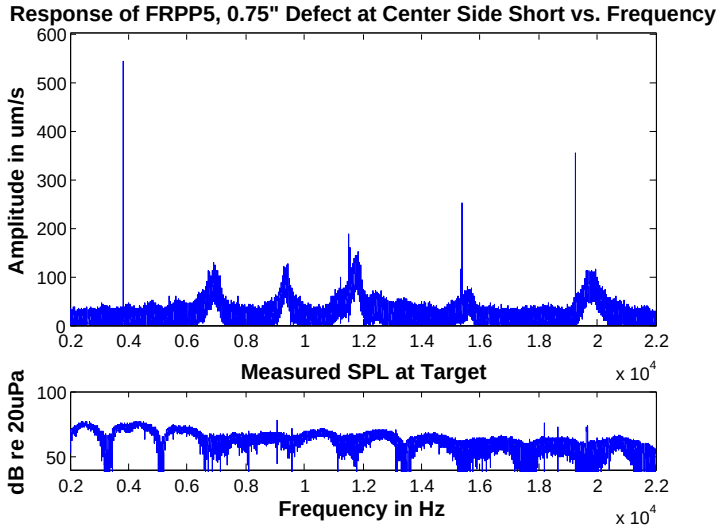

Figure A-5: Frequency response of FRPP5 at center side short of 0.75" wide crack defect

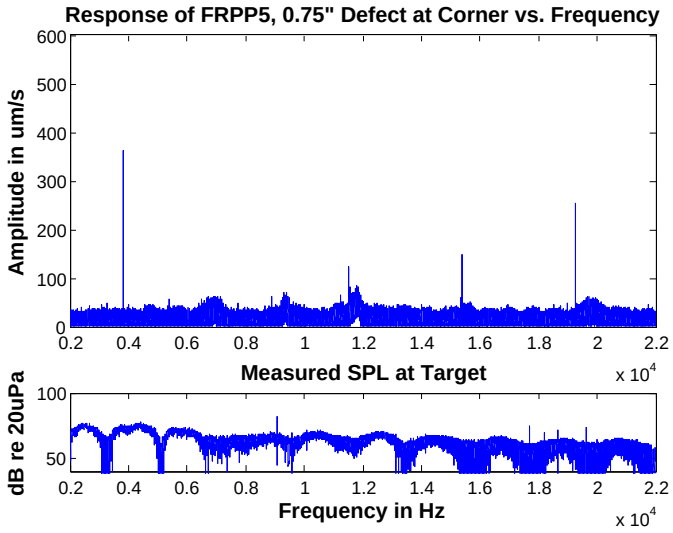

Figure A-6: Frequency response of FRPP5 at corner of 0.75" wide crack defect

A.2 Chapter 6: Parametric Studies

A.2.1 Sound Pressure Level

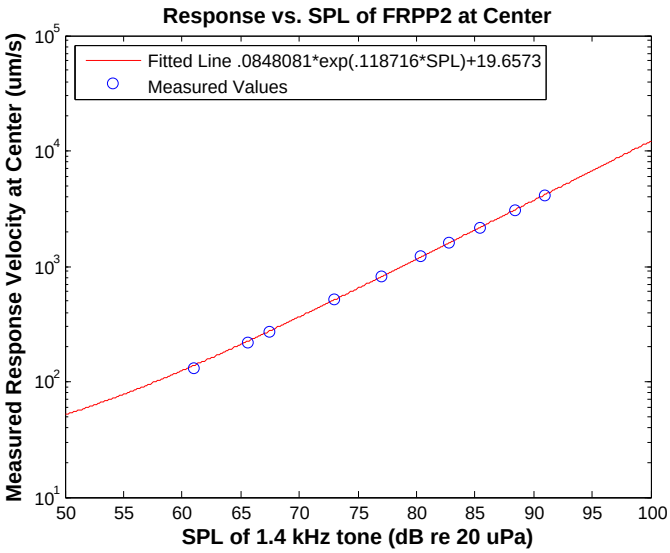

Figure A-7: Vibration amplitude of specimen FRPP2 vs. sound pressure level and fitted curve

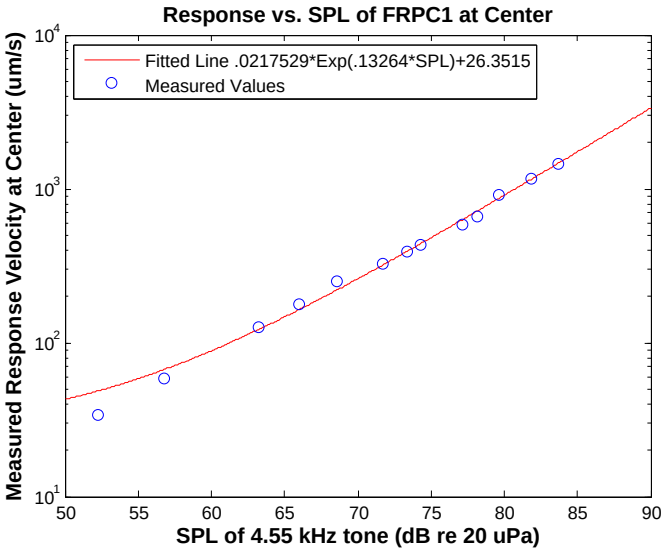

Figure A-8: Vibration amplitude of specimen FRPC1 vs. sound pressure level and fitted curve

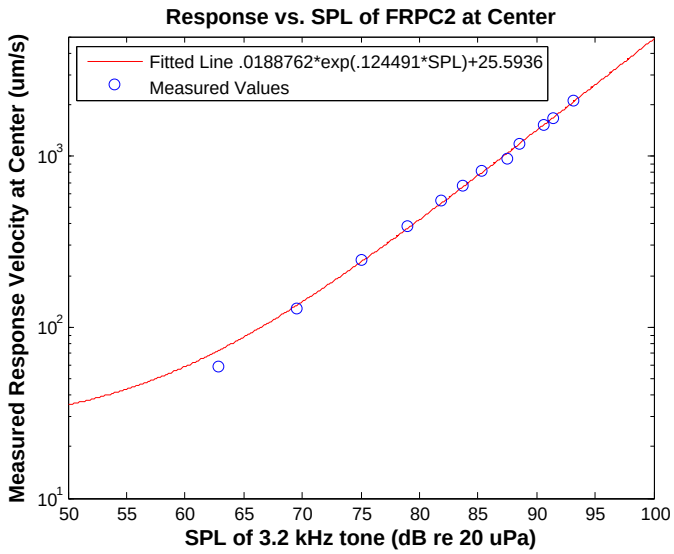

Figure A-9: Vibration amplitude of specimen FRPC2 vs. sound pressure level and fitted curve

A.2.2 Dwell Time

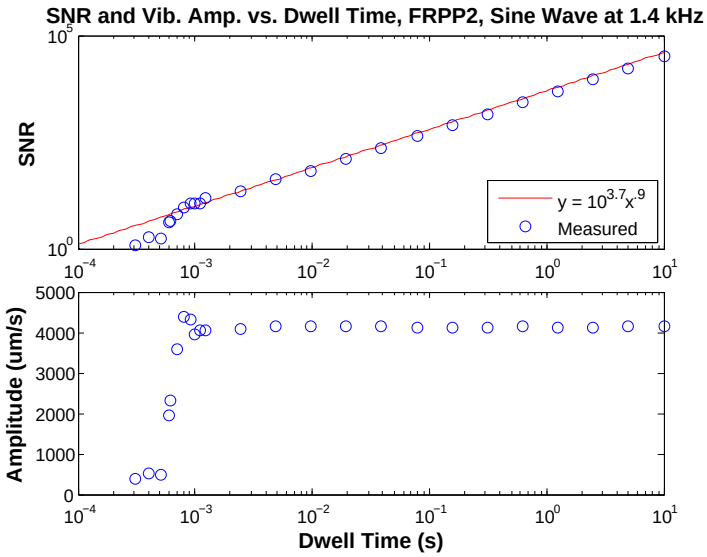

Figure A-10: SNR and vibration amplitude as a function of dwell time for a sine wave excitation for FRPP2

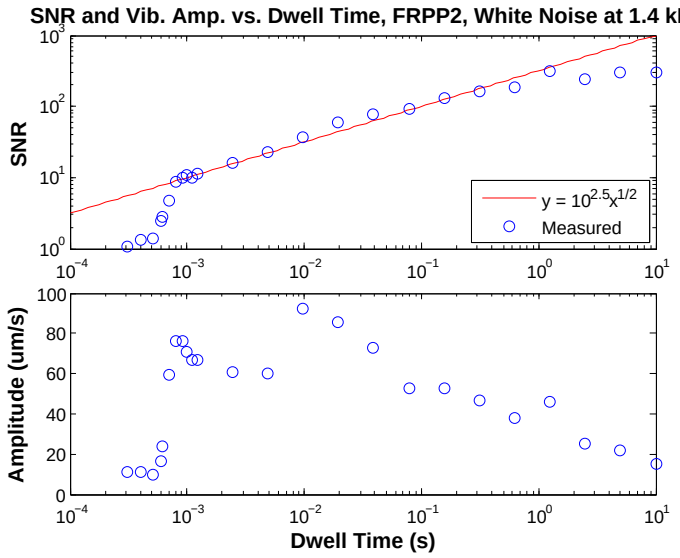

Figure A-11: SNR and vibration amplitude as a function of dwell time for a white noise excitation for FRPP2

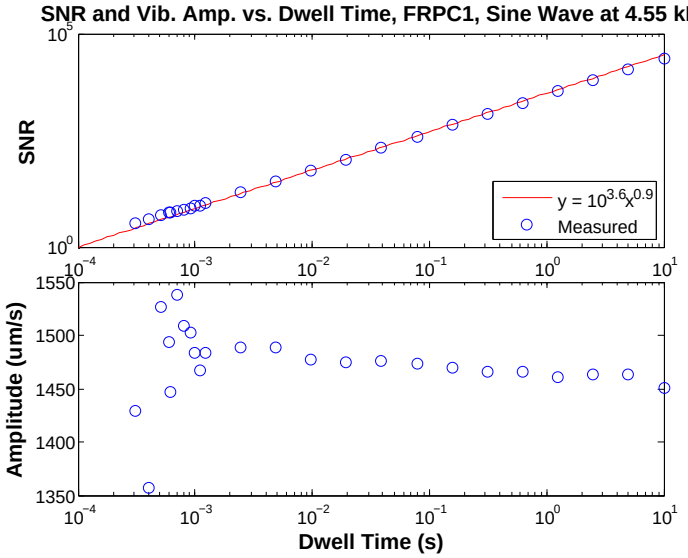

Figure A-12: SNR and vibration amplitude as a function of dwell time for a sine wave excitation for FRPC1

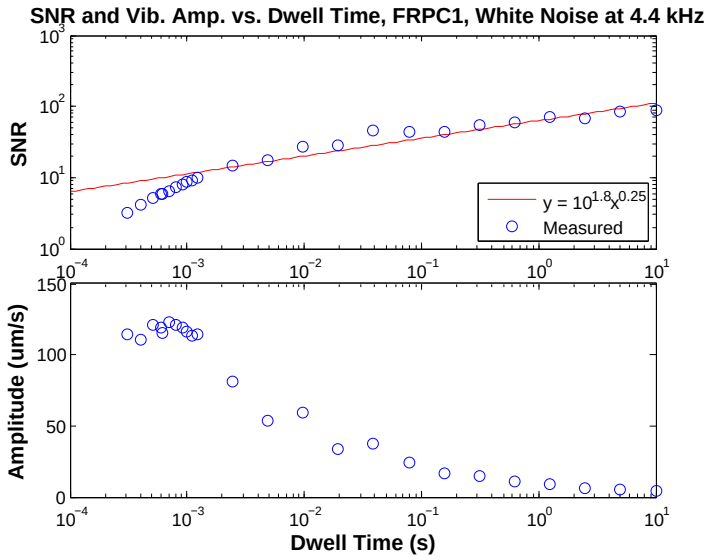

Figure A-13: SNR and vibration amplitude as a function of dwell time for a white noise excitation for FRPC1

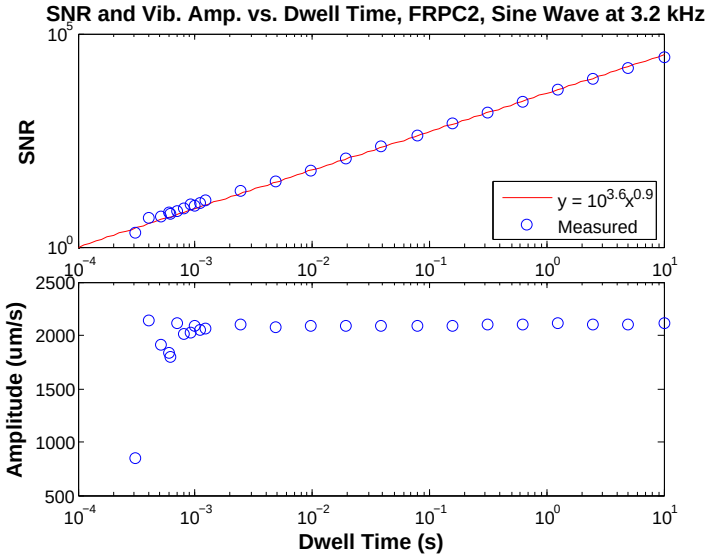

Figure A-14: SNR and vibration amplitude as a function of dwell time for a sine wave excitation for FRPC2

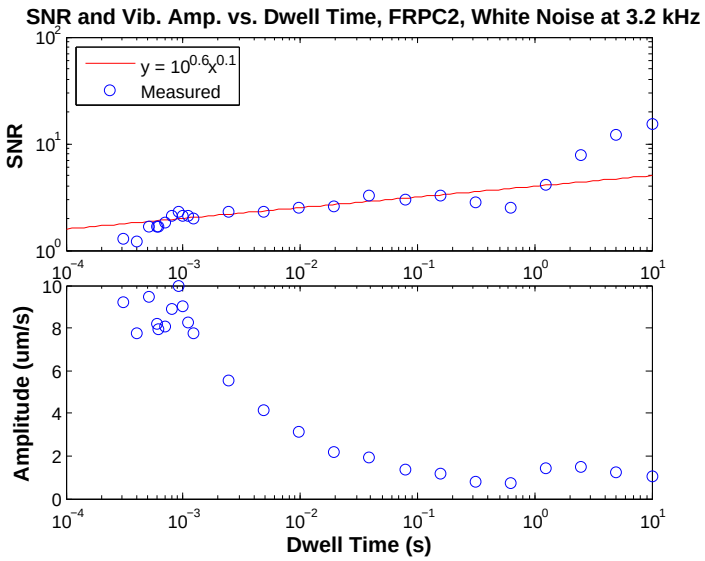

Figure A-15: SNR and vibration amplitude as a function of dwell time for a white noise excitation for FRPC2

A.2.3 Frequency Sweep Duration Study

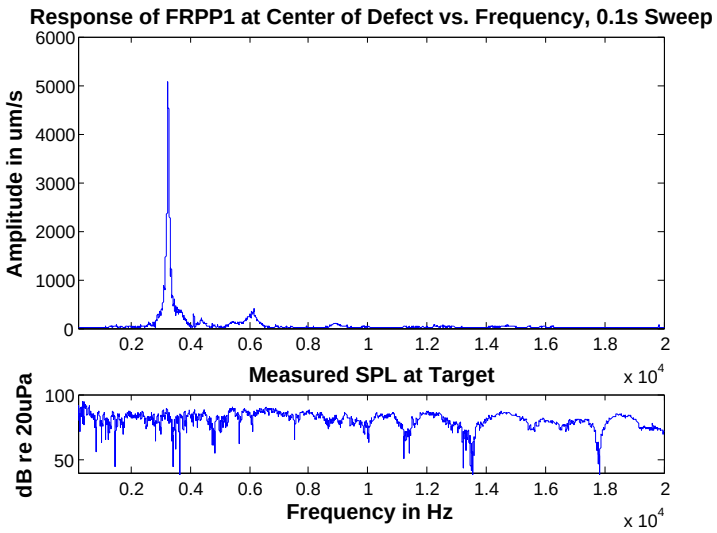

Figure A-16: Frequency Responses from FRPP1, 0.1 second long 0-20 kHz frequency sweep

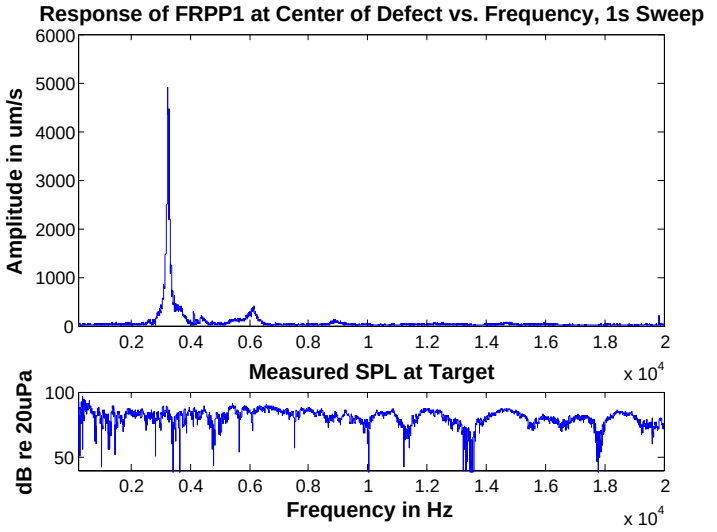

Figure A-17: Frequency Responses from FRPP1, 1 second long 0-20 kHz frequency sweep

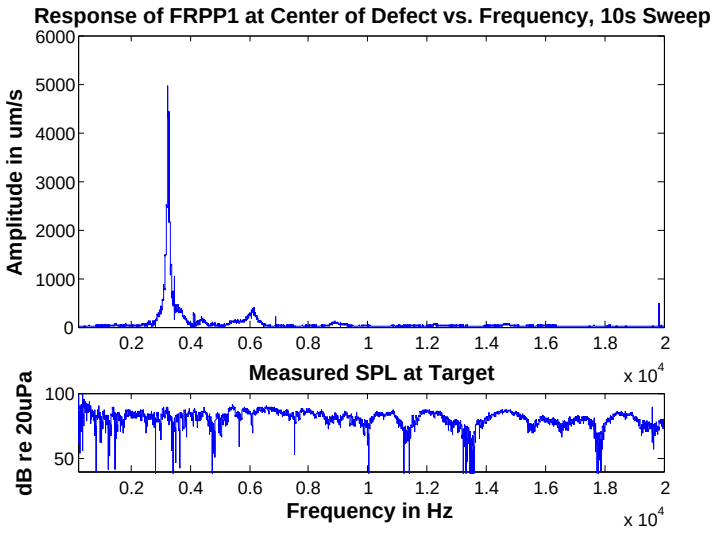

Figure A-18: Frequency Responses from FRPP1, 10 second long 0-20 kHz frequency sweep

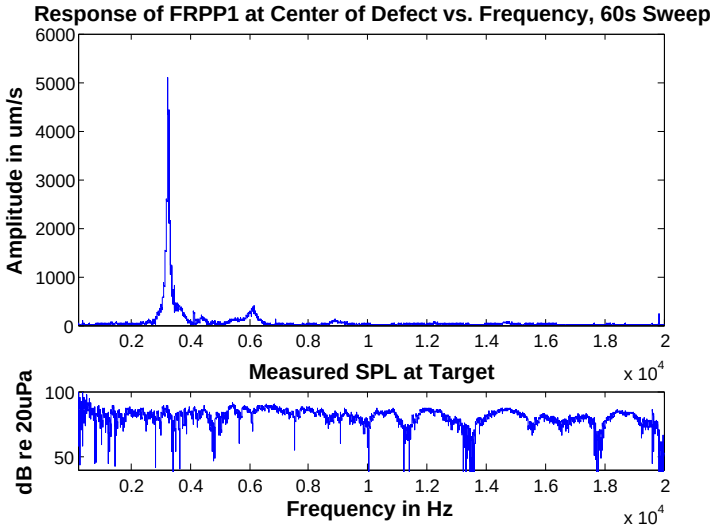

Figure A-19: Frequency Responses from FRPP1, 60 second long 0-20 kHz frequency sweep

A.3 Chapter 7: Receiver Operating Characteristic Curve Analysis

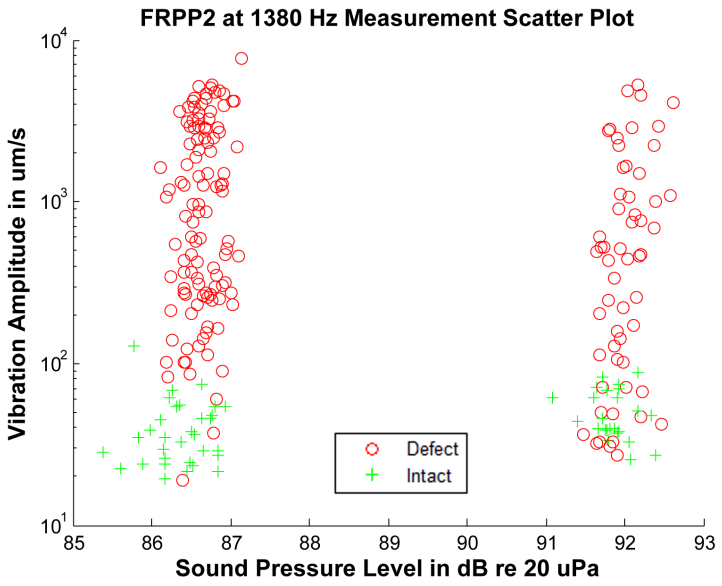

Figure A-20: Scatter plot data from FRPP2 grid measurement at 1380 Hz

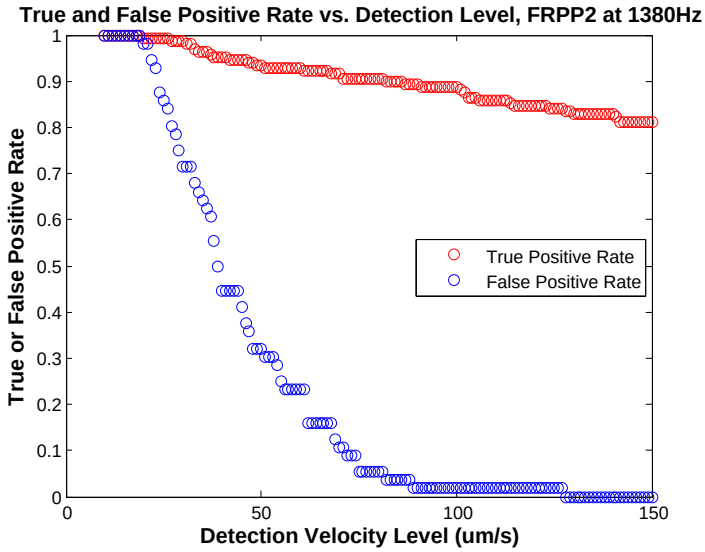

Figure A-21: Plot of true and false positive rate vs. detection velocity level for FRPP2 at 1380 Hz

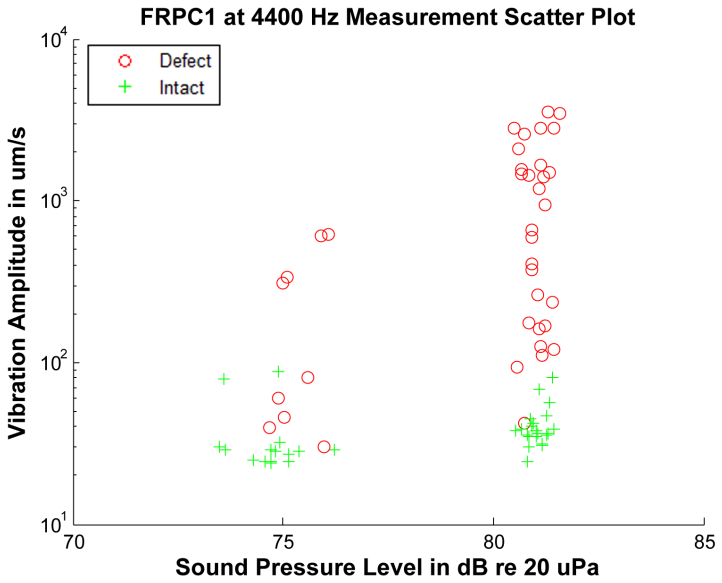

Figure A-22: Scatter plot data from FRPC1 grid measurement at 4400 Hz

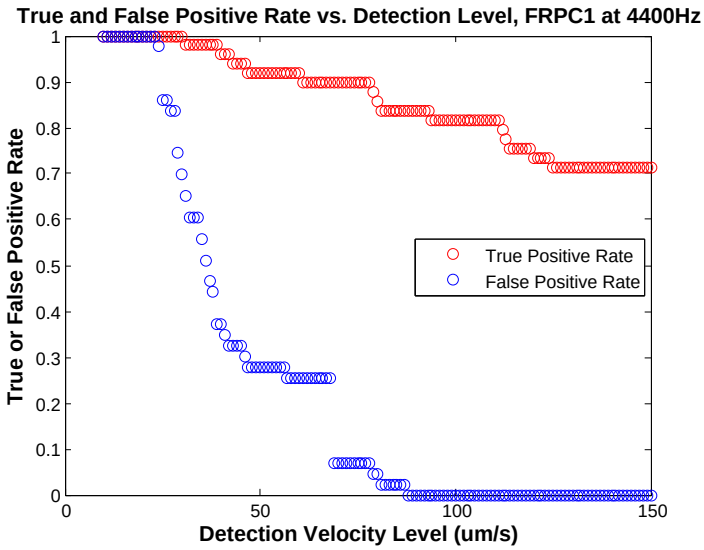

Figure A-23: Plot of true and false positive rate vs. detection velocity level for FRPC1 at 4400 Hz

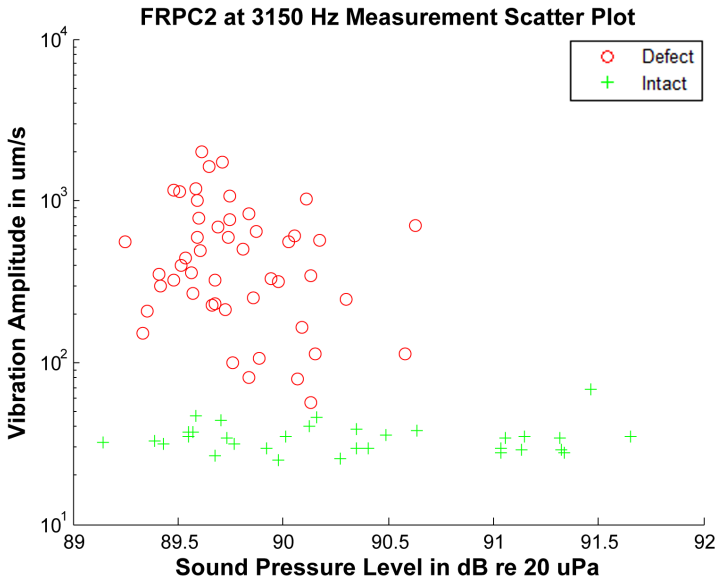

Figure A-24: Scatter plot data from FRPC2 grid measurement at 3150 Hz

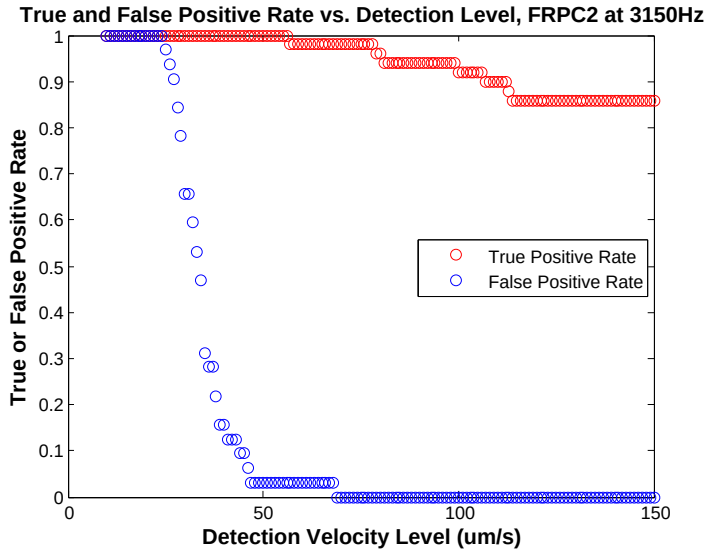

Figure A-25: Plot of true and false positive rate vs. detection velocity level for FRPC2 at 3150 Hz

References

[1] R. Reid. The infrastructure crisis. *Civil engineering*, 78(1):40–65, 2008.

[2] ASCE. 2009 report card for americas infrastructure. 2009.

[3] NTSB. *Highway accident report: interstate 35W collapse over the Mississippi River Minneapolis, Minnesota, August 1, 2007*. American Society of Civil Engineers, Washington, DC, 2007.

[4] S. Hao. I-35w bridge collapse. *Journal of Bridge Engineering*, 15(5):608–614, 2010.

[5] RJ Woodward and FW Williams. Collapse of yns-y-gwas bridge, glamorgan. In *ICE Proceedings*, volume 84, pages 635–669. Ice Virtual Library, 1988.

[6] J.P. Broomfield. *Corrosion of steel in concrete: understanding, investigation and repair*. Taylor & Francis, 1996.

[7] K. Wardhana and F.C. Hadipriono. Analysis of recent bridge failures in the united states. *Journal of Performance of Constructed Facilities*, 17(3):144–150, 2003.

[8] K. Wardhana and F.C. Hadipriono. Study of recent building failures in the united states. *Journal of performance of constructed facilities*, 17(3):151–158, 2003.

[9] Z.A. Eldukair and B.M. Ayyub. Analysis of recent us structural and construction failures. *Journal of Performance of Constructed Facilities*, 5(1):57–73, 1991.

[10] C.R. Farrar and K. Worden. An introduction to structural health monitoring. *Philosophical Transactions of the Royal Society A: Mathematical, Physical and Engineering Sciences*, 365(1851):303–315, 2007.

[11] K. Worden, C.R. Farrar, G. Manson, and G. Park. The fundamental axioms of structural health monitoring. *Proceedings of the Royal Society A: Mathematical, Physical and Engineering Science*, 463(2082):1639–1664, 2007.

[12] ASNT. Introduction to nondestructive testing, 2012. http://www.asnt.org/.

[13] P.J. Shull. *Nondestructive evaluation: theory, techniques, and applications*, volume 142. CRC, 2002.

[14] N.J. Carino et al. The impact-echo method: an overview. In *Proceedings of the 2001 Structures Congress & Exposition, May*, pages 21–23, 2001.

[15] U. Meier. Strengthening of structures using carbon fibre/epoxy composites. *Construction and Building Materials*, 9(6):341–351, 1995.

[16] H. Saadatmanesh and M.R. Ehsani. Rc beams strengthened with gfrp plates. i: Experimental study. *Journal of Structural Engineering*, 117(11):3417–3433, 1991.

[17] C. Tuakta. Use of fiber reinforced polymer composite in bridge structures. Master's thesis, Massachusetts Institute of Technology, 2005.

[18] T.Y. Yu. *Condition assessment of GFRP-retrofitted concrete cylinders using electromagnetic waves*. PhD thesis, Massachusetts Institute of Technology, 2008.

[19] O. Büyüköztürk. Imaging of concrete structures. *NDT & E International*, 31(4):233–243, 1998.

[20] O. Güneş. Microwave imaging of concrete structures from nondestructive evaluation. Master's thesis, Massachusetts Institute of Technology, 1998.

[21] J.A. Ortega. Assessment of FRP-confined concrete: understanding behavior and issues in nondestructive evaluation using radar. Master's thesis, Massachusetts Institute of Technology, 2006.

[22] A.L. Kachelmyer and K.I. Schultz. Laser vibration sensing. *The Lincoln Laboratory Journal*, 8(1):3–28, 1995.

[23] F. Chen and D. McKillip. Measurement and analysis of vibration and deformation using laser metrology for automotive application. *Proceedings of the Institution of Mechanical Engineers, Part D: Journal of Automobile Engineering*, 221(6):725–738, 2007.

[24] C. Santulli and G. Jeronimidis. Development of a method for nondestructive testing of fruits using scanning laser virometry (slv). *NDT. net*, 11(10), 2006.

[25] R.W. Haupt and K.D. Rolt. Standoff acoustic laser technique to locate buried land mines. *Linc. Lab. J*, 15:3–22, 2005.

[26] V. Aranchuk, A. Lal, C. Hess, and J.M. Sabatier. Multi-beam laser doppler vibrometer for landmine detection. *Optical Engineering*, 45(10):104302–104302, 2006.

[27] J.M. Sabatier and N. Xiang. Laser-doppler based acoustic-to-seismic detection of buried mines. In *Proc. SPIE*, volume 3710, pages 215–222. Orlando, FL, 1999.

[28] S. Beyer, D. Gornicki, and G. Müller. Analysis of laser-induced vibrations to detect non-adhesive regions of coatings. *Applied Physics A: Materials Science & Processing*, 79(4):1501–1504, 2004.

[29] A. Ghoshal, A. Chattopadhyay, MJ Schulz, R. Thornburgh, and K. Waldron. Experimental investigation of damage detection in composite material structures using a laser vibrometer and piezoelectric actuators. *Journal of intelligent material systems and structures*, 14(8):521–537, 2003.

[30] WJ Staszewski, BC Lee, L. Mallet, and F. Scarpa. Structural health monitoring using scanning laser vibrometry: I. lamb wave sensing. *Smart Materials and Structures*, 13(2):251, 2004.

[31] J.H. Doherty. Landmine detection with a standoff acoustic/laser technique. Master's thesis, Massachusetts Institute of Technology, 2008.

[32] T.J. Emge. Remote nondestructive evaluation of composite-steel interface by acoustic laser vibrometry. Master's thesis, Massachusetts Institute of Technology, 2012.

[33] T. Emge and O. Büyüköztürk. Remote nondestructive testing of composite-steel interface by acoustic laser vibrometry. *Materials Evaluation*, 70(12):1401–1410, 2012.

[34] O. Büyüköztürk, R. Haupt, C. Tuakta, and J. Chen. Remote detection of debonding in frp-strengthened concrete structures using acoustic-laser technique. In O. Büyüköztürk, M.A. Taşdemir, O. Güneş, and Y. Akkaya, editors, *Nondestructive Testing of Materials and Structures*, pages 19–24. RILEM Bookseries, Vol. 6, Springer, 2013.

[35] O. Güneş. *A fracture-based approach to understanding debonding in FRP bonded structural members*. PhD thesis, Massachusetts Institute of Technology, 2004.

[36] C. Tuakta. *Effects of moisture on debonding in FRP-retrofitted concrete systems*. PhD thesis, Massachusetts Institute of Technology, 2011.

[37] W. Soedel. *Vibrations of shells and plates*, volume 177. CRC, 2004.

[38] A.W. Leissa. Vibration of plates. Technical report, DTIC Document, 1969.

[39] F. Rice. *Physics 6 Sophomore Physics Lab Manual*. Caltech, 2007.

[40] ADINA R & D Inc. ADINA theory and modeling guide. Technical report, ARD 10-7, 2010.

[41] L.G. Olson and K.J. Bathe. A study of displacement-based fluid finite elements for calculating frequencies of fluid and fluid-structure systems. *Nuclear Engineering and Design*, 76(2):137–151, 1983.

[42] Fyfe Co. LLC. Tyfo SEH-51, Nov 2009.

[43] Polytec Inc. http://www.polytec.com.

[44] Polytec Inc. OFV-505/503 vibrometer sensor head data sheet, 2010.

[45] Polytec Inc. OFV-5000 vibrometer controller data sheet, 2010.

[46] M-Audio. http://www.m-audio.com.

[47] M-Audio. M-audio studiophile DSM1 user guide, 2009.

[48] Measurement Computing. Wavebook/516E datasheet.

[49] Earthworks. http://www.earthworksaudio.com.

[50] Earthworks. M30 user's manual, 2011.

[51] Earthworks. Microphone preamplifiers owner's manual, 2011.

[52] T. Fawcett. An introduction to ROC analysis. *Pattern recognition letters*, 27(8):861–874, 2006.

[53] Polytec Inc. PSV-400 scanning vibrometer data sheet, 2011.

[54] L.A. Jiang, M.A. Albota, R.W. Haupt, J.G. Chen, and R.M. Marino. Laser vibrometry from a moving ground vehicle. *Applied Optics*, 50(15):2263–2273, 2011.

[55] W.E. Wallace, A.J. Kearsley, and C.M. Guttman. An operator-independent approach to mass spectral peak identification and integration. *Analytical chemistry*, 76(9):2446–2452, 2004.

[56] B. Woodward and H. Sari. Underwater speech communications with a modulated laser. *Applied Physics B: Lasers and Optics*, 91(1):189–194, 2008.

[57] A.J. Antończak, P. Kozioł, J.Z. Sotor, P.R. Kaczmarek, and K.M. Abramski. Laser doppler vibrometry with a single-frequency microchip green laser. *Measurement Science and Technology*, 22(11):115306, 2011.